Energy Storage and Conversion

ACADEMIC
ACADEMIC PUBLISHING PTE LTD
Volume 3 Issue 4 2025
eISSN: 3029-2778(Online)

https://ojs.acad-pub.com/index.php/ESC

4

Editorial Team

Editor-in-Chief

Associate Editor

Editorial Board Members

Volume 3 Issue 4 • 2025

Energy Storage and Conversion

Editor-in-Chief

Prof. Xiaohu Yang

Xi'an Jiaotong University, China

ACADEMIC
ACADEMIC PUBLISHING PTE LTD

2025 | Volume 3 | Issue 4

Energy Storage and Conversion

https://ojs.acad-pub.com/index.php/esc

Contents

Articles

Reviews

2025 | Volume 3 | Issue 4

Energy Storage and Conversion

https://ojs.acad-pub.com/index.php/esc

Contents

Editorial

Energy Storage and Conversion 2025, 3(4), 3850.
doi: https://doi.org/10.59400/esc3850

Article

Comparative evaluation of solar photovoltaic cell technologies across Türkiye's climatic regions: A PVsyst simulation-based analysis

Muhammed Fatih Saltuk

Development and Investment Bank of Türkiye, Istanbul 34768, Turkey; fatih.saltuk@kalkinma.com.tr

CITATION

Saltuk MF. Comparative evaluation of solar photovoltaic cell technologies across Türkiye's climatic regions: A PVsyst simulation-based analysis. Energy Storage and Conversion. 2025; 3(4): 3850. https://doi.org/10.59400/esc3850

ARTICLE INFO

Received: 5 August 2025
Revised: 6 November 2025
Accepted: 8 November 2025
Available online: 3 December 2025

Abstract: Over the past fifteen years, solar photovoltaic (PV) technologies have become a part of the global energy transition, primarily driven by sustained reductions in capital costs. This rapid deployment has intensified the need for robust, technology-specific performance assessments under diverse climatic conditions. This study presents a comparative evaluation of three crystalline silicon PV cell technologies, which are Passivated Emitter and Rear Contact (PERC), Tunnel Oxide Passivated Contact (TOPCon), and Silicon Heterojunction (SHJ/HJT), across Türkiye's climatically heterogeneous regions using PVsyst simulation software. A rigorously controlled modelling framework was employed, in which all system-level parameters, including irradiance data, thermal behaviour, array configuration, and loss assumptions, were held constant across simulations, thereby isolating the impact of cell architecture on energy yield. The results demonstrate clear performance differentiation among the examined technologies. SHJ modules exhibit superior energy output under high temperature conditions due to favourable temperature coefficients, whereas TOPCon modules show enhanced robustness under harsh operating environments and improved resistance to lifetime degradation. PERC technology, despite its maturity, remains competitive in regions characterised by moderate climatic stress. These findings indicate that PV technology selection should extend beyond nominal efficiency metrics to incorporate thermal sensitivity, degradation behaviour, and low irradiance performance. Consequently, informed PV investment and deployment strategies must align cell technological attributes with specific environmental conditions. While controlled PVsyst simulations provide a consistent comparative baseline, their practical relevance depends on careful contextualisation to real-world operating environments.

Keywords: PV cell technology; renewable energy; PV cell performance; PVsyst; performance optimization

1. Introduction

Over the past fifteen years, solar energy has undergone a transformation, evolving into a major contributor to global electricity. Photovoltaic (PV) systems have advanced through coordinated progress in technology, economics, and policy frameworks. Continuous reductions in generation costs, as reported by IRENA (2024) [1], have coincided with rapid capacity expansion and sustained innovation. Crystalline silicon has emerged as the prevailing PV material, supported by advances in cell structures such as PERC, TOPCon, and silicon heterojunction designs, which have substantially elevated commercial module efficiencies. Parallel improvements in manufacturing processes and system integration have further accelerated cost

reductions, positioning utility-scale solar power among the most economically competitive electricity generation options worldwide [1]. The trend of PV technology in terms of installed cost, capacity factor and levelized cost of electricity is given in **Figure 1**.

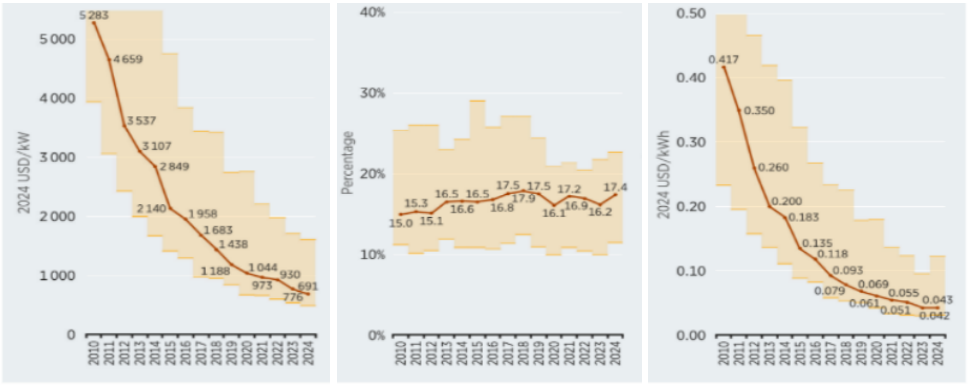

(a) **(b)** **(c)**

Figure 1. Global weighted average and range of **(a)** Total installed cost; **(b)** Capacity factor; **(c)** Levelized cost of electricity for utility-scale solar PV, 2010–2024 [1].

The global installed capacity of solar power has an exponential increase. In 2010, global solar PV capacity was approximately 40 GW. By the end of 2024, it surpassed more than 1000 GW, driven largely by policy incentives, cost competitiveness, and climate commitments. The largest contributions have come from China, the European Union, the United States, and, more recently, India and Southeast Asia. According to the IEA report, Solar Energy is expected to be an energy pioneer by the end of 2030 [2]. Foreseen energy outlook by 2030 is illustrated in **Figure 2**.

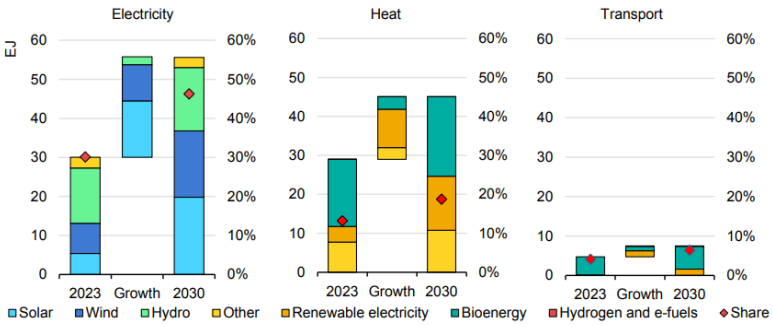

Figure 2. Foreseen energy outlook by 2030 [2].

The global diffusion of solar power has been enabled by supportive policy instruments, market mechanisms and technological maturation. Concurrent advances in PV cell architectures reflect distinct strategies to mitigate recombination losses while sustaining cost effectiveness and scale manufacturing [2]. The main structure of these PV cells is illustrated in **Figure 3** below [3].

According to the projections presented in the International Technology Roadmap for Photovoltaic (ITRPV), while PERC will gradually lose dominance, TOPCon is projected to emerge as the leading technology due to its higher efficiency potential and manufacturing compatibility, whereas SHJ adoption may remain constrained by

cost and process complexity [4]. Market share expectation of PV cell technologies is given in **Figure 4**.

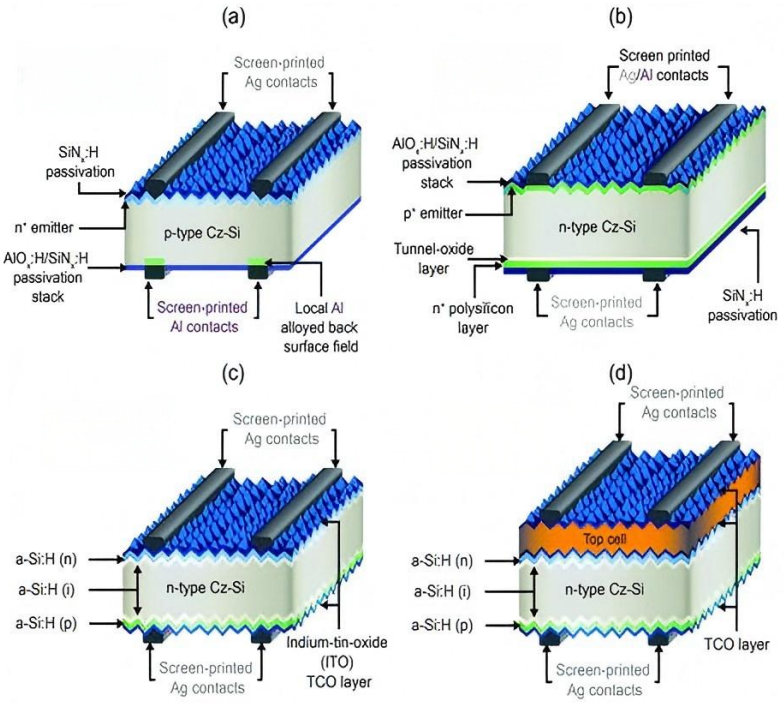

Figure 3. Illustrated structure of PV technologies: **(a)** PERC; **(b)** TOPCon; **(c)** SHJ; **(d)** Tandem [3].

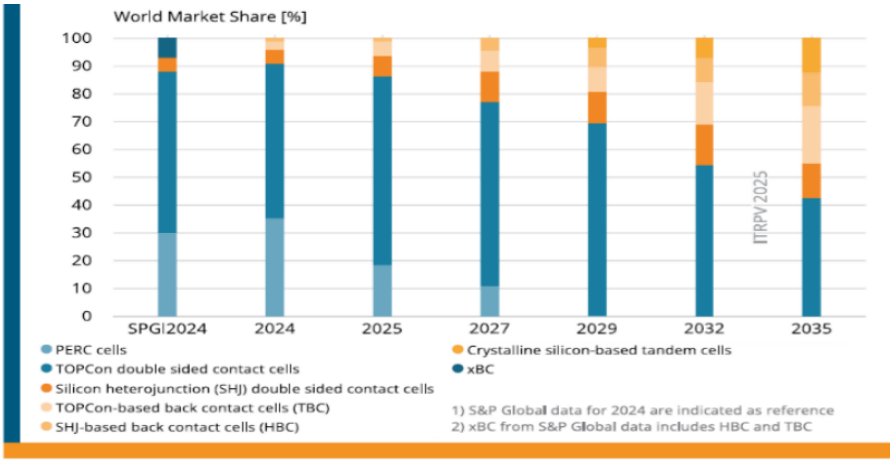

Figure 4. Market shares for different cell technologies from GW-scale manufacturers [4].

Despite substantial progress in photovoltaic deployment, challenges related to cell structure and ambient limitations remain.. PERC technology, while industrially mature, faces efficiency saturation and is increasingly affected by irradiation and degradation, constraining lifetime performance. TOPCon cells offer improved passivation but introduce challenges related to process complexity, contact resistivity, and cost scalability in mass production. Silicon heterojunction (SHJ) technologies achieve high efficiencies and favorable temperature coefficients; however, their reliance on low-temperature processing, indium-containing transparent conductive oxides, and tight manufacturing tolerances poses economic and supply chain constraints. The

competitive landscape of PV technology is thus shifting toward high-efficiency architectures that can balance performance, reliability, and cost. As global demand for clean energy accelerates, continuous innovation in materials, processes, and device architecture will determine the leading technologies in the next generation of solar photovoltaics. A comparison matrix of these technologies is given in **Figure 5** [3,5].

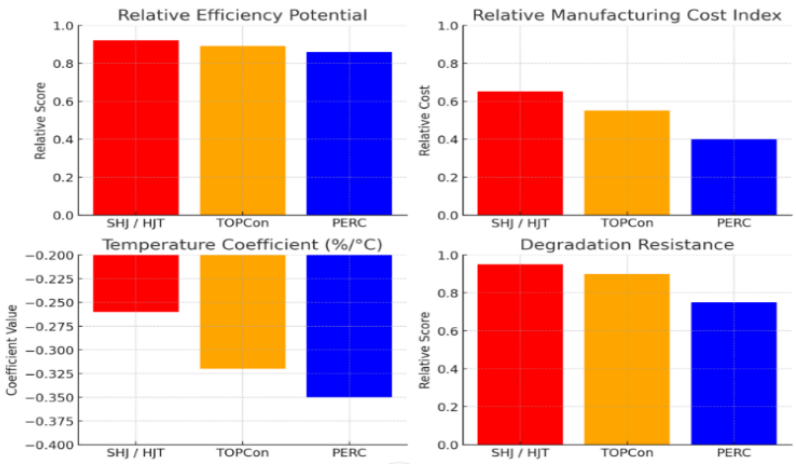

Figure 5. Comparison of PV cell technologies [3,5].

Kivambe et al. compared the performance of PERC, TOPCon, and SHJ PV modules operated for three years under Qatar's desert conditions, evaluating degradation rates, energy yields, and structural defects among other key parameters [5]. Zhou et al. proposed novel heterojunction architectures aimed at overcoming key technical limitations of PERC modules, which have emerged over the past decade as dominant players in the photovoltaic market [6]. Shen et al. conducted extensive investigations into mainstream approaches for enhancing solar cell efficiencies employed in photovoltaic modules [7]. Anderson et al. developed a comprehensive dataset by analyzing the parameters of fifteen distinct PV cell types intended for use within the PVsyst simulation software [8]. Chang et al. have provided a critical assessment of key materials employed in advanced photovoltaic technologies, particularly in PERC and TOPCon solar cells. Their analysis highlights material performance attributes, potential limitations, and implications for enhancing efficiency and durability [9]. Liu et al. emphasized that impedance spectroscopy enables the characterization of degradation processes in photovoltaic modules, offering valuable insights into performance decline. Their study further underscores its utility in comparing different PV cell types, thereby facilitating a deeper understanding of aging mechanisms and operational stability [10]. Xu et al. conducted research on photovoltaic panel performance, with a particular focus on TOPCon. Their study explored strategies to enhance efficiency, offering insights into technological optimizations and design improvements that can drive superior energy conversion in advanced PV architectures [11]. Liu et al. carried out investigations aimed at enhancing the performance of SHJ type photovoltaic panels. Their work focused on optimizing device architecture and material properties, thereby improving energy conversion efficiency and operational stability [12]. Li et al. investigated the influence of varying material thicknesses on UV resistance, with a specific focus on TOPCon photovoltaic cells. Their findings reveal critical

correlations between layer configuration and lifetime durability, offering guidance for improving reliability in advanced PV Technologies [13]. Liang et al. provided a comprehensive overview of solar cell evolution from silicon based PV panels to SHJ type technologies, examining how mechanical and other structural properties influence performance. Their analysis highlights the interplay between design parameters and efficiency, offering valuable perspectives for advancing PV module engineering [14]. Leung et al. investigated the evolution of photovoltaic panel technologies alongside an assessment of circular economy principles. Their study emphasizes sustainable material use, end-of-life management, and recycling strategies, linking technological advancement with environmental and economic resilience in the solar energy sector [15]. Yuan et al. examined performance and energy efficiency losses in PERC cells. Their research identifies key degradation mechanisms, quantifies their impact on lifetime output, and provides insights into mitigating efficiency decline through material and process optimization [16]. Gao et al. investigated the effect of doped materials on the efficiency of silicon solar cells. Their study demonstrates how controlled doping strategies can modify electronic properties, enhance carrier transport, and ultimately improve energy conversion efficiency [17]. Li et al. conducted an investigation into lead (Pb) content across 96 photovoltaic samples, including PERC panels. Their analysis evaluates the presence and distribution of Pb, highlighting implications for environmental safety, regulatory compliance, and sustainable management in PV technologies [18]. Öz et al. explored the optimization of PV panel manufacturing processes, focusing on the development of low-temperature lamination techniques for Perovskite/Si tandem structures. Their work aims to enhance structural integrity and performance while ensuring compatibility [19]. Chen et al. discussed advancements and technological innovations in screen printing within PV solar cell manufacturing. Their review highlights improvements in printing precision, paste formulations, and process integration, contributing to higher efficiency, reduced material waste, and enhanced scalability in photovoltaic production [20]. Karade et al. investigated the potential of inorganic tandem solar cells, outlining their advantages alongside the challenges that must be addressed. Their study highlights prospects for high efficiency and stability while emphasizing the need to overcome material compatibility, fabrication complexity, and barriers [21]. Khokhar et al. emphasized that achieving p-type TOPCon solar cells requires meticulous process optimization. Their findings underline the critical role of refining fabrication parameters to maximize energy conversion efficiency and ensure consistent performance in advanced PV technologies [22]. Zhang et al. investigated the use of carbon films in the production of solar cells. Their research demonstrates how carbon-based layers can enhance conductivity, and stability, offering a promising pathway for photovoltaic device engineering [23]. Wang et al. examined the impact of doping processes on the performance and efficiency of TOPCon solar cells. Their study reveals how optimized dopant selection and concentration can improve carrier lifetime, reduce recombination losses, and enhance overall energy conversion in advanced PV architectures [24]. Pirot-Berson et al. investigated the influence of structural layers on SHJ-type solar cells. Their research highlights how variations in layer composition, thickness, and interface quality affect carrier transport, recombination

dynamics, and overall device efficiency in photovoltaic systems [25]. Nasser et al. investigated the structural properties of PERC-type solar cells. Their study examines how layer configuration, material quality, and interface characteristics influence carrier dynamics and overall device performance, providing insights for optimizing efficiency and durability in advanced PV systems [26]. Jang et al. explored loss mechanisms and layer engineering in perovskite/Si tandem solar cells. Their research identifies critical factors affecting energy conversion efficiency and demonstrates how tailored layer design can mitigate losses, enhance carrier management, and optimize performance in photovoltaic devices [27]. Jäger et al. highlighted photovoltaic technology as a key instrument for achieving decarbonization, emphasizing its strategic role in the energy transition. Their assessment focuses on deployments, evaluating their potential to deliver substantial carbon reductions while supporting sustainable energy generation [28]. Brecl et al. investigated the performance of bifacial PV systems. Their study evaluates how varying irradiance components impact energy yield, providing a framework for more accurate performance prediction and optimization of bifacial photovoltaic installations [29]. ChenLi et al. examined the degradation reactions of TOPCon solar cells in acidic environments. Their investigation reveals the chemical and structural changes induced by acid exposure, offering insights into durability challenges and strategies for enhancing corrosion resistance in advanced PV technologies [30]. Du et al. conducted applications specifically on TOPCon type solar cells, analyzing their effects on performance and efficiency. Their findings demonstrate how targeted modifications in cell design and processing can enhance energy conversion, reduce losses, and improve operational stability in advanced photovoltaic systems [31]. Su et al. investigated silicon heterojunction solar cells, focusing on their energy conversion characteristics. Their research highlights the design advantages of solar architectures, demonstrating improved carrier collection, reduced recombination losses, and enhanced overall efficiency in photovoltaic applications [32]. Banerjee et al. investigated the structural properties of PERC-type solar cells, examining their influence on energy conversion efficiency. Their study identifies key design and material factors that affect performance, offering strategies to optimize structure for enhanced photovoltaic output [33]. Cao et al. examined the impact of back contacts on the efficiency of photovoltaic cells. Their research analyzes how contact design, material selection, and interface quality influence carrier transport and recombination, ultimately affecting overall energy conversion performance [34]. Kirchartz et al. studied the transition of PV solar cell efficiency from prototypes to commercial production. Their work addresses the performance gap, identifying factors such as material uniformity, process scalability, and defect control as critical to maintaining high efficiency in mass manufacturing [35]. Huang et al. conducted research on SHJ-type solar cells, which have recently emerged as one of the most advanced cell architectures. Their study explores material optimization, interface engineering, and fabrication techniques aimed at maximizing efficiency and operational stability [36]. Xu et al. examined the influence of individual layers on the efficiency of TOPCon solar cells. Their research highlights how variations in thickness, material properties, and interface quality can significantly impact carrier dynamics, recombination behavior, and overall energy conversion performance [37].

Hudişteanu et al. examined the influence of operating temperature on photovoltaic

panel performance. This study experimentally investigates monocrystalline and polycrystalline panels of identical nominal power (30 Wp) using a climatic chamber and solar simulator. Elevated temperatures notably reduce open circuit voltage, power output, and conversion efficiency, while cooling the panel's backside enhances performance. Results indicate a temperature coefficient of efficiency around −0.52%/°C and demonstrate differences between panel types due to material and spectral response. The findings underscore the potential of temperature management to optimize PV efficiency, supporting sustainable energy integration in building applications [38]. Karafil et al. stated PV panels convert solar energy directly into electrical energy through semiconductor materials. Panel performance is influenced by multiple factors, including tilt angle, shading, dust, wiring losses, solar radiation, and temperature, with the latter two being particularly significant. Solar radiation varies by panel location and time of day, directly affecting power output, whereas ambient temperature exhibits an inverse relationship with panel power. This study simulated the PV panel equivalent circuit in PSIM and MATLAB using catalogue data to investigate the effects of temperature and solar irradiance panel performance [39]. Wang et al. examined how solar spectral irradiance distributions (SIDs) critically influence on the photoelectric conversion performance of photovoltaic materials. This study evaluated the practical conversion efficiency of ten PV materials in Beijing and Changsha, China, using average photon energy. Photon energy utilization efficiency is proposed to compare performance across materials with identical aperture areas. Monocrystalline silicon performs best under reference spectra, whereas gallium arsenide excels when average photon energy exceeds 1.95 eV. Perovskite materials show variable mismatch factors depending on bandgap and spectral conditions. The study further proposes an ideal PV material optimized for regional SIDs, offering guidance for tailoring PV technologies to local solar spectra [40]. Bevanda et al. stated spectral irradiance is crucial for optimizing photovoltaic system performance. This study evaluated eight PV technologies across 79 European sites using satellite sky conditions. Results reveal systematic blue shifts in real spectra, with only 2–5% resembling AM1.5 reference conditions. Thin film technologies exhibit substantial spectral gains under blue-shifted spectra, whereas crystalline silicon variants maintain high stability (<1.6%). Latitude-dependent effects are influenced by air mass, water vapor, and aerosol content. The findings highlight the necessity of site spectral assessments to maximize energy yield and inform technology selection for diverse climates [41].

2. Materials and methods

In this study, PVsyst is employed as a robust energy yield calculation tool. Its advanced hourly simulation framework enables detailed modelling of thermal behaviour, system losses, shading, and component interactions. Owing to its validated databases and analytical depth, PVsyst constitutes a reliable platform for rigorous photovoltaic performance assessment. The selected provinces' map of case is given in **Figure 6**.

PVsyst simulations were conducted in Türkiye to estimate the electricity generation of PERC, TOPCon, and SHJ photovoltaic cell technologies across

provinces representing distinct climatic and geographical conditions. The selected cities, chosen for their characteristic environmental features, are illustrated on the Turkish Solar Energy Potential Atlas, underscoring their relevance for comparative photovoltaic performance assessment.

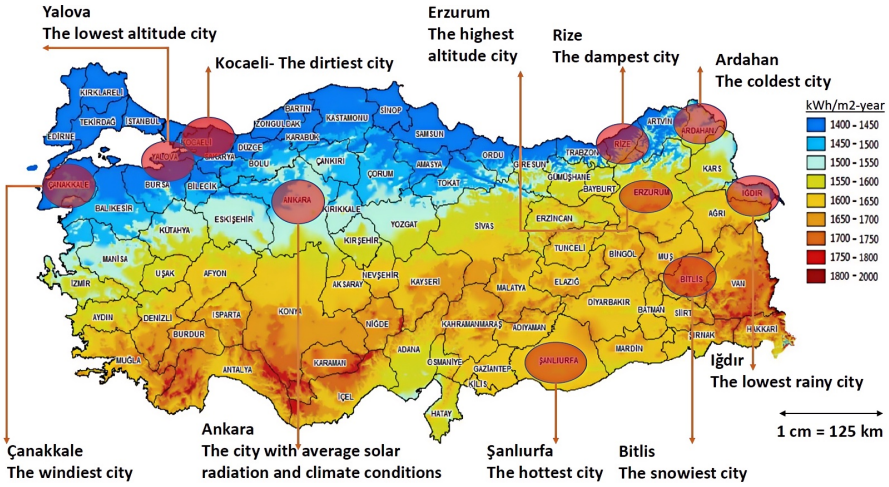

Figure 6. Selected provinces for PVsyst study case.

Ankara represents a semiarid continental climate typical of Central Anatolia. Ardahan and Erzurum exhibit severe high altitude continental climates, while Bitlis reflects eastern highland conditions with pronounced winter snowfall. Iğdır constitutes a low altitude microclimate within Eastern Anatolia, characterized by hotter summers and reduced precipitation. Çanakkale experiences a transitional Mediterranean/Marmara climate influenced by maritime effects. Kocaeli (Gebze) and Yalova represent humid Marmara climates with moderate seasonal variability. Rize exemplifies the humid Black Sea climate with persistent precipitation, whereas Şanlıurfa displays a hot semiarid climate marked by extreme summer temperatures and strong seasonal aridity. Key climatic parameters and altitudes are summarized in **Table 1**.

Table 1. Climatic parameter summary with altitudes.

Province	Climate type	Annual P.(mm)	Temp range (°C)	Altitude (m)	Notable features
Ankara	Semi-arid continental	350–400	−5 to 32	~938	Dry summers, spring rainfall peak
Ardahan	High-altitude continental	500–600	−20 to 25	~1800	Long, snowy winters
Erzurum	High-altitude continental	450–550	−20 to 26	~1900	Harsh winters, short mild summers
Bitlis	Mountain continental	800–1200	−10 to 27	~1540	Heavy winter snowfall
Çanakkale	Transitional Mediterranean–Marmara	600–700	5 to 30	~5	Maritime moderation
Kocaeli	Humid Marmara	700–900	4 to 30	~130	Even precipitation distribution
Iğdır	Semi-arid lowland continental	250–350	−5 to 35	~850	Mild winters for Eastern Anatolia
Rize	Humid subtropical (Black Sea)	2000–2500	7 to 28	~6	Year-round rainfall, orographic enhancement
Şanlıurfa	Hot-summer semi-arid	350–450	5 to 42	~518	Extreme summer heat, winter rainfall concentration
Yalova	Humid Marmara	800–1000	6 to 30	~2	Mild winters, warm summers

It clearly visualizes how provinces like Erzurum and Ardahan sit at the highest elevations, while Rize combines low altitude with extremely high precipitation, illustrating the strong maritime influence of the Black Sea. Iğdır remains low in precipitation despite its moderate altitude, reflecting its enclosed basin microclimate. The completed climate zone clustering chart showing the selected provinces positioned by altitude and annual precipitation, with colour coding for their respective climate types, is shown in **Figure 7**.

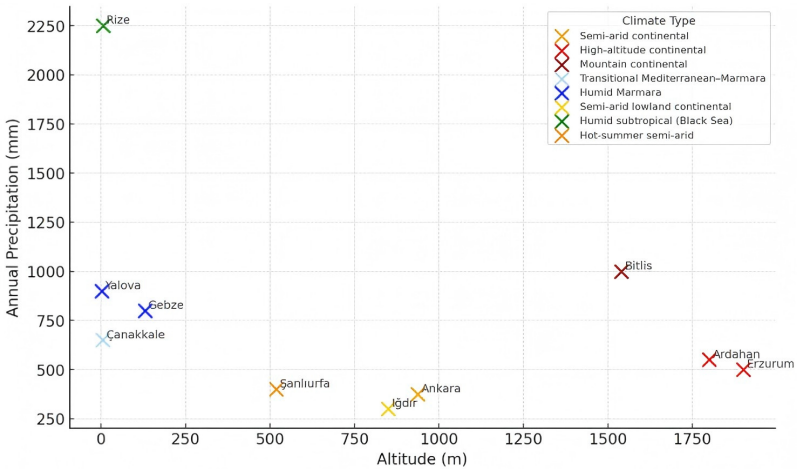

Figure 7. Climate zone clustering by altitude and precipitation.

Recent advancements in PV module manufacturing have resulted in diverse technological approaches, each optimized for specific performance, cost, and durability objectives. Among notable industry examples, Huasun Solar's DS585, JinkoSolar's JKM-585N-72HL4-BDV, and JinkoSolar's JKM585M-7RL4-V represent three distinct design philosophies: SHJ/HJT, TOPCon, and P-Type Monocrystalline PERC, respectively. Also, technical parameters of these cells are embedded in the PVsyst software program.

- Huasun Solar DS585: This model integrates SHJ cell architecture, which combines crystalline silicon wafers with thin amorphous silicon layers. The design aims to minimize recombination losses, enhance bifaciality, and maintain superior temperature coefficients. Its n type base structure provides immunity to light induced degradation (LID).
- JinkoSolar JKM-585N-72HL4-BDV: Employing n-type TOPCon technology, this module focuses on achieving high conversion efficiencies through advanced passivation and optimized carrier transport. TOPCon cells typically exhibit improved performance under low irradiance, superior bifacial gains, and better degradation resistance compared to standard PERC designs.
- JinkoSolar JKM585M-7RL4-V: This model uses p type monocrystalline cells, typically associated with PERC enhancements. While more mature and cost-efficient to manufacture, p-type cells are more susceptible to LID and have slightly lower efficiency ceilings compared to n type technologies. However, they remain a reliable choice for projects prioritizing proven performance and lower upfront costs [3,5,6]. A technical feature comparison of cells is given in **Table 2**.

Table 2. Technical feature comparison.

Model	Cell type	Base wafer type	Technology	Potential limitations
Huasun Solar DS585	SHJ/HJT	N-Type	Heterojunction	Higher manufacturing complexity and cost
JinkoSolar JKM-585N-72HL4-BDV	TOPCon	N-Type	Passivating Contact	Slightly higher cost than PERC; emerging large-scale manufacturing base
JinkoSolar JKM585M-7RL4-V	P-Type Monocrystalline (PERC)	P-Type	Passivated Emitter and Rear Cell	Light-induced degradation (LID) risk, lower efficiency potential than n-type

3. Results and discussion

The assumptions adopted in this study are as follows:

- For the PERC cell type, the JinkoSolar JKM585M-7RL4-V PV module was used; for the TOPCon cell type, the JinkoSolar JKM-585N-72HL4-BDV PV module was employed; and for the SHJ cell type, the Huasun Solar DS585 PV module was selected.
- Calculations were performed for the ten previously specified cities.
- In PVsyst, the technical parameters of the aforementioned PV cell types are embedded within the software's database.
- All simulations were conducted assuming an installed capacity of 1 MW.
- The nominal PV module power was set at 585 W for all three cell types.
- A Huawei inverter with a nominal capacity of 200 kW was used in all cases.
- In PVsyst, only the PV cell type was varied to determine the resulting energy output; all other parameters and site-specific conditions for each location were kept constant, in line with the ceteris paribus assumption.

A detailed sample of PVsyst result is given in **Figures 8–11** for Şanlıurfa province.

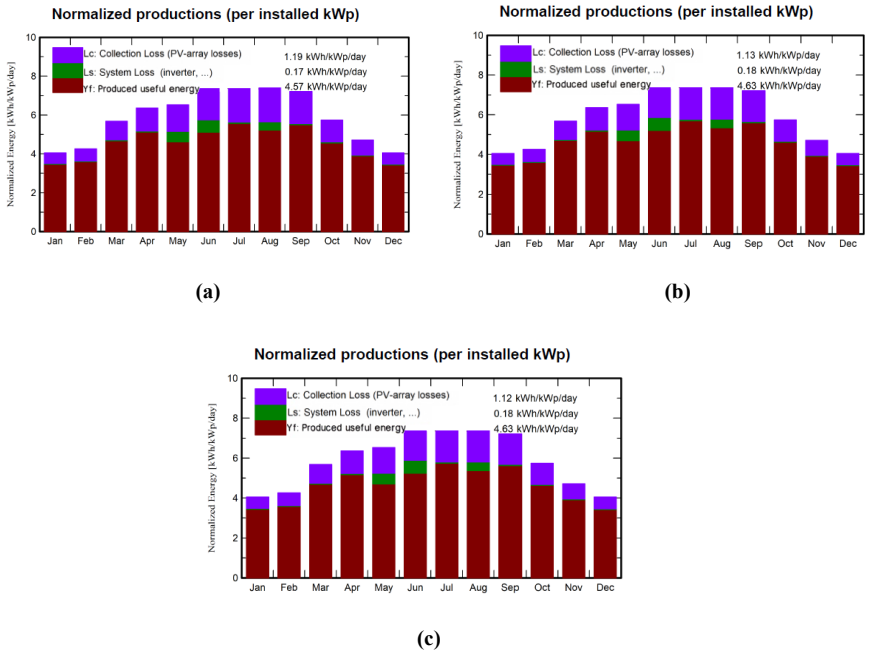

Figure 8. System generation results for Şanlıurfa province: **(a)** PERC; **(b)** TOPCon; **(c)** SHJ.

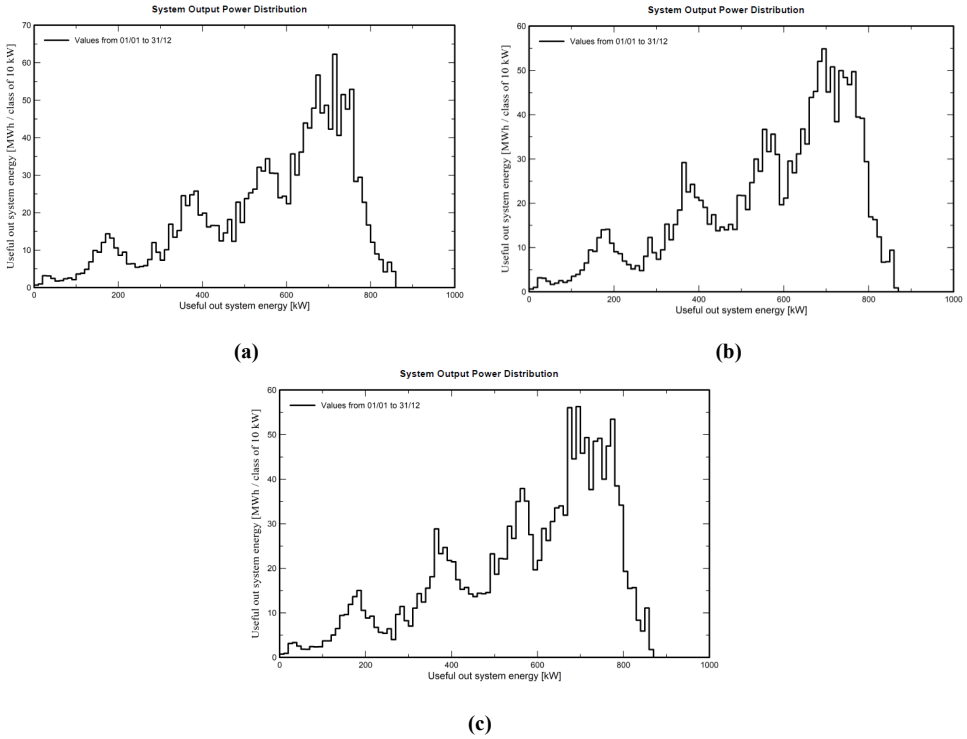

Figure 9. System output power distribution for Şanlıurfa province: **(a)** PERC; **(b)** TOPCon; **(c)** SHJ.

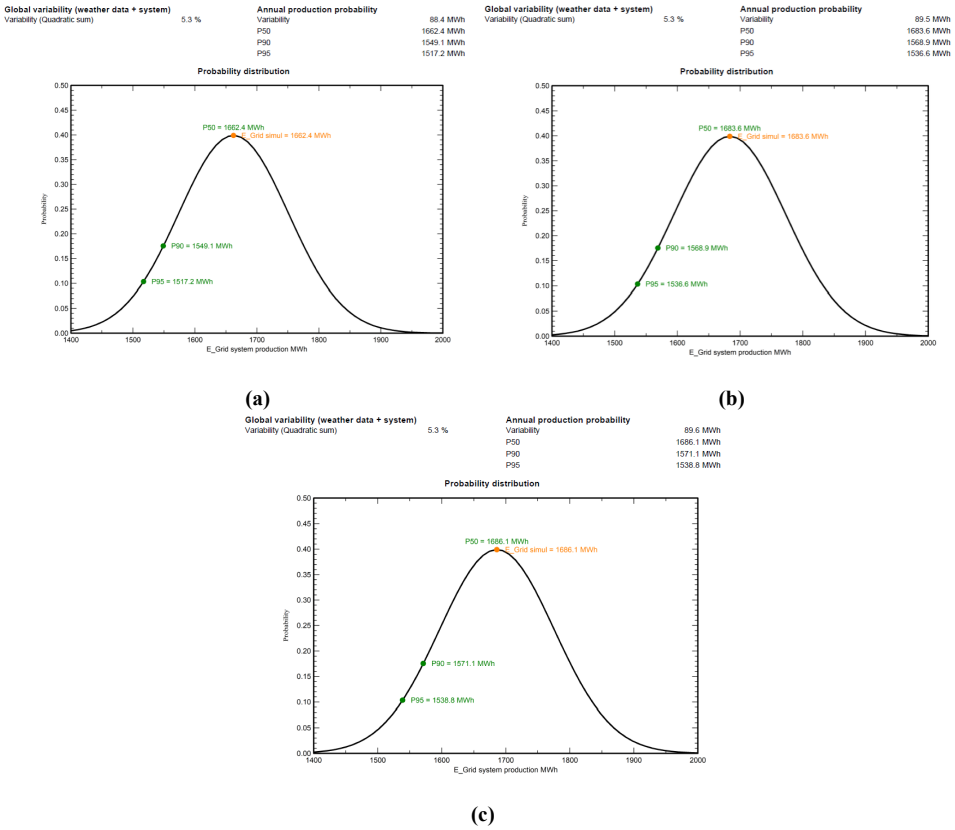

Figure 10. Probability distribution for Şanlıurfa province: **(a)** PERC; **(b)** TOPCon; **(c)** SHJ.

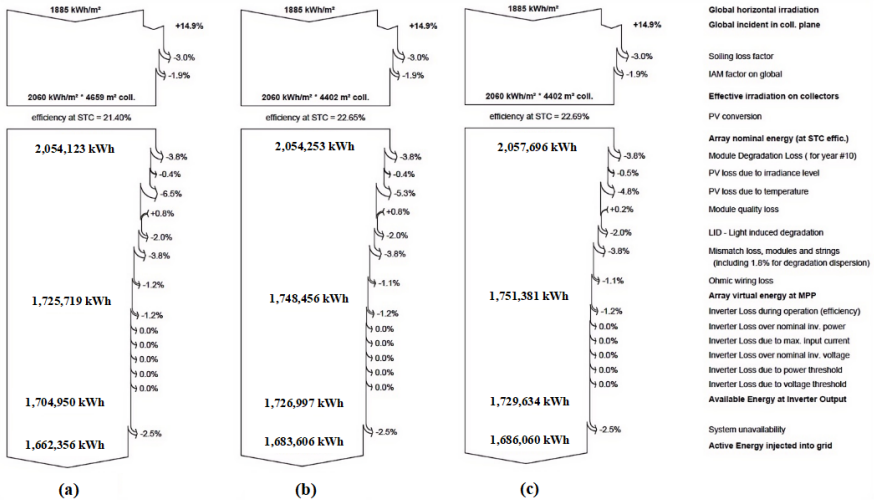

Figure 11. Loss diagram of systems: **(a)** PERC; **(b)** TOPCon; **(c)** SHJ.

The following **Table 3** presents recorded annual PV production (MWh) by technology across select Turkish provinces, each uniquely defined by a climate characteristic.

Table 3. A summary of the PVsyst study.

Province	Climate feature	PERC (MWh)	TOPCon (MWh)	SHJ (MWh)
Ankara	Moderate continental	1567.2	1577.5	1576.0
Ardahan	Coldest winters (high elevation)	1636.4	1639.3	1634.4
Bitlis	Snowiest, mountainous	1766.3	1775.7	1773.2
Çanakkale	Windy coastal terrain	1462.5	1473.9	1473.0
Kocaeli	High air pollution	1274.1	1283.3	1282.6
Iğdır	Low precipitation, dry basin	1322.1	1332.3	1331.6
Rize	Wettest, humid	1369.3	1377.5	1375.6
Şanlıurfa	Hottest summer region	1662.4	1683.6	1686.1
Yalova	Lowest elevation, coastal	1304.5	1293.5	1304.5
Erzurum	Highest elevation, frigid winters	1789.9	1795.3	1791.0

According to the PVsyst result:

- SHJ modules consistently lead in conversion efficiency (lab scale ~26.8%) thanks to superior surface passivation and high open-circuit voltage [5]. SHJ exhibits superior thermal resilience (temperature coefficient ~0.23%/°C), maintaining performance in high temperature environments [42,43]. SHJ modules suffered up to high performance loss over three years, largely due to encapsulant degradation and delamination. SHJ is ideal where efficiency peaks matter, high irradiance sites (e.g., Şanlıurfa).
- TOPCon follows closely with ~26% efficiency, enhanced carrier selectivity, and low degradation properties. TOPCon shows moderate temperature sensitivity, outperforming PERC in hot climates. TOPCon demonstrated remarkable reliability; one module endured only relatively low degradation. TOPCon is a resilient all-rounder excelling in high elevation, high humidity, windy, or polluted environments due to superior temperature stability and lifetime durability.
- PERC modules, while more affordable and widely deployed, retain comparatively

lower efficiency (~23.3%). PERC is most affected by heat, with higher performance decay in hotter conditions. PERC experienced high initial degradation that later stabilized. An effective baseline option for stable, moderate climates or low-budget scenarios, though with lower yield potential under stress.

A heatmap diagram is given in **Figure 12** for PVsyst results.

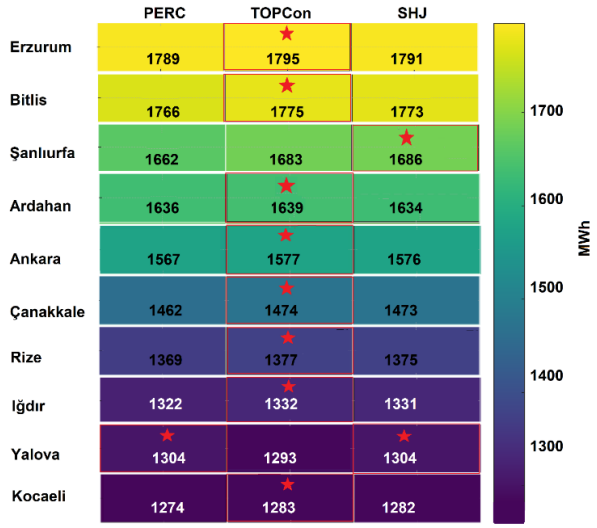

Figure 12. Heatmap diagram of PVsyst results.
Note: The red starred entries indicate the maximum values observed within each row.

Türkiye's abundant solar resource makes large scale PV deployment strategically compelling, yet climate sensitive technology choice is decisive. Rising heat and extremes increasingly constrain performance. Aligning SHJ with hot, high irradiance regions, TOPCon with harsh or variable climates, and PERC with stable zones maximizes energy yield, resilience, and long term system reliability nationwide sustainably. A summary is given in **Table 4.**

Table 4. A summary of PV technology-climate fit.

Technology	Key strengths	Ideal climate fit(s)
TOPCon	High efficiency, lowest degradation in harsh climates, moderate temp sensitivity	High-altitude, humid, dusty, coastal, snowy (most provinces)
SHJ (HJT)	Highest efficiency, best thermal coefficient	Hot climates (e.g., Şanlıurfa) despite degradation risk
PERC	Most cost-effective, mature technology	Moderate climates (e.g., Yalova) under lower stress

4. Discussion

Photovoltaic electricity generation in Türkiye displays pronounced spatial heterogeneity, reflecting the combined influence of solar availability and region's climatic conditions. An assessment of provinces including Kocaeli, Yalova, Iğdır, Rize, Çanakkale, Ankara, Ardahan, Şanlıurfa, Bitlis, and Erzurum demonstrates that cumulative PV output is governed by the interaction of altitude, ambient temperature, humidity, air quality, and irradiance. Provinces such as Kocaeli and Yalova exhibit the lowest total production, consistent with the adverse effects of dense industrial aerosols and low elevation, both of which are known to suppress effective solar irradiance and module performance.

Erzurum records the highest production levels, attributable to its high altitude and cool thermal regime. Reduced operating temperatures at elevated sites are widely reported to enhance PV efficiency, in some cases exceeding 40% gains relative to lowland, warmer environments. Provinces characterized by high humidity and frequent precipitation, notably Rize and Bitlis, achieve intermediate to high production levels. Although atmospheric moisture can attenuate incoming radiation and increase module temperatures, adequate solar availability compensates for these losses, sustaining robust generation.

Thermal conditions emerge as a critical determinant of technology performance. In Şanlıurfa, where irradiance is intense but ambient temperatures are elevated, PERC modules deliver slightly lower outputs than TOPCon and SHJ technologies. This pattern reflects the higher temperature coefficient and thermal sensitivity of PERC architectures. Similar constraints are observed in industrialized urban settings such as Kocaeli, where particulate pollution reduces optical transmittance and further limits yield.

Provincial PV performance in Türkiye is shaped by a convergence of climatic drivers. Cooler, high altitude environments favor technologies with strong thermal tolerance, while humid regions benefit from maintenance strategies that mitigate moisture and soiling losses. High irradiance zones consistently outperform others, yet only when thermal and atmospheric effects are adequately managed. These findings indicate that maximizing PV yield in Türkiye requires climate fit technology selection and region's operational strategies, rather than reliance on solar resource magnitude alone.

5. Conclusion

A comparative evaluation of photovoltaic electricity generation across Turkish provinces, conducted for PERC, TOPCon, and SHJ (HJT) cell architectures, provides a structured perspective on the interaction between climate, technology choice, and modeling methodology in energy system assessment. All yield estimates were derived using PVsyst, a widely established platform for PV system design and performance prediction. To ensure methodological rigor, irradiance datasets, meteorological inputs, thermal formulations, shading assumptions, and loss factors were maintained identically across simulations; the PV cell technology constituted the sole variable. This ceteris paribus framework enables a transparent comparison of technology fit behavior, independent of confounding parameter shifts, while acknowledging that variability may exceed what numerical models can fully resolve.

PVsyst employs advanced physical representations, including one-diode electrical models, cell temperature formulations, and standardized meteorological databases such as Meteonorm and PVGIS, to generate internally consistent and reproducible outputs. Within this controlled environment, provinces at higher elevation and with cooler ambient conditions, notably Erzurum, consistently achieve the highest simulated production across all module categories. In contrast, low altitude or industrialized provinces such as Kocaeli and Yalova exhibit the lowest yields, reflecting the well documented effects of elevated module temperatures, atmospheric pollution, and

soiling on PV performance.

Despite the internal consistency of these simulations, deviations are expected under operational conditions. Factors such as long term degradation, dust accumulation, ultraviolet exposure, and localized microclimatic dynamics introduce uncertainties that are only partially captured by numerical tools. Even so, PVsyst's modeling framework offers a reliable comparative baseline, particularly valuable during early stage feasibility analysis, where relative performance trends are more critical than absolute yield values.

The results highlight the necessity of aligning PV technology characteristics with regional climatic conditions in procurement and investment decisions. In high temperature environments such as Şanlıurfa, SHJ modules, distinguished by low temperature coefficients and enhanced thermal stability, display a relative performance advantage over thermally sensitive PERC designs. In humid or snow affected regions, including Rize and Bitlis, technologies exhibiting strong low irradiance response and resilience to soiling, often SHJ or well passivated TOPCon variants, are more likely to sustain superior output in practice. Consequently, module selection should extend beyond nominal efficiency or cost considerations to incorporate the interaction between cell physics and local climate.

The ceteris paribus simulations conducted in PVsyst establish an essential reference under equalized conditions, enabling objective technology comparison. Final system design and technology choice, however, must be refined using site's parameters encompassing irradiance regimes, temperature distributions, altitude, soiling intensity, and maintenance strategies. Integrating high-fidelity simulation outcomes with regional climatic intelligence ultimately supports more reliable, resilient, and economically robust photovoltaic deployments across Türkiye's diverse geographic landscape.

Funding: This work was carried out without financial support from any funding agency, public or private.

Institutional review board statement: Not applicable.

Informed consent statement: This study did not involve human participants; therefore, informed consent was not applicable.

Data availability statement: The data used in this study are available from the corresponding author upon reasonable request.

Acknowledgment: The authors acknowledge the valuable feedback provided by the anonymous reviewers.

Conflict of interest: The author declares no conflict of interest.

References

1. International Renewable Energy Agency (IRENA). Renewable Power Generation Costs in 2024. International Renewable Energy Agency; 2025.
2. International Energy Agency (IEA). World Energy Outlook 2024. International Energy Agency; 2024.

3. Zhang Y, Kim M, Wang L, et al. Design considerations for multi-terawatt scale manufacturing of existing and future photovoltaic technologies: challenges and opportunities related to silver, indium and bismuth consumption. Energy and Environmental Science. 2021; 14: 5587–5610. doi: 10.1039/D1EE01814K
4. VDMA. International Technology Roadmap for Photovoltaics (ITRPV), 16th ed. VDMA; 2025.
5. Kivambe M, Abdallah A, Figgis B, et al. Comprehensive assessment of performance and reliability of PERC, TOPCon and SHJ modules in desert climates. Solar Energy. 2025; 295: 113555. doi: 10.1016/j.solener.2025.113555
6. Zhou Z, Kang Q, Sun Z, et al. Optimization strategies and efficiency prediction for silicon solar cells with hybrid route of PERC and SHJ passivation contact. Advanced Science. 2025; 12(15): 2411965. doi: 10.1002/advs.202411965
7. Shen W, Zhao Y, Liu F. Highlights of mainstream solar cell efficiencies in 2024. Frontiers in Energy. 2025; 19: 8–17. doi: 10.1007/s11708-025-0985-5
8. Anderson KS, Hansen CW, Theristis M. A noniterative method of estimating parameter values for the PVsyst version 6 single-diode model from IEC 61853-1 matrix measurements. IEEE Journal of Photovoltaics. 2025; 15(3): 492–499. doi: 10.1109/JPHOTOV.2025.3554338
9. Chang YC, Zhang Y, Wang L, et al. Silver-lean metallization and hybrid contacts via plating on screen-printed metal for silicon solar cells manufacturing. Progress in Photovoltaics: Research and applications. 2025; 33(1): 158–169. doi: 10.1002/pip.3799
10. Liu M, Cao X, Wang L, et al. Characterizing photovoltaic module power degradation through impedance spectroscopy: Transitioning to outdoor applications. Renewable Energy. 2025; 252: 123438. doi: 10.1016/j.renene.2025.123438
11. Xu W, Zhou P, Xiu Q. Optimizing the manufacturing process to increase fill factor and elevate efficiency of N-type crystalline silicon TOPCon solar cells. AIP Advances. 2025; 15(6), 065009. doi: 10.1063/5.0270347
12. Liu Y, Peters IM, Ding K, et al. Silver reduction through direct wire bonding for Silicon Heterojunction solar cells. Solar Energy Materials and Solar Cells. 2025; 282: 113412. doi: 10.1016/j.solmat.2025.113412
13. Li Z, Yu K, Zhu Q, et al. UVID of TOPCon Solar Cells: Effect of the Front Passivation Al2O3 layer thickness and recovery by different processes. Solar Energy Materials and Solar Cells. 2025; 289: 113691. doi: 10.1016/j.solmat.2025.113691
14. Liang B, Chen X, Wang X, et al. Progress in crystalline silicon heterojunction solar cells. Journal of Materials Chemistry A. 2025; 13(4): 2441–2477. doi: 10.1039/D4TA06224H
15. Leung TL, Willson GK, Fimbres-Weihs G, et al. A new perspective for evaluating circularity of photovoltaic module recycling and technology developments. Cell Reports Physical Science. 2025; 6: 102547. doi: 10.1016/j.xcrp.2025.102547
16. Yuan D, Cui J, Ding J, et al. Efficiency loss analysis and simulation of 23.2% efficiency PERC cell. Optical and Quantum Electronics. 2025; 57: 216. doi: 10.1007/s11082-025-08136-w
17. Gao K, Xu D, Wang J, et al. Efficient silicon solar cells with aluminum-doped zinc oxide-based passivating contact. Advanced Functional Materials. 2025; 35: 2415039. doi: 10.1002/adfm.202415039
18. Li F, Tatapudi SR, Shaw SL, et al. Photovoltaic module leach testing: Database development and statistical analysis. Journal of Environmental Management. 2025; 377: 124666. doi: 10.1016/j.jenvman.2025.124666
19. Öz AK, Neven-du Mont S, Nikitina V, et al. Pushing the boundaries: Challenges that arise in manufacturing and designing photovoltaic modules for new application areas. Solar Energy Materials and Solar Cells. 2025; 291: 113735. doi: 10.1016/j.solmat.2025.113735
20. Chen N, Liu Y, Shao Y, et al. Review of the latest industrial progress in screen printing. Solar Energy Materials and Solar Cells. 2025; 290: 113734. doi: 10.1016/j.solmat.2025.113734
21. Karade VC, He M, Song Z, et al. Opportunities and challenges for emerging inorganic chalcogenide–silicon tandem solar cells. Energy & Environmental Science. 2025; 18: 6899–6933. doi: 10.1039/D4EE04526B
22. Khokhar MQ, Yousuf H, Alamgeer, et al. Progressive development of n-poly-Si contacts and stencil refinement for high-efficiency p-TOPCon solar cells. International Journal of Precision Engineering and Manufacturing-Green Technology. 2025. doi: 10.1007/s40684-025-00755-8
23. Zhang L, Gao Q, Guo J, et al. High work function large-area carbon black films as conductive, passivated, and hole-selective heterocontact layer for highly efficient solar cells. Solar Energy. 2025; 296: 113590. doi: 10.1016/j.solener.2025.113590
24. Wang X, Sen C, Wu X, et al. Alleviating contaminant-induced degradation of TOPCon solar cells with copper plating. Solar Energy Materials and Solar Cells. 2025; 282: 113444. doi: 10.1016/j.solmat.2025.113444
25. Pirot-Berson L, Couderc R, Bodeux R, et al. Study and mitigation of moisture-induced degradation in SHJ

modules by modifying cell structure. Solar Energy Materials and Solar Cells. 2025; 285: 113557. doi: 10.1016/j.solmat.2025.113557
26. Nasser H, Altıner G, Çambay Kuban F, et al. Industrial PERC solar cells with fully passivated rear contact enabled by local hole-selective MoO_x/Ag. ACS Applied Energy Materials. 2025; 8(12): 7912–7918. doi: 10.1021/acsaem.4c03001
27. Jang YH, Lee Y, Seo HS, et al. Sacrificial layer concept interface engineering for robust, lossless monolithic integration of perovskite/Si tandem solar cells yielding high fill factor of 0.813. Nano Convergence. 2025; 12: 24. doi: 10.1186/s40580-025-00492-3
28. Jäger K, Aeberhard U, Llado EA, et al. Optics for terawatt-scale photovoltaics: Review and Perspectives. Advances in Optics and Photonics. 2025; 17: 185–294. doi: 10.1364/AOP.530556
29. Brecl K, Bokalič M, Faes A, Topič M. An accurate bifacial PV module energy performance model using a direct-diffuse power rating model. Applied Energy. 2025; 382: 125310. doi: 10.1016/j.apenergy.2025.125310
30. ChenLi Y, Sun Z, Yan D, et al. Degradation mechanism of TOPCon solar cells in an ambient acid environment. ACS Applied Materials & Interfaces. 2025; 17(7): 10776–10783. doi: 10.1021/acsami.4c21774
31. Du H, Zhang X, Liu W, et al. High-performance boron emitters for tunnel oxide passivating contact solar cells enabled by multi-layer PECVD-deposited boron source structures. Chemical Engineering Journal. 2025; 515: 163487. doi: 10.1016/j.cej.2025.163487
32. Su Q, Lin H, Wang G, et al. Contactless characterization of polarity boundary recombination on silicon heterojunction back contact solar cells. Solar Energy Materials and Solar Cells. 2025; 291: 113738. doi: 10.1016/j.solmat.2025.113738
33. Banerjee S, Das MK, Ahmed T, et al. Design and analysis of passivated n-Si solar cell employing SiC window layer. Silicon. 2025; 17: 1079–1089. doi: 10.1007/s12633-025-03252-4
34. Cao K, Yang Z, Wang M, et al. Physical mechanisms and design strategies for high-efficiency back contact tunnel oxide passivating contact solar cells. Solar Energy Materials and Solar Cells. 2025; 289: 113656. doi: 10.1016/j.solmat.2025.113656
35. Kirchartz T, Yan G, Yuan Y, et al. The state of the art in photovoltaic materials and device research. Nature Reviews Materials. 2025; 10(5): 335–354. doi: 10.1038/s41578-025-00784-4
36. Huang H, Du D, Li L, et al. Revealing the effect of phosphorus diffusion gettering on industrial silicon heterojunction solar cell. Solar Energy Materials and Solar Cells. 2025; 282: 113392. doi: 10.1016/j.solmat.2024.113392
37. Xu J, Zhang W, Li Y, et al. The impact of silicon surface pretreatment on interface structure and passivation quality of AlOx films deposited by atomic layer deposition. Solar Energy Materials and Solar Cells. 2025; 289: 113658. doi: 10.1016/j.solmat.2025.113658
38. Hudişteanu VS, Cherecheș NC, Țurcanu FE, et al. Impact of temperature on the efficiency of monocrystalline and polycrystalline photovoltaic panels: A comprehensive experimental analysis for sustainable energy solutions. Sustainability. 2024; 16(23): 10566. doi: 10.3390/su162310566
39. Karafil A, Ozbay H, Kesler M. Temperature and solar radiation effects on photovoltaic panel power. Journal of New Results in Science. 2016; 12: 48–58.
40. Wang S, Peng J, Wang M, et al. Evaluation of the energy conversion performance of different photovoltaic materials with measured solar spectral irradiance. Renewable Energy. 2023; 219(Part 1): 119431. doi: 10.1016/j.renene.2023.119431
41. Bevanda I, Marić P, Kristić A, et al. Assessing the impact of solar spectral variability on the performance of photovoltaic technologies across European climates. Energies. 2025; 18(14): 3868. doi: 10.3390/en18143868
42. Sen C, Wu X, Wang H, et al. Accelerated damp-heat testing at the cell-level of bifacial silicon HJT, PERC and TOPCon solar cells using sodium chloride. Solar Energy Materials and Solar Cells. 2023; 262: 112554. doi: 10.1016/j.solmat.2023.112554
43. Wang Q, Guo K, Gu S, et al. Electrical performance, loss analysis, and efficiency potential of industrial-type PERC, TOPCon, and SHJ solar cells: A comparative study. Progress in Photovoltaics: Research and Applications. 2024; 32: 889–903. doi: 10.1002/pip.3839

Energy Storage and Conversion 2025, 3(4), 3891.
doi: https://doi.org/10.59400/esc3891

Article

Comparative evaluation of green hydrogen production methods using the Pugh matrix technique

Afrin[1], Adeel H. Suhail[1], Fiseha M. Guangul[2], Abdalellah Mohmmed[2,*], Abdul Nazeer[1]

[1] Department of Civil and Mechanical Engineering, Middle East College, Muscat 124, Oman

[2] School of Engineering, Infrastructure and Sustainability, De Montfort University, Dubai P.O. Box 501870, United Arab Emirates

*** Corresponding author:** Abdalellah Mohmmed, abdalellah.mohammed@dmu.ac.uk

CITATION

Afrin, Suhail AH, Guangul FM, et al. Comparative evaluation of green hydrogen production methods using the Pugh matrix technique. Energy Storage and Conversion. 2025; 3(4): 3891. https://doi.org/10.59400/esc3891

ARTICLE INFO

Received: 29 September 2025
Revised: 3 November 2025
Accepted: 10 November 2025
Available online: 4 December 2025

Abstract: Hydrogen plays a vital role as an energy carrier in the global effort to combat climate change, with significant applications in sectors such as transportation and ammonia production. However, traditional hydrogen production methods are heavily carbon-intensive, with over 98% of hydrogen derived from fossil fuels. This primarily occurs through steam methane reforming (76%) and coal gasification (22%). While steam methane reforming is cost-effective, it generates approximately 9 kg of CO_2 per kg of hydrogen. Consequently, advancing green hydrogen production methods has become a critical area of research. This study explores and compares various green hydrogen production techniques powered by renewable energy sources, including solar, wind, hydro, biomass, and hybrid systems. Production methods such as electrolysis, thermal, chemical, photonic, and biological processes are evaluated using a Pugh matrix, accounting for factors including efficiency, hydrogen yield, resource availability, operating conditions, cost, and greenhouse gas emissions. The findings indicate that alkaline electrolysis currently represents the most viable option for green hydrogen production. These findings affirm alkaline electrolysis as the most appropriate near-term technology for large-scale green hydrogen implementation in Oman and the GCC, while also advocating for the ongoing development of PEM and emerging pathways to ensure long-term diversification. Ultimately, this study provides a clear and practical decision-support framework for the strategic selection of hydrogen technologies in renewable-rich arid regions.

Keywords: green hydrogen; Pugh matrix technique; renewable energy; fossil fuels; water splitting

1. Introduction

Global energy demand is rising due to population growth, industrial expansion, urbanization, and rapid technological advancement [1]. Currently, fossil fuels remain the predominant source of energy for electricity generation, transportation, and industrial processes, resulting in substantial emissions of greenhouse gases (GHGs) and air pollutants, including CO_2, NO_x, SO_x, and particulate matter [2]. The energy sector alone accounts for nearly three-quarters of global greenhouse gas emissions, thereby constituting the primary contributor to climate change [3]. In response, international initiatives have increasingly concentrated on attaining net-zero carbon emissions by 2050, with the aim of restricting the global temperature increase to 1.5 °C, as delineated in major global energy roadmaps [3]. Realizing these ambitious objectives necessitates a fundamental transformation of energy production systems, emphasizing a significant

transition toward low-carbon and carbon-free energy carriers.

Hydrogen offers unique advantages as an energy vector, including high gravimetric energy density, versatility in end-use applications, and zero carbon emissions at the point of use [4, 5]. Beyond its conventional role in ammonia and methanol production, hydrogen is increasingly recognized as a strategic medium for long-duration and seasonal energy storage and for sector coupling between electricity, industry, transport, and synthetic fuel production [6, 7]. In power-to-gas-to-power (P2G2P) systems, surplus renewable electricity can be converted into hydrogen via electrolysis, stored for extended periods, and reconverted to electricity or used as an industrial feedstock. Although the round-trip efficiency of such chains typically remains below 35–40%, hydrogen remains one of the few technically viable options for large-scale and seasonal energy storage [8–10]. Moreover, hydrogen–ammonia coupling provides an attractive pathway for long-distance energy transport and export, particularly in regions with established ammonia infrastructure and strong renewable resource potential [11, 12].

Recent state-of-the-art studies increasingly emphasize that hydrogen production technologies cannot be evaluated in isolation but must be assessed within integrated energy storage and conversion systems. Large-scale system analyses highlight electrolysis-based hydrogen as a cornerstone of future low-carbon energy systems, enabling long-duration storage, renewable curtailment mitigation, and sector coupling [13–16]. Techno-economic assessments indicate that alkaline and PEM electrolysis currently dominate commercial deployment, while solid oxide electrolysis remains at the demonstration stage due to durability and system-integration challenges. Parallel research underscores the growing importance of hydrogen conversion to ammonia and synthetic fuels to improve volumetric energy density, transportability, and export competitiveness, particularly for renewable-rich regions [17, 18].

Hydrogen can be utilized in transportation, power generation, industrial heating, and chemical manufacturing, particularly in ammonia and methanol production [19,20]. When produced using renewable energy sources, hydrogen, commonly referred to as “green hydrogen”, offers a pathway to deep decarbonization that is difficult to achieve through direct electrification alone. The current hydrogen production remains overwhelmingly carbon-intensive. More than 98% of global hydrogen production relies on fossil fuel–based methods, primarily steam methane reforming (SMR) and coal gasification, which collectively contribute substantial CO_2 emissions, approximately 9 kg of CO_2 per kg of hydrogen produced via SMR [21]. This reality has intensified global research efforts to identify sustainable, environmentally benign hydrogen production technologies powered by renewable energy sources such as solar, wind, hydropower, and biomass. The literature has extensively examined a diverse array of green hydrogen production technologies, encompassing water electrolysis (including alkaline, proton exchange membrane, and solid oxide methods), thermochemical water splitting, photonic processes, and biomass-based pathways [4, 21–23]. These technologies differ significantly in terms of efficiency, hydrogen yield, operating conditions, cost, resource availability, and technological maturity. While many studies have focused on thermodynamic, techno-economic, or exergy-based evaluations of individual hydrogen

production routes [23–25], fewer have addressed the comparative selection problem: how to systematically identify the most suitable green hydrogen production method when multiple, often conflicting, criteria must be considered simultaneously.

Existing comparative studies often utilize sophisticated multi-criteria decision-making (MCDM) tools, such as AHP, TOPSIS, or fuzzy-based methodologies. While these tools are highly effective, they necessitate extensive data, hierarchical structuring, and expert judgment, which may not always be readily accessible, particularly in the context of emerging hydrogen markets [4, 22]. Consequently, there is a practical necessity for transparent and low-complexity decision-making frameworks that can facilitate early-stage planning, policy development, and technology evaluation. Moreover, a significant gap exists in the regional contextualization of green hydrogen technology selection. The majority of published studies adopt a global or generic perspective, with limited consideration of country-specific factors such as renewable resource availability, water constraints, infrastructure readiness, and economic priorities. This limitation is particularly pertinent for countries in the Middle East and North Africa (MENA) region, where renewable energy potential is substantial, yet techno-economic and environmental conditions vary considerably across locations.

Oman represents a strategically essential and underexplored case for green hydrogen deployment. The country has one of the world's highest levels of solar irradiation, ample land, and strong ambitions to diversify its energy mix and reduce dependence on fossil fuels. At the same time, Oman faces challenges related to water scarcity, infrastructure development, and cost competitiveness, making the selection of an appropriate hydrogen production technology a critical decision [26, 27]. Choosing a suboptimal technology could lead to high costs, inefficient resource utilization, or delayed adoption, undermining national decarbonization objectives. Despite these strategic considerations, there is a lack of structured, technology-selection studies specifically tailored to Oman's context. Existing research largely focuses on resource assessments or individual technology analyses, without offering a systematic comparison of green hydrogen production pathways that balances technical performance, economic feasibility, operational conditions, and environmental impact.

To bridge this gap, the present study uses the Pugh matrix decision-making technique to assess 15 green hydrogen production methods against six critical criteria: efficiency, hydrogen yield, raw material availability, required operating conditions, cost, and greenhouse gas emissions. The Pugh matrix is selected for its simplicity, transparency, and appropriateness for early-stage technology evaluation, rendering it particularly advantageous for policymakers, planners, and engineers in nascent hydrogen economies. This study offers a comprehensive comparative analysis of major green hydrogen production technologies through a structured yet accessible decision-making framework. It highlights the trade-offs among competing technologies across multiple performance criteria, thereby facilitating a clearer understanding of their relative strengths and limitations. Additionally, it provides insights specific to Oman to support strategic decision-making for sustainable hydrogen deployment. By addressing both methodological and regional gaps, this work aims to support informed and pragmatic decisions toward the large-scale adoption of green hydrogen in Oman and other regions

rich in renewable resources.

2. Materials and methods

This study employs a structured multi-criteria evaluation framework to identify the most suitable green hydrogen production technology, accounting for technical, economic, and environmental considerations. The methodology integrates a comprehensive review of green hydrogen production pathways with a Pugh matrix decision-making technique to rank alternative technologies transparently and systematically. An extensive review of peer-reviewed journal articles, International Energy Agency reports, and recent review studies was conducted to identify relevant green hydrogen production pathways [4, 5, 21, 28]. Based on this review, fifteen hydrogen production methods were selected for evaluation, representing the most prominent renewable-based and low-carbon hydrogen production routes discussed in the literature. The identified technologies were classified into five major categories: electrolysis-based processes, thermolysis and thermochemical water-splitting processes, photonic processes, biological biomass-based processes, and thermochemical biomass-based processes. This classification facilitates a systematic comparison across fundamentally different production mechanisms while ensuring comprehensive coverage of current green hydrogen technologies. The overall classification of green hydrogen production technologies is illustrated in **Figure 1**, adapted from [22,29].

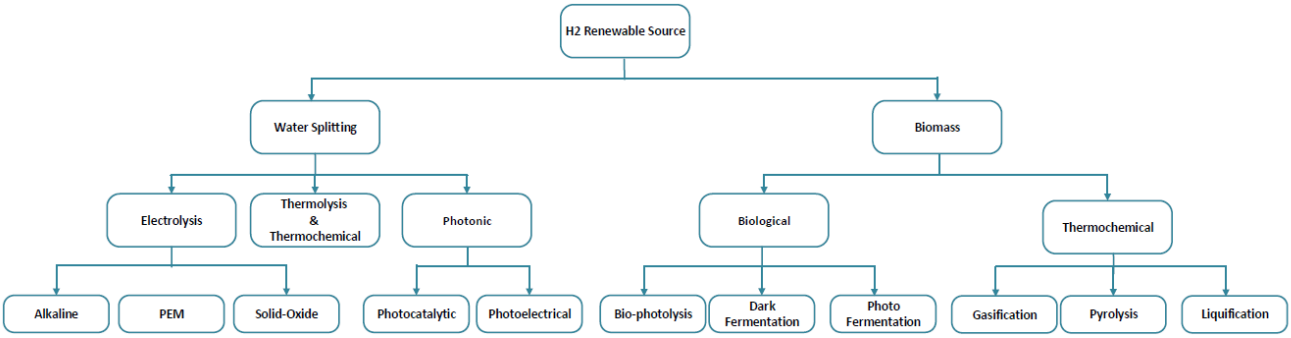

Figure 1. Green hydrogen production technologies.

2.1. Electrolysis

Electrolysis is a process in which water is decomposed into hydrogen and oxygen gases at two electrodes immersed in a liquid medium. The electrochemical cell, comprising solely pure water and two electrodes connected to an external power source, constitutes the core of an electrolysis unit. Upon reaching the critical voltage between the electrodes, hydrogen gas is generated at the cathode, which is negatively charged, while oxygen gas is produced at the anode, which is positively charged.

There are primarily three types of water electrolysis: (a) Alkaline Electrolysis. Alkaline water electrolysis was the first commercially viable water electrolysis technology and remains the most prevalent today. This method utilizes energy to dissociate water molecules into hydrogen and oxygen, with the requisite electrical energy for producing green hydrogen potentially sourced from renewable energy [30]. (b) Proton

Exchange Membrane (PEM) Electrolysis. The proton exchange membrane (PEM) water electrolysis technique, initially developed by General Electric for fuel cell applications and subsequently for electrolysis, employs a polymeric proton exchange membrane as the solid electrolyte. Nafion is the most widely used membrane, consisting of a sulfonated fluorinated polymer. The thickness of the Nafion membrane ranges from 25 to 250 μm, with the specific thickness required for a given application determined by the operating conditions of the electrolyzer. The efficiency of electrolysis is enhanced with increased membrane thickness. (c) Solid Oxide Electrolysis (SOE). Solid oxide electrolysis (SOE) is increasingly recognized for its enhanced capability to generate ultra-pure hydrogen and convert electrical energy into chemical energy. The operational temperature of a solid oxide electrolyzer, typically ranging from 800 to 1000 °C, sets it apart from both alkaline and proton exchange membrane (PEM) systems. At these elevated temperatures, steam is introduced into the electrolyzer instead of water. The primary components of SOE include two porous electrodes and a dense ionic conducting electrolyte. Yttria-stabilized zirconia (YSZ) is the most frequently utilized electrolyte in SOE, owing to its robust mechanical strength and high oxygen-ion conductivity [31,32]. The schematic diagrams for alkaline electrolysis, PEM electrolysis, and Solid oxide electrolysis are shown in **Figure 2**.

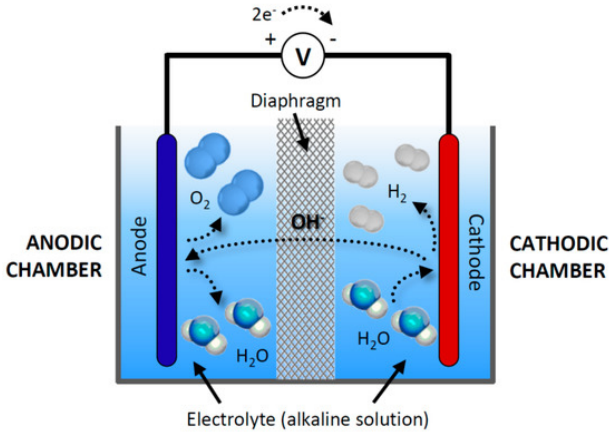

(a)

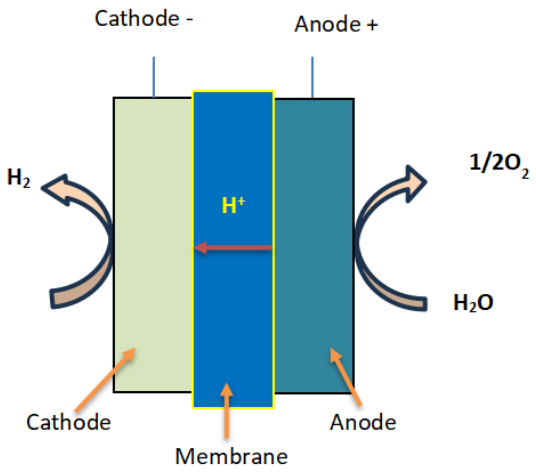

(b)

Figure 2. *Cont.*

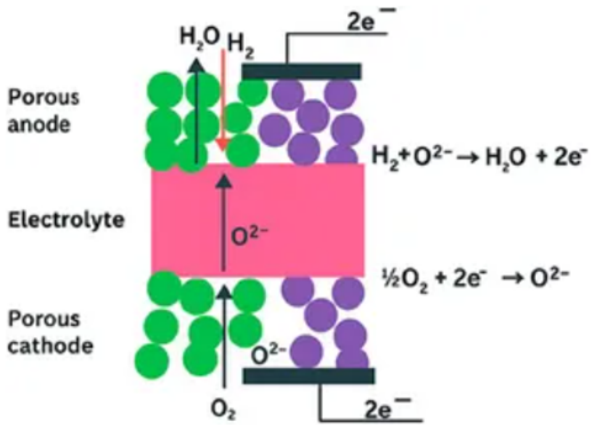

(c)

Figure 2. **(a)** Alkaline electrolyser [33]; **(b)** PEM electrolysis; **(c)** Solid oxide electrolysis [34].

2.2. Thermolysis and thermochemical water splitting

Thermolysis and thermochemical water splitting are methodologies that employ thermal energy to produce hydrogen from water. Thermolysis is a single-step process that involves the dissociation of water and necessitates a high-temperature energy source exceeding 2500 K. It is crucial to achieve adequate dissociation to prevent the formation of an explosive mixture. This requirement imposes stringent demands on the materials due to the extremely high temperatures involved. Thermochemical water splitting, in contrast, entails a sequence of cyclic chemical reactions that ultimately result in the dissociation of water into hydrogen and oxygen. Notably, this process frequently does not necessitate the use of a catalyst or a membrane for the separation of hydrogen and oxygen. The operational temperature generally ranges from 600 to 1200 K. Employing higher temperatures reduces the number of cycles required for thermochemical water splitting. Moreover, the incorporation of electrical energy to facilitate the process introduces the concept of hybrid cycles [35]. Various chemicals and metals can be employed in distinct thermochemical water splitting cycles. Notably, the two-step and three-step thermochemical cycles represent the fundamental forms [36, 37]. **Figure 3** shows the thermolysis reaction of thermochemical water-splitting processes.

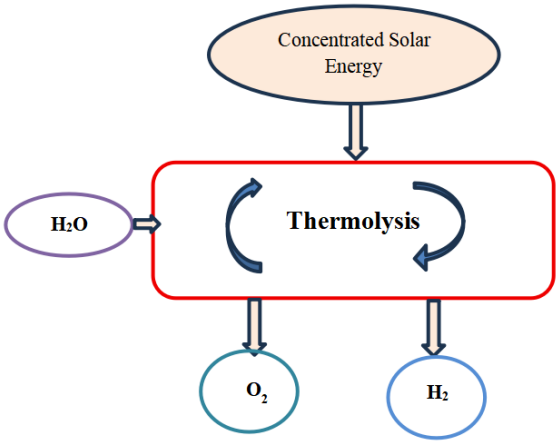

Figure 3. Thermolysis reaction.

In the two-step thermochemical cycles depicted in **Figure 4**, a metal oxide in a low valence state can undergo reduction to form the metal and release oxygen. Alternatively, a metal oxide with a higher valence state may be reduced to produce a metal oxide with a lower valence state. In this process, a temperature range of 1700–3000 K must be supplied by the heat source, and a solar collector can be utilized to harness concentrated solar radiation. To date, the primary limitations of this type of thermochemical cycle include the necessity of materials that can withstand very high temperatures and the relatively lower efficiency of two-step thermochemical cycles compared to electrolysis [37].

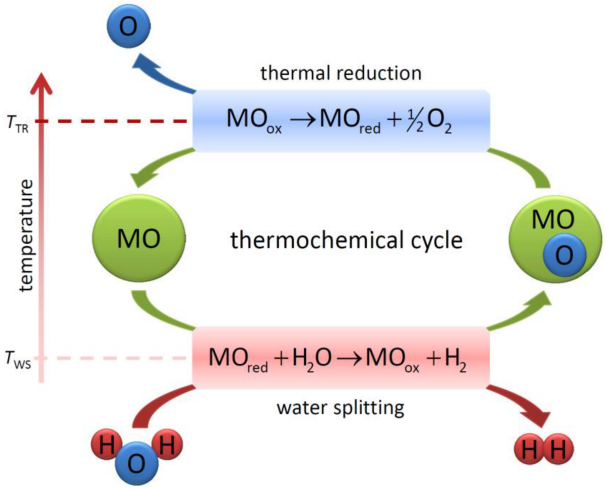

Figure 4. Two-step thermochemical metal oxide cycle [38].

Three-step processes can be derived from two-step processes by replacing the reaction that occurs at the highest temperature with a two-step reaction process. This alteration serves to lower the maximum temperature requirement for the cycle. The Sulphur-Iodine (S-I) cycle, also referred to as the General Electric cycle, is the most prominent example within this category. It was initially proposed in the 1970s by General Electric [37]. A schematic diagram of the Hybrid Sulfur cycle is presented in **Figure 5**.

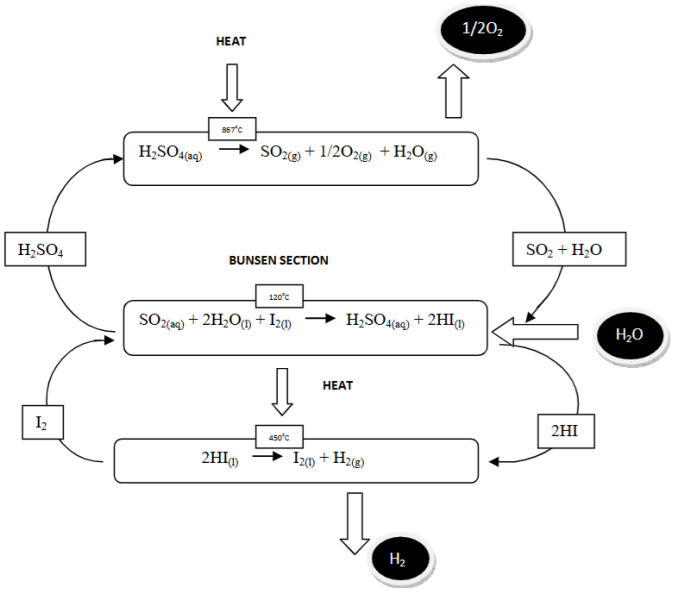

Figure 5. Schematic diagram for a three-step S-I thermochemical cycle [39].

2.3. Photonic process

Hydrogen can also be produced using a photonic process in which photon energy is used. This can be classified into two processes: photocatalytic and photoelectrochemical (also known as photoelectrolysis) water splitting.

2.3.1. Photocatalytic water splitting

The photocatalytic process uses direct sunlight in the presence of a photocatalyst, such as titanium oxide (TiO_2), which is used in powdered form and dispersed in water. Light will be radiated in this water, and the water will split into hydrogen and oxygen. This is a very flexible and cheap method of hydrogen production. The benefit of photocatalysts is that water splitting can occur in the homogeneous phase without the need for transparent electrodes or direct illumination. However, there are some disadvantages and challenges of employing this method in large-scale production.

In a photocatalytic cell, a semiconductor such as platinum (Pt) or Titanium oxide (TiO_2) can be considered a photoelectrochemical cell, which provides both oxidation and reduction at its surface. It happens in a series of steps. **Figure 6** shows the schematic representation of photocatalytic overall water splitting on a metal-loaded semiconductor (such as Pt/TiO_2) particle system [40].

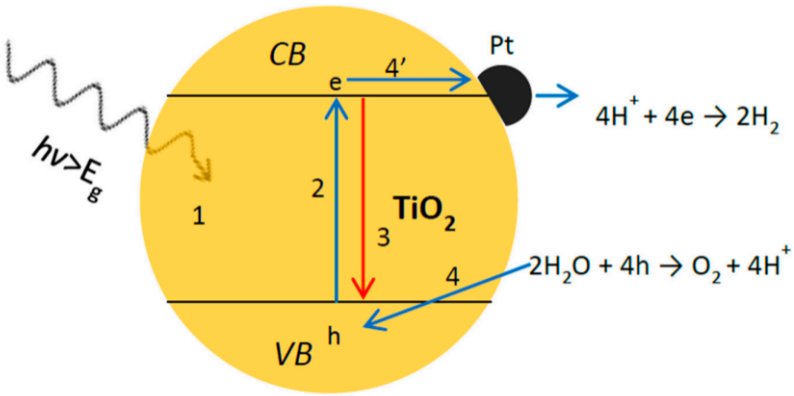

Figure 6. Process of the photocatalytic system [40].

2.3.2. Photoelectrochemical

The basic principle behind photoelectrochemical water decomposition, shown in **Figure 7**, is that light energy is converted into electricity in a cell made up of two electrodes submerged in an aqueous electrolyte, one of which must be made of a semiconductor to absorb light. Water is then electrolyzed using this power. Numerous photoelectrode materials, including WO_3, Fe_2O_3, and TiO_2, have been researched for usage as thin films in the photoelectrochemical process, and TiO_2 is found to be the most promising photoelectrode for this reaction [41].

2.4. Biomass process

Biomass can undergo two distinct processes: biological and thermochemical processes. The primary biological processes encompass bio-photolysis and fermentation, with bio-photolysis further categorized into direct and indirect bio-photolysis. Similarly, fermentation can be classified as dark fermentation and photo-fermentation.

Thermochemical conversion stands out as the leading technology for producing hydrogen from biomass, building on methodologies used in biofuels such as biomethane, which is derived from steam methane reforming (SMR). The three main thermochemical routes involved in this process are gasification, pyrolysis, and aqueous phase reforming [21].

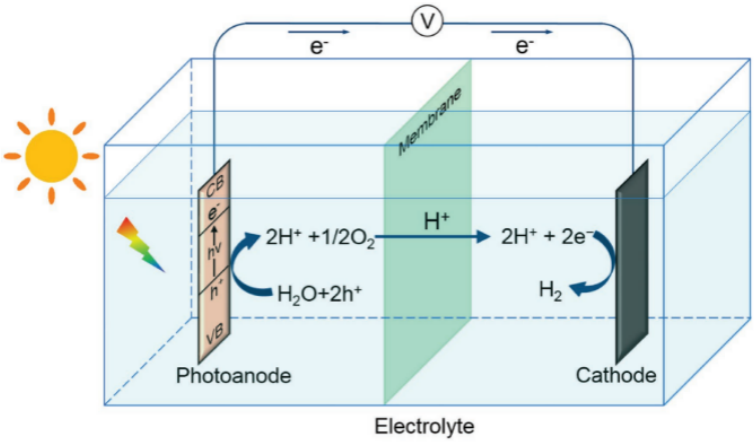

Figure 7. Process of photoelectrochemical cell (PEC) water splitting [42].

2.4.1. Biological process

Biophotolysis

There are two types of biophotolytic H_2 generation processes: Direct and indirect biophotolysis. Direct biophotolysis is a straightforward water-splitting mechanism that produces biohydrogen in either cyanobacteria or green algae. Various types of microalgae are used for biophotolysis, but the most used species is the microalgae Chlamydomonas reinhardtii (C. reinhardtii). Green algae in anoxic conditions can convert around 22% of the light energy by using hydrogen as an electron donor during carbon dioxide fixation, even at low light intensities. Green microalgae produce hydrogen in the dark under anaerobic conditions to support hydrogen metabolism.

Indirect biophotolysis was created to solve the issue of oxygen suppression of biohydrogen synthesis in direct biophotolysis. Cyanobacteria (green-blue algae) and Chlamydomonas reinhardtii are the most commonly used in this process. Production of biohydrogen and the separation of oxygen are the two steps in this process. Photosynthesis in an open pond converts atmospheric CO_2 into carbohydrates and oxygen, serving as the primary phase of the oxygen separation process, which comprises two stages. The subsequent stage involves inducing anaerobic, dark conditions in a closed bioreactor, where the generated carbohydrates are metabolized to yield acetic acid and biohydrogen [43].

Fermentation

Biomass rich in carbohydrates can be used as a renewable resource to assist photoheterotrophic (light fermentation) and anaerobic (dark fermentation) microorganisms in their production of biohydrogen. Dark fermentation is one of the most promising biological pathways for producing biohydrogen. It occurs under anaerobic conditions in the absence of light and uses the fermentative conversion of organic substrates and biomass to biohydrogen. Organic waste can also be used in this

process to form hydrogen. The pH, organic food, feed rate of nutrients, temperature, solids retention time, and partial pressure of hydrogen must all be controlled in the dark fermentation process in order to enhance the hydrogen yield [43].

In photofermentation or light fermentation, light energy is converted into biomass, and photosynthetic bacteria break down a variety of substrates to produce hydrogen. In this procedure, organic acids such as acetate, lactate, and butyrate are converted by purple nonsulfur (PNS) photosynthetic bacteria, such as Rhodobacter species, under anaerobic and anoxic conditions. Bacteria absorb solar energy, produce Adenosine triphosphate (ATP) through their photosynthetic mechanism, and use nitrogenase to turn organic acids into Hydrogen. The nitrogenase enzyme is responsible for producing hydrogen in this method as well. Because purple non-Sulphur bacteria can perform anoxygenic photosynthesis, in which no oxygen is evolved, there are no issues during photo fermentation despite nitrogenase being oxygen-sensitive. As a result, the nitrogenase activity is not inhibited, which is a significant advantage over the direct biophotolysis [22,44].

2.4.2. Thermochemical process for biomass

One of the most efficient ways to extract hydrogen-rich gases from biomass is using thermochemical processes. The key tenets used in these technologies include gasification, pyrolysis, and hydrothermal liquefaction.

Gasification is the thermochemical breakdown of biomass at high temperatures (800–900 ℃) in a limited-oxygen environment. Various product ratios, including H_2, CO, CO_2, CH_4, C_xH_x, and tars, are generated depending on operating parameters, such as temperature, catalysts, and the gasification medium. A catalyst used during gasification will accelerate the cracking reaction and lower the activation energy, thereby reducing energy consumption. Various types of catalysts are used, but the nickel-based catalyst showed better performance [45–50].

Pyrolysis resembles gasification but occurs at lower temperatures (400–800 °C) and is carried out without oxidizing agents. Therefore, the pyrolysis of biomass yields three distinct products: a liquid called bio-oil, a solid called bio-char, and a gaseous product called syngas. The relative proportions of these products are influenced by factors such as the composition of the feedstock and the pyrolysis process parameters. Pyrolysis can be categorized into two main types: rapid (fast) pyrolysis and traditional pyrolysis, depending on the specific operational conditions. Fast pyrolysis, which involves high temperatures and short residence times, is chosen for hydrogen production because charcoal is the main byproduct of conventional pyrolysis. Catalytic pyrolysis utilizes metal-based catalysts, such as Ni or alkali metals, or non-metal-based catalysts, such as activated carbon. Both have demonstrated their capability to enhance the production of hydrogen [48–50].

Hydrothermal liquefaction is a relatively low-temperature (300–400 °C), high-pressure (40–200 bar) process that produces bio-oil from a relatively wet biomass in the presence of a catalyst and hydrogen. A liquid biocrude, along with hydrogen and other byproducts, is the major outcome of this process [51].

2.5. Green hydrogen production method selection

Selecting an optimal green hydrogen production pathway in Oman and the broader Gulf Cooperation Council (GCC) region is a complex multi-criteria decision-making (MCDM) challenge. While the region boasts some of the highest levels of solar irradiation globally, abundant land resources, and a strong governmental commitment to hydrogen export and energy diversification, it also confronts significant constraints. These include acute water scarcity, harsh operational conditions, infrastructure readiness issues, and the need to compete on cost with fossil-fuel-based hydrogen [52–54]. The unique characteristics of specific regions highlight the need for a decision-support framework that effectively balances technical performance, resource availability, operational feasibility, economic viability, and environmental impact. Relying solely on single-criterion or purely economic optimization approaches is inadequate. Consequently, structured Multi-Criteria Decision-Making (MCDM) techniques have gained prominence in the assessment of hydrogen technology, particularly in arid and resource-constrained regions such as Oman and the Gulf Cooperation Council (GCC) [55–57].

In this study, we employ the Pugh matrix decision-making technique to evaluate and prioritize green hydrogen production technologies suitable for implementation in Oman and comparable GCC environments. The Pugh matrix functions as a comparative evaluation tool, facilitating the assessment of multiple alternatives against a common set of criteria relative to a defined baseline [57]. While advanced multi-criteria decision-making (MCDM) methods such as AHP, TOPSIS, PROMETHEE, and ELECTRE have been widely applied in studies of hydrogen and renewable energy [58–60], the Pugh matrix is particularly well-suited for the early-stage strategic technology selection required in the Omani and GCC hydrogen roadmap for several reasons: Compatibility with early-phase hydrogen planning: Oman's green hydrogen sector is currently in a scaling and infrastructure-development phase. At this stage, decision-makers necessitate a transparent and adaptable screening tool rather than a data-intensive optimization model. The Pugh matrix facilitates rapid comparison of multiple production routes under conditions of limited or evolving data [57, 61]. Equal-level evaluation of interdependent criteria: In the GCC context, criteria such as efficiency, water use, operating conditions, and cost are strongly interrelated. Hierarchical decomposition, as required by AHP, may oversimplify these interactions. The Pugh matrix permits all criteria to be evaluated at the same level, which aligns more closely with the integrated nature of hydrogen system challenges in arid regions [62]. Transparency for policy and industrial stakeholders: Hydrogen development in Oman involves multiple stakeholders, including policymakers, utilities, investors, and export-oriented industries. The intuitive scoring structure of the Pugh matrix enhances interpretability and facilitates stakeholder engagement and consensus-building [63]. Proven relevance in engineering and process selection: The Pugh matrix has been extensively applied in engineering design, process selection, and sustainability-driven technology screening, rendering it well-suited for the comparative assessment of hydrogen production technologies under region-specific constraints [57, 64].

2.6. Criteria definition and weighting with regional relevance

The Pugh matrix is implemented through a structured seven-step procedure that explicitly considers Oman/GCC conditions.

Step 1: Definition of Alternatives—The alternatives consist of technically viable hydrogen production pathways that can be integrated with Oman's renewable energy potential, particularly solar and wind resources, and aligned with export-oriented hydrogen strategies.

Step 2: Definition of Evaluation Criteria—Six criteria have been identified following a comprehensive review of hydrogen production technologies and the principal regional challenges impacting the deployment of green hydrogen in Oman and the GCC. These criteria are as follows: Energy efficiency, which underscores the necessity to optimize output from renewable electricity resources; Hydrogen yield, which affects land use, scalability, and export potential; Raw material availability, with a particular focus on access to water and feedstocks in arid environments; Required operating conditions, which consider high ambient temperatures, dust, and infrastructure constraints; Cost, which continues to be a significant barrier to the competitiveness of green hydrogen in the region; and Emissions, which are aligned with Oman's decarbonization and net-zero objectives. These criteria collectively address the technical, environmental, and socio-economic realities of hydrogen production in arid, high-temperature regions [53,55,56,65].

Step 3: Criteria Prioritization—The criteria are ranked in descending order of importance based on their relevance to overcoming the dominant barriers to green hydrogen competitiveness in Oman. Efficiency and hydrogen yield are prioritized due to the capital-intensive nature of renewable-based hydrogen systems, followed by raw material availability and operating conditions, which are critical in water-scarce and high-temperature environments. Cost and emissions, while still essential, are ranked lower due to ongoing policy support and long-term decarbonization commitments.

Step 4: Assignment of Relative Weightages—Linear weightages from 6 (highest priority) to 1 (lowest priority) are assigned to the criteria. This weighting scheme reflects strategic priorities specific to Oman's hydrogen ambitions while maintaining simplicity and methodological transparency [61].

Step 5: Baseline Selection—A conventional hydrogen production pathway or a reference green hydrogen method is selected as the baseline and assigned a neutral score of zero, enabling relative comparison across alternatives.

Step 6: Evaluation Scale Definition—A discrete qualitative-to-quantitative evaluation scale is adopted (**Table 1**), ranging from *Excellent* (+3) to *Not acceptable* (−2). This scale allows expert judgment to be systematically translated into numerical values while accommodating uncertainty typical of emerging hydrogen technologies.

Step 7: Score Aggregation and Ranking—Weighted scores are calculated by multiplying criterion weightages with the corresponding evaluation scale values. The aggregated scores are then used to rank hydrogen production pathways according to their suitability for deployment in Oman and the GCC.

Table 1. Evaluation scale points.

Description	Scale
Excellent	+3
Very good	+2
Good	+1
Acceptable/OK	0
Poor	−1
Not acceptable	−2

2.7. Sensitivity analysis in the regional context

A sensitivity analysis is conducted to assess the robustness of the technology rankings under uncertainty in criterion importance. Criterion weightages are varied by ±10–20% to reflect alternative policy priorities, such as increased emphasis on water availability or cost reduction. This analysis is particularly relevant in the Oman/GCC context, where hydrogen strategies are evolving in response to infrastructure development, desalination integration, and export market dynamics [63,66]. The results confirm whether the preferred production pathway remains dominant across plausible regional scenarios.

3. Results and discussion

The Pugh matrix methodology was applied to evaluate fifteen green hydrogen production pathways using six criteria relevant to the Oman/GCC context: efficiency, hydrogen yield, raw material availability, required operating conditions, cost, and greenhouse gas (GHG) emissions. The results provide a structured comparison of the relative suitability of each technology for deployment under arid-climate and resource-constrained conditions.

3.1. Criterion-level performance analysis

From an efficiency perspective, proton exchange membrane (PEM) electrolysis, solid oxide electrolysis (SOEC), and hydrogen liquefaction achieved the highest weighted scores. These technologies benefit from advanced electrochemical and thermodynamic characteristics that allow high conversion efficiencies [53, 55]. However, high efficiency alone does not guarantee regional suitability, particularly in Oman, where water scarcity, operational robustness, and capital cost remain dominant constraints [67]. In terms of hydrogen yield, alkaline electrolysis emerged as the leading technology. This outcome reflects its proven capability for continuous large-scale hydrogen production and its compatibility with industrial-scale deployment, both of which are essential for export-oriented hydrogen strategies envisioned in Oman and the GCC [68, 69]. Raw material availability is a critical factor in arid regions. Alkaline electrolysis, fermentation-based routes, gasification, pyrolysis, and liquefaction achieved the highest scores in this category due to their reliance on widely available materials or mature supply chains. In contrast, PEM electrolysis and photoelectrochemical routes scored lower because of their reliance on scarce noble metals and specialized membranes, which increase supply-chain vulnerability and

costs [70,71].

Regarding operating conditions, alkaline electrolysis and PEM electrolysis performed strongly due to their moderate temperature and pressure requirements. These characteristics enhance reliability and safety under Oman's high ambient temperatures and dust-prone environments, compared to high-temperature thermochemical cycles that require complex thermal management systems [72]. Cost analysis indicated that photolysis, fermentation, gasification, pyrolysis, and liquefaction achieved relatively favourable scores. However, many of these technologies remain at laboratory or pilot scales and face significant challenges related to efficiency, scalability, and system integration, limiting their short-term applicability in the GCC [73, 74]. For GHG emissions, electrolysis-based routes powered by renewable electricity achieved the highest scores, confirming their potential for near-zero operational emissions. In contrast, biomass and thermochemical conversion pathways exhibited comparatively higher emissions due to upstream processing and auxiliary energy requirements [53,75].

Although the present analysis adopts a structured qualitative–quantitative MCDM approach, the ranking outcomes are broadly consistent with reported quantitative performance indicators in the literature. Typical specific electricity consumption for alkaline and PEM electrolysis ranges between 48–55 kWh kg^{-1} H_2, corresponding to system efficiencies of 65–75%, while solid oxide electrolysis may exceed 80% under high-temperature operation but with significantly higher system complexity. When embedded in power-to-gas-to-power chains, overall round-trip efficiencies decline to approximately 35–40%, highlighting the importance of coupling hydrogen primarily to long-duration storage, industrial feedstocks, and ammonia or synthetic fuel production rather than short-term grid balancing [76, 77]. Incorporating such thermodynamic and techno-economic performance indicators into future extensions of the present framework would further strengthen the robustness of technology selection for large-scale deployment in Oman.

3.2. Overall ranking and technology prioritization

The aggregated weighted scores (**Table 2**) reveal that alkaline electrolysis achieved the highest overall score: 55, followed by PEM electrolysis: 50, and solid oxide electrolysis: 39. A significant performance gap exists between these leading technologies and the remaining alternatives, indicating a clear preference for electrolysis-based hydrogen production in the Oman/GCC context. This result highlights the importance of balanced performance across multiple criteria rather than optimization of a single parameter. Technologies that scored highly in efficiency but poorly in cost or material availability were outperformed by mature electrolysis systems that offer robustness and scalability.

Table 2. Production processes and the results of the Pugh matrix.

Criteria	Weight	Baseline	Electrolysis				Thermochemical water split			Photonic			Biological processes			Thermochemical processes		
			Alkaline	PEM	Solid oxide	Ther-molysis	Two steps (Mox)	Three steps (S-I)	Photo-catalytic water split	PEC	Direct photo-lysis	Indirect photo-lysis	Dark ferment-ation	Photo ferment-ation	Gasifi-cation	Pyrolysis	Liquification
Efficiency	6	0	6 × 2 = 12	6 × 3 = 18	6 × 3 = 18	6 × (−1) = −6	6 × 0 = 0	6 × 1 = 6	6 × (−2) = −12	6 × (−2) = −12	6 × 2 = 12	6 × (−2) = −12	6 × 1 = 6	6 × (−2) = −12	6 × 1 = 6	6 × 0 = 0	6 × 3 = 18

Table 2. *Cont.*

Criteria	Weight	Baseline	Electrolysis			Thermochemical water split			Photonic		Biological processes			Thermochemical processes		
			Alkaline	PEM	Solid oxide	Thermolysis	Two steps (Mox)	Three steps (S-I)	Photocatalytic water split	PEC	Direct photolysis	Indirect photolysis	Dark fermentation	Photo fermentation	Gasification	Pyrolysis	Liquification
Yield	5	0	5 × 3 = 15	5 × 2 = 10	5 × 1 = 5	5 ×(−1) = −5	5 × 0 = 0	5 × 1 = 5	5 × (−2) = −10	5 ×(−1) = −5	5 × (−2) = −10	5 × (−2) = −10	5 × 1 = 5	5 × 1 = 5	5 × 1 = 5	5 × (−1) = −5	5 × (−2) = −10
Raw Material Availability	4	0	4 × 3 = 12	4 × 2 = 8	4 × 2 = 8	4 × 1 = 4	4 × 1 = 4	4 × 1 = 4	4 × 2 = 8	4 × 2 = 8	4 × 1 = 4	4 × 1 = 4	4 × 3 = 12	4 × 3 = 12	4 × 3 = 12	4 × 3 = 12	4 × 3 = 12
Required Condition	3	0	3 × 3 = 9	3 × 3 = 9	3 × 1 = 3	3 × (−1) = −3	3 × 0 = 0	3 × 1 = 3	3 × 1 = 3	3 × 1 = 3	3 × 3 = 9	3 × 3 = 9	3 × 3 = 9	3 × 3 = 9	3 × 0 = 0	3 × 1 = 3	3 × 1 = 3
Cost	2	0	2 × 2 = 4	2 × 1 = 2	2 × 1 = 2	2 × (−1) = −2	2 × 1 = 2	2 × 1 = 2	2 × (−2) = −4	2 × (−2) = −4	2 × 3 = 6	2 × 3 = 6	2 × 3 = 6	2 × 3 = 6	2 × 3 = 6	2 × 3 = 6	2 × 3 = 6
Emission	1	0	1 × 3 = 3	1 × 3 = 3	1 × 3 = 3	1 × 3 = 3	1 × 3 = 3	1 × 3 = 3	1 × 3 = 3	1 × 3 = 3	1 × 3 = 3	1 × 3 = 3	1 × (−1) = −1	1 × (−1) = −1	1 × (−1) = −1	1 × (−1) = −1	1 × (−1) = −1
Total			**55**	**50**	**39**	**−9**	**9**	**23**	**−12**	**−7**	**24**	**0**	**37**	**19**	**28**	**15**	**28**

The evaluation scale used in the Pugh matrix is as follows:

Evaluation Scale	Value
Excellent	3
Very Good	2
Good	1
Acceptable	0
Poor	−1
Very Poor	−2

3.3. Comparative discussion: Alkaline vs. PEM electrolysis

Alkaline electrolysis ranked first due to its technological maturity, cost-effectiveness, and operational simplicity. Operating at moderate temperatures (50–80 °C) and pressures (up to 30 bar), it is well suited for large-scale deployment in Oman. The use of low-cost electrolytes such as potassium hydroxide (KOH) or sodium hydroxide (NaOH), along with non-noble metal catalysts, significantly enhances economic viability and material availability [68, 78].

PEM electrolysis ranked second, benefiting from higher efficiency (up to 90%), compact system design, and high hydrogen purity (up to 99.9%). These features make PEM particularly attractive for integration with variable renewable energy sources such as solar and wind [79]. However, its reliance on platinum-group metals and polymer membranes increases capital cost and supply-chain risk, which currently limits its competitiveness for large-scale deployment in Oman [70, 80]. While PEM technology is expected to improve as material costs decline and recycling pathways mature, alkaline electrolysis remains the most practical near-term solution for Oman due to its established industrial base and lower economic risk.

3.4. Implications for Oman and the GCC

The findings suggest that alkaline electrolysis currently represents the most appropriate technology for green hydrogen production in Oman, considering regional limitations related to water availability, cost sensitivity, climatic conditions, and infrastructure readiness. Proton exchange membrane (PEM) electrolysis serves as a robust complementary option, particularly for prospective decentralized or flexible operational scenarios. Other production methods, such as thermochemical cycles, photolysis, and biological processes, hold promise for long-term diversification but necessitate significant technological advancement before they can be adopted on a large

scale in the Gulf Cooperation Council (GCC) region.

4. Conclusion

Hydrogen is anticipated to assume a pivotal role in future low-carbon energy systems, particularly in the decarbonization of sectors that are challenging to abate and in facilitating the export of renewable energy. Nevertheless, the sustainability and competitiveness of hydrogen are critically contingent upon the selection of suitable production technologies. This study assessed fifteen green hydrogen production methods utilizing a structured Pugh matrix decision-making framework specifically adapted to the Oman/GCC context. Six efficiency criteria which are: hydrogen yield, raw material availability, required operating conditions, cost, and greenhouse gas emissions, were employed to encapsulate the technical, economic, and environmental dimensions pertinent to arid regions.

The findings suggest that alkaline electrolysis and PEM electrolysis are the most viable methods for green hydrogen production, with total scores of 55 and 50, respectively. Alkaline electrolysis outperforms PEM in terms of yield, material availability, cost, and technological maturity, whereas PEM exhibits superior efficiency and hydrogen purity. Given Oman's existing infrastructure, climate, and cost constraints, alkaline electrolysis is identified as the most suitable short-term solution for large-scale green hydrogen implementation. Therefore, it is recommended that alkaline electrolysis be prioritized for near- and medium-term hydrogen initiatives in Oman and the GCC. Meanwhile, PEM electrolysis should be supported through targeted research, development, and pilot projects, particularly for integration with variable renewable energy sources. Additionally, emerging technologies such as photolysis, thermochemical cycles, and biological routes should continue to be explored as part of a long-term hydrogen diversification strategy.

While the Pugh matrix offers a transparent and practical framework for decision support, it is important to acknowledge several limitations. The method's reliance on expert judgment may introduce subjectivity, influenced by regional experience and data availability. Additionally, the linear weighting approach does not explicitly account for nonlinear trade-offs between water consumption, energy efficiency, and cost, which are critical considerations in arid regions such as Oman. Furthermore, the Pugh matrix generates relative rankings rather than absolute performance metrics. Despite these limitations, when combined with sensitivity analysis and region-specific criteria definition, the method provides a robust and defensible approach for early-stage screening of green hydrogen technology in Oman and the GCC. Future research should incorporate quantitative techno-economic analysis and water–energy nexus modeling to complement the qualitative MCDM approach. The proposed methodology offers a transparent and robust framework for the early-stage selection of hydrogen technologies and can be readily adapted to other arid, resource-constrained regions pursuing green hydrogen development.

Author contributions: Each author played a significant role at various stages of the research process, culminating in the final report as detailed below. A: Responsible

for conceptualizing the research topic, developing the methodology, conducting data collection and analysis, and drafting the research report. AHS: Provided guidance and supervision throughout the research, ensured the validation of results and analyses, and contributed to the editing of the report. FMG: Oversaw the research methodology, conducted a thorough revision of the research report, prepared the manuscript for publication, and validated the data and findings. AM: Focused on validating the analysis and results, editing and refining the manuscript, and formatting it according to journal submission standards. AN: Assisted with data collection and analysis, while also contributing to the editing of the research report. All authors have read and agreed to the published version of the manuscript.

Funding: This work received no external funding.

Institutional review board statement: Not applicable.

Informed consent statement: Not applicable.

Data availability statement: Not applicable.

Acknowledgment: The authors express their gratitude to the Civil and Mechanical Engineering Programme at Middle East College for facilitating and providing all the essential support throughout the completion of this project work.

Conflict of interest: The authors declare no conflict of interest.

References

1. Guangul FM, Chala GT. SWOT analysis of wind energy as a promising conventional fuels substitute. In: Proceedings of the 2019 4th MEC International Conference on Big Data and Smart City (ICBDSC); 2019; Muscat, Oman. pp. 1–6.
2. Citaristi I. International energy agency—IEA. In: The Europa Directory of International Organizations 2022. Routledge; 2022. pp. 701–702.
3. International Energy Agency (IEA). Net Zero by 2050: A Roadmap for the Global Energy Sector. International Energy Agency; 2021.
4. Dincer I. Green methods for hydrogen production. International Journal of Hydrogen Energy. 2012; 37(2): 1954–1971.
5. Dincer I, Joshi AS. Solar Based Hydrogen Production Systems. Springer; 2013. Volume 553.
6. Khaleel M, Bashir S, Al-Ansari T, et al. Towards hydrogen sector investments for achieving sustainable electricity generation. Journal of Solar Energy and Sustainable Development. 2024; 13(1): 71–96.
7. Al-Breiki M, Bicer Y. Sustainable Energy Carriers for Energy Storage and Transport: Exploring Advanced Solutions for a Green Future. Springer Nature; 2025.
8. Landler A. Capacity Expansion Modeling of Hydrogen and Electricity with Sector Coupling in New England [PhD Thesis]. Massachusetts Institute of Technology; 2023.
9. Ratz H, West K, Liebman J, et al. The Role of Long-Duration Energy Storage in Deep Decarbonization: Policy Considerations. World Resources Institute; 2025.
10. Beck HP, Kuehne M, Sauer DU, et al. A comprehensive review of sustainable energy systems in the context of the German energy transition—part 2: Renewable energy and storage technologies. Carbon Neutral Systems. 2025; 1(1): 13.
11. Salmon N, Bañares-Alcántara R. Green ammonia as a spatial energy vector: A review. Sustainable Energy & Fuels. 2021; 5(11): 2814–2839.
12. Negro V, Noussan M, Chiaramonti D. The potential role of ammonia for hydrogen storage and transport: A critical review of challenges and opportunities. Energies. 2023; 16(17): 6192.

13. Ivanov P, Zhuk A. Thermodynamic modeling of the Power-to-Gas technology with methane and hydrogen as a chemical storage. Energy Storage and Conversion. 2025; 3(3).
14. Guangul FM, Chala GT. A comparative study between the seven types of fuel cells. Applied Science and Engineering Progress. 2020; 13(3): 185–194.
15. Wang X, Zhang Y, Liu Z, et al. Roadmap toward the production, storage, transportation, and applications of green hydrogen. Carbon and Hydrogen. 2025; 27(3): 241–267.
16. Kishk A. State-of-the-Art and Technologies in Hydrogen Production and Distribution. 2023. Available online: https://aaltodoc.aalto.fi/server/api/core/bitstreams/0aa2da49-8296-4872-9572-d4f46f30e521/content (accessed on 7 August 2025).
17. Algburi S, Faeq A, Ahmed A, et al. The green hydrogen role in the global energy transformations. Renewable and Sustainable Energy Transition. 2025; 8: 100118.
18. Kurre SK, Singh R, Kumar A, et al. Sustainable Hydrogen Technology and Global Energy Transition. Ashok Yakkaldevi; 2025.
19. Bockris JO. The origin of ideas on a hydrogen economy and its solution to the decay of the environment. International Journal of Hydrogen Energy. 2002; 27(7–8): 731–740.
20. Marbán G, Valdés-Solís T. Towards the hydrogen economy? International Journal of Hydrogen Energy. 2007; 32(12): 1625–1637.
21. Lepage T, Itouchène M, Courson C, et al. Biomass-to-hydrogen: A review of main routes production, processes evaluation and techno-economical assessment. Biomass and Bioenergy. 2021; 144: 105920.
22. Agyekum EB, Nutakor C, Agwa AM, et al. A critical review of renewable hydrogen production methods: Factors affecting their scale-up and its role in future energy generation. Membranes. 2022; 12(2): 173.
23. Yilanci A, Dincer I, Ozturk HK. A review on solar-hydrogen/fuel cell hybrid energy systems for stationary applications. Progress in Energy and Combustion Science. 2009; 35(3): 231–244.
24. Ni M, Leung MK, Leung DY. Energy and exergy analysis of hydrogen production by a proton exchange membrane (PEM) electrolyzer plant. Energy Conversion and Management. 2008; 49(10): 2748–2756.
25. Safari F. Development and Analysis of Alternative Thermochemical Cycles for Hydrogen Production [PhD Thesis]. Ontario Tech University; 2021.
26. Barghash H, Al-Suleimani A, Al-Habsi S, et al. Achieving decarbonization considering green hydrogen production: Case study of Oman. Results in Engineering. 2024; 23: 102657.
27. Sial NR, Al-Abri M, Al-Hinai A, et al. Techno-economic assessment of green hydrogen production in unexploited landlocked northern-western region of Oman to realize national sustainable strategy. International Journal of Hydrogen Energy. 2024. 137: 892–904.
28. Younus HA, Al Hajri R, Ahmad N, et al. Green hydrogen production and deployment: opportunities and challenges. Discover Electrochemistry. 2025; 2(1): 32.
29. Dincer I, Acar C. Review and evaluation of hydrogen production methods for better sustainability. International Journal of Hydrogen Energy. 2015; 40(34): 11094–11111.
30. Chisholm G, Zhao T, Cronin L. Hydrogen from water electrolysis. In: Storing Energy. Elsevier; 2022. pp. 559–591.
31. Elder R, Cumming D, Mogensen MB. High temperature electrolysis. In: Carbon Dioxide Utilisation. Elsevier; 2015. pp. 183–209.
32. Ni M, Leung MK, Leung DY. Technological development of hydrogen production by solid oxide electrolyzer cell (SOEC). International Journal of Hydrogen Energy. 2008; 33(9): 2337–2354.
33. Rodríguez J, Amores E. CFD modeling and experimental validation of an alkaline water electrolysis cell for hydrogen production. Processes. 2020; 8(12): 1634.
34. Raman R, Kumar S, Gupta A, et al. Energy-efficient parameter estimation of solid oxide fuel cells under varying pressure conditions using the Black Widow optimization algorithm. Frontiers in Energy Research. 2025; 13: 1659232.
35. Sundén B. Hydrogen, Batteries and Fuel Cells. Academic Press; 2019.
36. Rozzi E, Minuto FD, Lanzini A, et al. Green synthetic fuels: Renewable routes for the conversion of non-fossil feedstocks into gaseous fuels and their end uses. Energies. 2020; 13(2): 420.
37. Safari F, Dincer I. A review and comparative evaluation of thermochemical water splitting cycles for hydrogen production. Energy Conversion and Management. 2020; 205: 112182.
38. Roeb M, Neises M, Monnerie N, et al. Materials-related aspects of thermochemical water and carbon dioxide splitting: a review. Materials. 2012; 5(11): 2015–2054.

39. Nyoni B. Simulation of the Sulphur Iodine Thermochemical Cycle [PhD Thesis]. North-West University; 2011.
40. Nadeem MA, Khan MA, Idrees F, et al. An overview of the photocatalytic water splitting over suspended particles. Catalysts. 2021; 11(1): 60.
41. El-Shafie M, Kambara S, Hayakawa Y. Hydrogen production technologies overview. Journal of Power and Energy Engineering. 2019. 7: 107–154.
42. Xu XT, Pan L, Zhang X, et al. Rational design and construction of cocatalysts for semiconductor-based photo-electrochemical oxygen evolution: a comprehensive review. Advanced Science. 2019; 6(2): 1801505. doi: 10.1002/advs.201801505
43. Azwar M, Hussain M, Abdul-Wahab A. Development of biohydrogen production by photobiological, fermentation and electrochemical processes: A review. Renewable and Sustainable Energy Reviews. 2014; 31: 158–173.
44. Chandrasekhar K, Lee YJ, Lee DW. Biohydrogen production: Strategies to improve process efficiency through microbial routes. International Journal of Molecular Sciences. 2015; 16(4): 8266–8293.
45. Guangul F, Sulaiman S, Ramli A. Gasification of Oil Palm Fronds with Preheated Inlet Air. Universiti Teknologi PETRONAS; 2013.
46. Guangul FM, Sulaiman SA, Raghavan VR. Gasification and effect of gasifying temperature on syngas quality and tar generation: A short review. AIP Conference Proceedings. 2012; 1440: 491–498. doi: 10.1063/1.4704254
47. Guangul F, Sulaiman S, Ramli A. Temperature profile and producer gas composition of high temperature air gasification of oil palm fronds. IOP Conference Series: Earth and Environmental Science. 2013; 16, 012067.
48. Megía PJ, Vizcaíno AJ, Calles JA, et al. Hydrogen production technologies: From fossil fuels toward renewable sources. A mini review. Energy & Fuels. 2021; 35(20): 16403–16415.
49. Guangul FM, Sulaiman SA, Ramli A. Study of the effects of operating factors on the resulting producer gas of oil palm fronds gasification with a single throat downdraft gasifier. Renewable Energy. 2014; 72: 271–283.
50. Guangul FM, Sulaiman SA, Ramli A. Gasifier selection, design and gasification of oil palm fronds with preheated and unheated gasifying air. Bioresource Technology. 2012; 126: 224–232.
51. Chen WT, Zhang Y, Zhang J, et al. Renewable diesel blendstocks produced by hydrothermal liquefaction of wet biowaste. Nature Sustainability. 2018; 1(11): 702–710.
52. Pohekar SD, Ramachandran M. Application of multi-criteria decision making to sustainable energy planning—A review. Renewable and Sustainable Energy Reviews. 2004; 8(4): 365–381.
53. Staffell I, Scamman D, Velazquez Abad A, et al. The role of hydrogen and fuel cells in the global energy system. Energy & Environmental Science. 2019; 12(2): 463–491.
54. Wang JJ, Jing YY, Zhang CF, et al. Review on multi-criteria decision analysis aid in sustainable energy decision-making. Renewable and Sustainable Energy Reviews. 2009; 13(9): 2263–2278.
55. Ball M, Weeda M. The hydrogen economy–vision or reality? International Journal of Hydrogen Energy. 2015; 40(25): 7903–7919.
56. Maroufmashat A, Fowler M. Transition of future energy system infrastructure; through power-to-gas pathways. Energies. 2017; 10(8): 1089.
57. Pugh S. Total Design: Integrated Methods for Successful Product Engineering. Addison-Wesley; 1991.
58. Brans JP, Vincke P. Note—A Preference Ranking Organisation Method: (The PROMETHEE Method for Multiple Criteria Decision-Making). Management Science. 1985; 31(6): 647–656.
59. Huynh VN, Yanako Y, Nakamori Y, et al. Multiple-attribute decision making under uncertainty: The evidential reasoning approach revisited. IEEE Transactions on Systems, Man, and Cybernetics-Part A: Systems and Humans. 2006; 36(4): 804–822.
60. Saaty TL. Decision making with the analytic hierarchy process. International Journal of Services Sciences. 2008; 1(1): 83–98.
61. Otto KN. Product Design: Techniques in Reverse Engineering and New Product Development. Tsinghua University Press; 2003.
62. Dodgson JS, Spackman M, Pearman A, et al. Multi-criteria Analysis: A Manual. Department for Communities and Local Government; 2009.
63. Ishizaka A, Nemery P. Multi-criteria Decision Analysis: Methods and Software. John Wiley & Sons; 2013.
64. Fargier H, Thierry C. The use of possibilistic decision theory in manufacturing planning and control: Recent results in Fuzzy Master Production Scheduling. In: Title of the Book. Springer-Verlag; 2000. pp. 45–59.
65. Benbouzid M, Machmoum M, Feldhoff AF, et al. Global Journey of Green Hydrogen: Opportunities and Challenges. In: Green Hydrogen. Wiley; 2025. pp. 337–371.

66. Isa AHM, Mohd RM. A Hybrid AHP-TOPIS-Based Marine Economic Activities Evaluation Model for Marine Geospatial Data Infrastructure. UNILAG Journal of Transport and Logistics. 2024; 1(1): 55–72.
67. International Energy Agency. Global Hydrogen Review 2023. OECD Publishing; 2023.
68. Buttler A, Spliethoff H. Current status of water electrolysis for energy storage, grid balancing and sector coupling via power-to-gas and power-to-liquids: A review. Renewable and Sustainable Energy Reviews. 2018; 82: 2440–2454.
69. Kumar SS, Himabindu V. Hydrogen production by PEM water electrolysis–A review. Materials Science for Energy Technologies. 2019; 2(3): 442–454.
70. Glenk G, Reichelstein S. Economics of converting renewable power to hydrogen. Nature Energy. 2019; 4(3): 216–222.
71. Züttel A, Remhof A, Borgschulte A, et al. Hydrogen: the future energy carrier. Philosophical Transactions of the Royal Society A: Mathematical, Physical and Engineering Sciences. 2010; 368(1923): 3329–3342.
72. Laguna-Bercero MA. Recent advances in high temperature electrolysis using solid oxide fuel cells: A review. Journal of Power Sources. 2012; 203: 4–16.
73. Turner J, Sreivatsava G, Oglesby W, et al. Renewable hydrogen production. International Journal of Energy Research. 2008; 32(5): 379–407.
74. Abanades S, Flamant G. Thermochemical hydrogen production from a two-step solar-driven water-splitting cycle based on cerium oxides. Solar Energy. 2006; 80(12): 1611–1623.
75. Acar C, Dincer I. Comparative assessment of hydrogen production methods from renewable and non-renewable sources. International Journal of Hydrogen Energy. 2014; 39(1): 1–12.
76. Xhani E. Performance Analysis of a Hydrogen Production Plant: Efficiency Evaluation of a NaOH Alkaline Electrolyzer [Master's Thesis]. Università Politecnica delle Marche; 2023.
77. Begum S. Techno-Economic Analysis of Hydrogen Production & Storage Technologies for Grid Scale Applications [Master's Thesis]. University of Vaasa; 2024.
78. Zeng K, Zhang D. Recent progress in alkaline water electrolysis for hydrogen production and applications. Progress in Energy and Combustion Science. 2010; 36(3): 307–326.
79. Carmo M, Fritz DL, Mergel J, et al. A comprehensive review on PEM water electrolysis. International Journal of Hydrogen Energy. 2013; 38(12): 4901–4934.
80. Ursua A, Gandia LM, Sanchis P. Hydrogen production from water electrolysis: Current status and future trends. Proceedings of the IEEE. 2011; 100(2): 410–426.

Energy Storage and Conversion 2025, 3(4), 3933.
doi: https://doi.org/10.59400/esc3933

Article

Hybrid energy storage system integrating lithium-ion batteries and supercapacitors for enhanced electric vehicle performance

Ashiq Hussain[1,*], Muhammad Fasih Aamir[1,2,*]

[1] Graduate School of Science and Technology, University of Tsukuba, 1-1-1 Tennodai, Tsukuba 305-8577, Japan

[2] International Center for Materials Nanoarchitectonics (MANA), National Institute for Materials Science (NIMS), 1-1 Namiki, Tsukuba 305-0044, Japan

*** Corresponding author:** Ashiq Hussain, s2420914@u.tsukuba.ac.jp; Muhammad Fasih Aamir, aamir.fasih.ke@u.tsukuba.ac.jp

CITATION

Hussain A, Aamir MF. Hybrid energy storage system integrating lithium-ion batteries and supercapacitors for enhanced electric vehicle performance. Energy Storage and Conversion. 2025; 3(4): 3933. https://doi.org/10.59400/esc3933

ARTICLE INFO

Received: 17 September 2025
Revised: 7 November 2025
Accepted: 14 November 2025
Available online: 8 December 2025

Abstract: The increasing adoption of electric vehicles (EVs) has highlighted persistent challenges related to battery efficiency, limited lifespan and performance fluctuations during highly dynamic driving conditions. To address such issues, this study proposes a novel Hybrid Energy Storage System (HESS) that strategically combines lithium-ion batteries and supercapacitors to take advantage of the high energy density of batteries and the rapid charge-discharge characteristics of supercapacitors. The hybrid configuration is governed by an Arduino-based control unit equipped with an intelligent power management algorithm, which tracks real-time acceleration profiles and dynamically allocates power to the appropriate energy source. During steady-state operation, the batteries supply the required power, while peak loads during sudden acceleration or regenerative braking are effectively handled by the supercapacitors. Extensive simulations and laboratory experiments demonstrate that this strategy significantly reduces battery stress, mitigates thermal effects, and increases overall cycle life. Additionally, a dedicated mobile application enables real-time monitoring of key operating parameters, including SOC, vehicle speed and overall system status, thereby improving user interaction and enabling proactive maintenance decisions. Overall, the proposed HESS substantially improves energy efficiency and operational stability, representing a practical and scalable solution for achieving long-term sustainability and high performance in next-generation electric vehicle technologies.

Keywords: hybrid energy storage system (HESS); electric vehicles (EVs); supercapacitors; energy management system (ESS); battery management; Arduino control

1. Introduction

1.1. Background

The rising number of internal combustion engine (ICE) vehicles, which depend heavily on non-renewable fossil fuels, has led to serious energy shortages and environmental degradation, including increased greenhouse gas emissions [1–3]. In response, many countries are accelerating the transition toward electric vehicles (EVs) as a cleaner and more sustainable alternative to reduce oil dependency and curb urban air pollution [4,5]. The first electric vehicle (EV) was developed in 1834 [6]. Throughout the 19th century, numerous companies, particularly in America, Britain, and France, endeavored to advance EV technologies [7]. However, these early vehicles relied on a

single battery source, which proved insufficient for practical use [8–11]. Additionally, technological limitations in battery design combined with the rapid progress of internal combustion engine (ICE) vehicles contributed to the decline of EV popularity by the 1930s [12–14]. In 1898, German engineer Dr. Ferdinand Porsche developed the first hybrid electric vehicle (HEV), known as the Lohner Electric Chaise [15]. HEV technology was designed to address the limitations of both ICE vehicles and pure EVs by combining an internal combustion engine with a battery-powered electric motor [16–18]. This hybrid configuration offers several advantages, including reduced emissions, improved reliability, enhanced fuel efficiency, and extended driving range compared to either ICE vehicles or EVs alone [19, 20]. Additionally, HEVs can recover kinetic energy during braking, similar to EVs, improving overall energy efficiency [20, 21]. However, the HEV powertrain is inherently more complex due to the integration of multiple components and sophisticated control systems [22–24].

The use of electric vehicles (EVs) gained early momentum through the efforts of the California Air Resources Board (CARB), which issued strong regulatory signals aimed at reducing vehicular emissions [25–27]. This initiative drew global attention, as EVs were seen as a promising solution to environmental pollution [28–30]. Consequently, countries around the world began accelerating their shift toward electric mobility in an effort to build cleaner and more sustainable transportation systems. Several factors influence the efficiency and performance of electric vehicles, with the energy storage system (ESS) being one of the most critical components [31]. The ESS plays a central role in determining the overall functionality and range of an EV. Among the various energy storage options, batteries remain the most widely used devices across all EV platforms [32]. While different battery chemistries have been explored, lithium-ion (Li-ion) batteries have emerged as the most promising due to their high energy density, lightweight design, and widespread use in portable electronic devices such as smartphones and laptops [33].

Despite their advantages, the broader adoption of EVs is still hindered by limitations such as the relatively low energy density and limited lifespan of Li-ion batteries [34]. Several factors such as overheating, internal redox reactions, and overcharging, can accelerate battery degradation. Although significant advancements have been made to mitigate these issues, battery performance still poses a barrier to the large-scale deployment of electric vehicles [35]. One of the primary factors that reduces the battery lifecycle in electric vehicles (EVs) is the sudden discharge of energy during peak power demands, such as rapid acceleration [36]. This scenario frequently occurs in EVs due to varying influences like driving habits and road conditions, which cause abrupt fluctuations in power consumption [37, 38]. While batteries perform optimally under steady, smooth power demand at constant speeds, such ideal conditions are rarely encountered in real-world driving. Therefore, to extend the lifespan of the energy storage system, an effective battery management system (BMS) is essential to regulate and ensure a smooth and consistent flow of power from the battery to the vehicle. One of the prominent solutions is to utilize the supercapacitor along with the battery to absorb the fluctuation in energy consumption by the battery during unprecedented events. Several studies investigated the impact of the integration of a supercapacitor along

with a battery on electric vehicle performance and durability. Research by Pedram et al. [39] demonstrated that hybrid systems significantly reduce battery current ripple under dynamic load conditions, leading to improved battery efficiency and thermal behavior. Similarly, Garcia et al. [40] highlighted that hybrid configurations enhance powertrain reliability by decoupling high-power transients from the main battery. Other works have focused on the optimization of power flow between storage devices, showing that proper coordination between batteries and supercapacitors can substantially extend battery cycle life and improve regenerative energy utilization [41,42].

More recent studies have explored advanced control frameworks for HESS in EVs. For example, fuzzy-logic-based and model predictive control approaches have been proposed to achieve smoother power sharing and improved energy efficiency [43, 44]. Optimization-based strategies using dynamic programming and real-time energy management have also been reported to enhance system-level performance under standardized driving cycles [45]. In addition, several authors have examined the role of supercapacitors in absorbing regenerative braking energy more effectively than batteries, thereby reducing energy losses and mechanical braking demand [46]. These studies collectively confirm that HESS offers clear technical advantages over single-source battery systems.

Despite these advancements, experimental validation remains limited in many reported works. A significant portion of the literature relies heavily on numerical simulations using predefined driving cycles, with minimal focus on hardware implementation or real-world operating conditions [41–44]. Moreover, while some studies have introduced sophisticated energy management algorithms, their practical deployment is often constrained by computational complexity, sensor dependency, and the need for accurate system modeling [47–50]. Recent research has also begun to emphasize the importance of real-time monitoring and connectivity; however, IoT-based integration in HESS is still at an early stage and is rarely coupled directly with control decisions [51–55].

Overall, although existing studies clearly demonstrate the benefits of hybrid battery–supercapacitor systems, several shortcomings remain when viewed from a practical implementation perspective. Most studies do not provide a simple and intuitive criterion for activating supercapacitor support during real driving conditions, often relying instead on complex SOC- or model-based thresholds. Charging strategies for supercapacitors are frequently limited to regenerative braking, reducing their availability during frequent acceleration events. Furthermore, many proposed HESS architectures depend on multiple DC–DC converters, increasing system cost and complexity and limiting applicability in low-cost EV platforms. Experimental prototype validation and user-level monitoring are also insufficiently addressed. In contrast, the present work directly tackles these limitations by introducing a throttle-variation-based activation mechanism, a low-complexity switching architecture, and integrated IoT-based real-time monitoring, thereby offering a practical and scalable solution aligned with real-world electric vehicle operation.

1.2. Purpose of this research

As discussed in the above section, most existing studies on HESS for electric vehicles primarily focus on improving energy efficiency, power smoothing, and battery performance through advanced control strategies and converter-based architectures. While these studies demonstrate the technical benefits of combining batteries and supercapacitors, many of them rely on complex energy management algorithms, such as optimization-based or predictive control methods, which limit their practical applicability in real-time and low-cost electric vehicle platforms. In addition, several studies assume that supercapacitors are charged exclusively through regenerative braking, which restricts their effectiveness under frequent acceleration or urban driving conditions.

Furthermore, existing research often lacks clear and practical criteria for determining when the supercapacitor should actively support the battery during vehicle operation. Although peak power mitigation is widely acknowledged, few studies explicitly define the activation threshold or duration of supercapacitor operation in a manner that is simple, intuitive, and implementable using low-complexity hardware. Most reported works emphasize simulation-based validation under standardized driving cycles, with limited focus on prototype-level implementation or real-world operation. Moreover, real-time monitoring and remote visualization of battery and supercapacitor health parameters are rarely integrated directly into the energy management framework, despite their importance for diagnostics, reliability, and user awareness.

To address these gaps, this study proposes an IoT-based hybrid battery–supercapacitor energy storage system for electric vehicles that emphasizes simplicity, practicality, and real-time applicability. The proposed system introduces a throttle-variation-based energy management strategy to explicitly identify peak power demand conditions and dynamically allocate power between the battery and supercapacitor. By reducing control complexity and integrating real-time monitoring, the proposed approach aims to enhance battery lifetime and improve overall system performance. The main contributions of this research are summarized as follows:

a. Development of a low-complexity hybrid battery–supercapacitor energy storage architecture for electric vehicles, in which the supercapacitor is employed as an auxiliary power source to mitigate peak power demands and reduce battery stress during rapid acceleration events.

b. Design and implementation of a throttle-difference-based energy management strategy that provides a clear, intuitive, and real-time criterion for activating supercapacitor support, eliminating the need for computationally intensive control algorithms.

c. Integration of an IoT-based monitoring framework that enables real-time observation and remote visualization of key vehicle and energy storage parameters, including state of charge and vehicle speed, thereby enhancing system transparency and operational reliability.

d. Validation of the proposed hybrid energy storage system through both simulation and prototype-level hardware implementation, demonstrating its practical feasibility and effectiveness in improving battery lifetime and operational

efficiency under dynamic driving conditions.

2. Methodology

This work presents the detailed methodology adopted for the design, implementation, and validation of the proposed IoT-based hybrid energy storage system for electric vehicles using a battery and supercapacitor. The methodology focuses on system architecture, operating principles, energy management strategy, control and switching logic, IoT-based monitoring, and simulation setup. The proposed approach aims to protect the battery from sudden peak power demands by intelligently coordinating power flow between the battery and the supercapacitor under different driving conditions.

2.1. System architecture

The suggested system architecture is a hybrid energy storage system in which a lithium-ion battery is the primary energy source and a supercapacitor bank serves as an auxiliary energy storage device to handle peak power needs, as shown in **Figure 1**. An Arduino microcontroller serves as the system's central control unit. The controller continuously monitors throttle input to determine the vehicle's operating mode. The controller uses relay-based switching to switch the energy source between the battery and the supercapacitor in response to throttle changes. This architecture enables the battery to run under more stable current circumstances, while the supercapacitor meets short-duration high-power demands during abrupt acceleration.

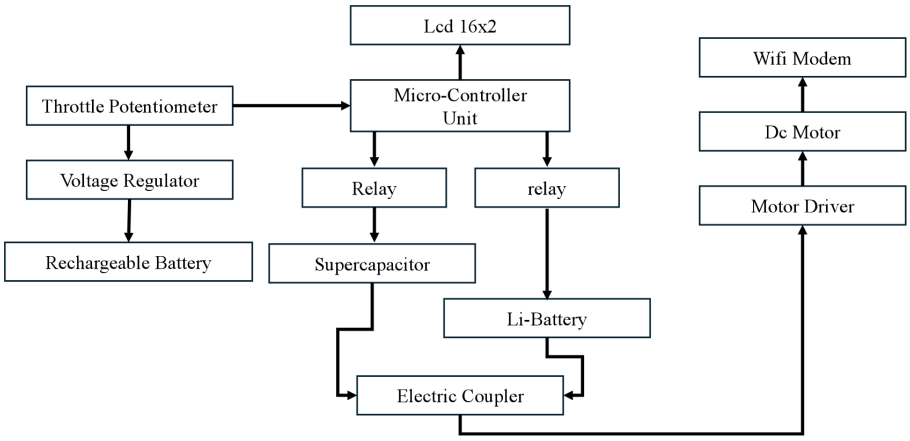

Figure 1. Schematic of System Architecture-hybrid energy storage system.

During normal driving conditions, the lithium-ion battery provides the electric car with sustained energy. The battery's high energy density makes it suited for long-term operation; yet, it is vulnerable to large current transients. In the proposed architecture, the battery provides power mostly during steady-state operation, avoiding exposure to sudden peak loads that could exacerbate aging and thermal stress.

To address quick power fluctuations, a supercapacitor bank has been included as an additional energy storage device. Supercapacitors have a high-power density and a quick charge-discharge rate, making them excellent for supplying energy during unexpected acceleration events. When peak power demand is recognized, the supercapacitor temporarily replaces the battery as the motor's primary power source, protecting it from

high current discharge and increasing its operational life.

The Arduino microcontroller serves as the system's central processor. It accepts input from the throttle potentiometer and other sensors, processes the control algorithm, and generates relay switching signals. The Arduino implements the energy management logic in real time, ensuring a smooth transition between battery and supercapacitor modes. Its low cost, simplicity, and ease of programming make it ideal for prototyping and low-cost electric vehicle applications.

The throttle potentiometer represents the electric vehicle's accelerator input. It generates an analog signal based on the driver's acceleration requirement. The controller continuously monitors the throttle position and calculates the variation between time periods. This variation is the essential indicator for detecting unexpected acceleration and activating supercapacitor support. The relay modules function as electrically regulated switches, connecting the battery or the supercapacitor to the motor drive circuit. The relays open or close in response to Arduino control signals, allowing the right energy source to be selected. Relay-based switching is preferred because of its simplicity, dependability, and adaptability for low-complexity system designs. The DC motor reflects the electric car prototype's traction load. It turns electrical energy into mechanical motion, and its power consumption changes with throttle input. Peak power requirements result from sudden increases in motor speed or torque demand, which are met by the hybrid energy storage system. The motor driver connects the energy storage system and the DC motor. It provides controlled power to the motor, protects the controller from excessive currents, and allows for smooth motor performance under variable load situations.

A voltage regulator provides a constant and regulated voltage to the Arduino, sensors, Wi-Fi module, and display modules. This component protects low-power devices from voltage fluctuations and maintains system stability. The system features a 16 × 2 LCD display for user engagement and monitoring. It allows for the local, real-time viewing of system data such as voltage, current, motor speed, and active energy source. This display simplifies debugging, testing, and on-site monitoring. The Wi-Fi module allows for remote system monitoring using IoT technology. It sends crucial operational data to a mobile app or online interface, such as battery and supercapacitor status, motor speed, and charge level. This feature improves system openness, enables remote diagnostics, and allows for future extensions like data logging and predictive maintenance.

Overall, the suggested system architecture allows for coordinated interaction between energy storage devices, control units, power electronics, and monitoring components. By dynamically dividing power between the battery and supercapacitor depending on throttle variation, the architecture significantly decreases battery stress during peak demand events while maintaining efficient and dependable electric vehicle performance.

2.2. Operating principle of the hybrid energy storage system

The operating principle of the proposed hybrid energy storage system is based on classifying vehicle operation into two distinct modes, namely normal demand mode

and peak demand mode, according to the variation in throttle input, named as throttle difference. The throttle difference is defined as the change in vehicle acceleration between two consecutive time steps. It represents the variation in throttle input demanded by the driver or control system. A low throttle difference indicates smooth driving with gradual power demand, whereas a high throttle difference corresponds to sudden acceleration or deceleration. These rapid changes generate transient power spikes that stress the battery. During normal driving conditions, when the throttle position changes gradually and the power demand remains relatively low, the lithium-ion battery supplies energy to the DC motor. This mode ensures efficient utilization of the battery for sustained energy delivery and avoids unnecessary stress on the battery during steady-state operation.

In the developed prototype, the throttle input is implemented using a potentiometer connected to the Arduino microcontroller. The potentiometer provides an analog signal proportional to the driver's acceleration demand. The microcontroller continuously reads this signal and compares the current throttle value with the previous value to determine the throttle variation. When the throttle variation remains below a predefined threshold, the system remains in battery mode. In this state, the battery relay remains closed while the supercapacitor relay remains open, allowing the battery to supply power to the motor through the motor driver.

During sudden acceleration or rapid changes in throttle position, the power demand of the DC motor increases sharply. Supplying this transient power directly from the battery can result in high current draw, increased internal losses, and thermal stress, which accelerate battery degradation. To prevent this, the proposed system activates the supercapacitor during peak demand conditions. In the prototype, when the throttle variation exceeds the predefined threshold, the Arduino generates control signals that disconnect the battery relay and simultaneously connect the supercapacitor relay. As a result, the supercapacitor becomes the primary energy source for the motor during this short-duration high-power event.

Due to its high-power density and fast charge–discharge characteristics, the supercapacitor is capable of supplying the required transient current almost instantaneously. During this period, the battery is effectively isolated from the peak load, thereby reducing high-current stress and protecting it from accelerated aging. The motor continues to operate smoothly because the switching process is fast and does not interrupt the power supply to the motor. Once the acceleration stabilizes and the throttle variation falls below the threshold value, the system automatically switches back to battery mode. The Arduino deactivates the supercapacitor relay and reconnects the battery relay, allowing the battery to resume supplying energy for normal vehicle operation. This continuous monitoring and rapid switching process ensures that the supercapacitor is used only when necessary, while the battery is reserved for energy-intensive but low-power-fluctuation operation.

In the prototype, the current operating mode—battery or supercapacitor—is displayed on the 16 × 2 LCD and transmitted to the remote monitoring interface via the Wi-Fi module. This allows real-time observation of system behavior and verification of correct switching during different driving conditions. Through this operating principle,

the proposed hybrid energy storage system effectively smooths battery current, enhances battery lifetime, and improves overall system performance under dynamic driving conditions.

2.3. Energy management strategy

The energy management strategy of the proposed system is based on throttle variation rather than complex state-of-charge or model-based control methods. The throttle input is measured using a potentiometer connected to the Arduino. The controller continuously compares the current throttle value with the previous value to compute the throttle difference.

A predefined threshold is used to distinguish between normal and peak demand conditions. When the throttle difference remains below the threshold, the system operates in battery mode. When the throttle difference exceeds the threshold, indicating sudden acceleration, the controller activates the supercapacitor. This rule-based strategy is simple, computationally efficient, and suitable for real-time implementation in low-cost electric vehicle platforms. By prioritizing the supercapacitor during high-power demand events, the strategy reduces battery current peaks and minimizes battery degradation. At the same time, the battery remains responsible for supplying energy during steady-state operation, ensuring optimal utilization of both energy storage devices.

2.4. Control algorithm and switching logic

The control algorithm is implemented using Arduino programming and operates in a continuous loop. The algorithm begins by reading sensor data, including throttle position, voltage, current, and motor speed. The throttle value is mapped and compared with a predefined threshold to determine the operating mode. If the throttle value exceeds the set threshold, the Arduino sends a control signal to deactivate the battery relay and activate the supercapacitor relay. In this mode, the supercapacitor supplies power to the motor. If the throttle value remains below the threshold, the battery relay remains active, and the supercapacitor is disconnected. The switching logic is designed to be fast and reliable, ensuring smooth transitions between battery and supercapacitor modes without interrupting motor operation. The controller periodically checks the throttle condition and updates the relay states accordingly. This logic ensures continuous protection of the battery from sudden high current demands.

2.5. IoT-based monitoring framework

An IoT-based monitoring framework is included in the proposed hybrid energy storage system, allowing for real-time observation and remote supervision of vehicle and storage parameters. A Wi-Fi module connected to the Arduino microcontroller establishes a wireless connection between the hardware system and a remote monitoring platform. The microprocessor continuously collects data from voltage, current, and speed sensing devices, as well as the functioning state of the energy storage system, and communicates it via the Wi-Fi module at regular intervals. Key metrics such as battery voltage, supercapacitor voltage, motor current, motor speed, and the active working mode (battery or supercapacitor) are sent to a mobile app or web dashboard. This enables

users to check the energy storage system's real-time status without requiring physical access to the vehicle. The device also gives instant visual feedback on switching events, allowing for verification of proper supercapacitor activation during peak power demand.

The IoT framework improves system transparency and dependability by allowing remote diagnostics and fault detection. Any problematic behavior, such as sudden voltage decreases or frequent switching events, can be detected in real time, allowing for prompt corrective action. Furthermore, continuous data logging enables performance analysis and long-term evaluation of battery and supercapacitor utilization trends. This architecture also lays the groundwork for future improvements, such as predictive maintenance, cloud-based data analytics, and adaptive energy management methods based on past driving behavior.

3. Simulation setup

3.1. Simulation environment and system modeling

The simulation of the proposed IoT-based hybrid energy storage system was carried out using Proteus 8 Professional software prior to hardware implementation. Proteus was selected because of its strong capability to simulate microcontroller-based systems and mixed analog–digital circuits, making it suitable for validating Arduino-controlled power electronics applications. The complete system schematic was designed in the Proteus environment to closely resemble the actual hardware prototype. All major system components were modeled, including the Arduino microcontroller, lithium-ion battery, supercapacitor bank, relay modules, DC motor, motor driver, voltage regulator, throttle potentiometer, and display units. Each component was connected according to the proposed system architecture to ensure accurate representation of power flow and control behavior. Virtual instruments such as the LCD and virtual terminal were used to observe voltage, current, motor speed, and operating mode during simulation. This modeling approach ensured that the simulation environment closely matched real-world system behavior.

3.2. Control logic and workflow

The control logic of the hybrid energy storage system was implemented by uploading the Arduino program into the simulated microcontroller within Proteus (**Figure 2**). The Arduino code continuously reads the throttle input provided through a virtual potentiometer and processes it according to the predefined energy management strategy. The throttle value is monitored in real time and compared with a preset threshold to identify normal and peak power demand conditions. Based on the throttle input, the Arduino controls the relay switching logic to select the appropriate energy source. When the throttle variation remains below the threshold, the battery relay is activated, allowing the battery to supply power to the motor. When the throttle variation exceeds the threshold, indicating sudden acceleration, the controller deactivates the battery relay and activates the supercapacitor relay. This switching process follows the simulation flow illustrated in the flowchart and ensures a smooth transition between battery and supercapacitor modes without interrupting motor operation. The switching behavior,

relay response, and motor operation were carefully observed during simulation to verify the correctness of the control logic. The results confirmed that the control algorithm performs as intended and accurately follows the proposed energy management strategy.

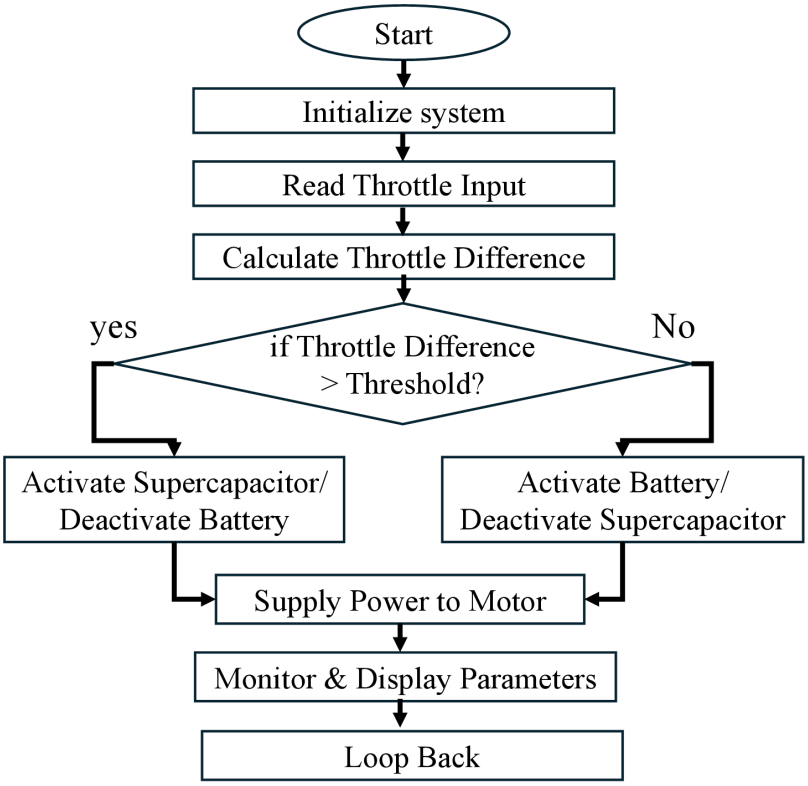

Figure 2. Workflow diagram of a hybrid energy storage system.

4. Results

This work presents the results obtained from the simulation and implementation of the IoT-based hybrid energy storage system using a battery and a supercapacitor for electric vehicle applications. The purpose of this work is to evaluate the performance of the proposed system under different operating conditions and to verify the effectiveness of the control strategy. In addition, the effectiveness of the proposed hybrid configuration in improving energy utilization and extending battery operating duration was also analyzed. The results include simulation-based analysis, comparison between battery-only and battery-supercapacitor operation, and evaluation of energy usage over time. Special emphasis is given to the improvement in battery duration achieved by integrating a supercapacitor, as illustrated in the comparative energy usage results.

4.1. Simulation results

When a control signal is sent by the microcontroller, the DC motor is activated via a motor driver circuit. The motor driver, composed of various electronic components, ensures smooth voltage delivery to the DC motor while minimizing fluctuations and protecting the motor from abrupt voltage changes. A Wi-Fi modem is integrated into the system to enable real-time monitoring of vehicle parameters over the internet. These monitored features include the SOC of the battery and the vehicle's speed, which are

tracked at different time intervals. The supercapacitor bank is designed to be charged via a solar panel mounted on the roof of the vehicle. **Figure 3** illustrates the circuit diagram in Proteus software. However, in our prototype setup, the supercapacitor is charged using an external battery source. The lithium-ion battery, on the other hand, is charged by converting AC voltage to DC using a full-bridge rectifier followed by a filter circuit to ensure stable charging. The throttle difference ranges from 1 to 100 units and serves as the key variable on which our prototype operates. It represents the variation in throttle position between two consecutive operational states of the vehicle. This difference determines whether the system draws energy from the battery or the supercapacitor.

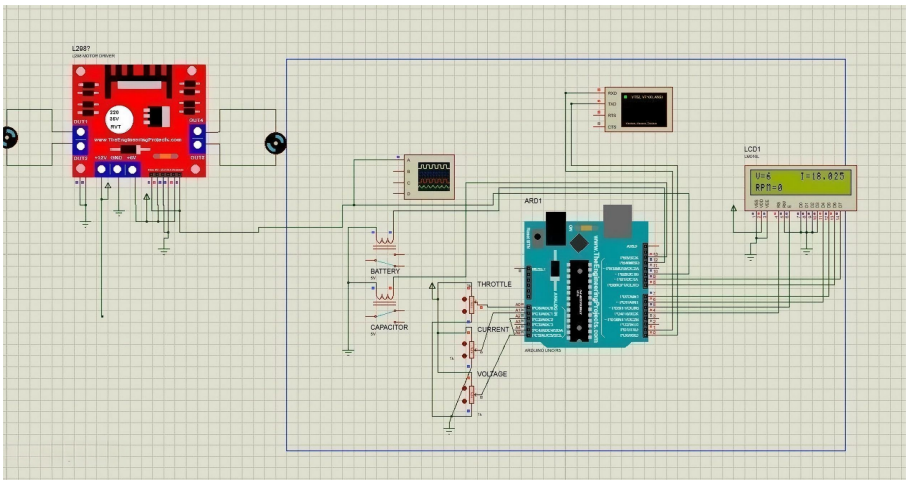

Figure 3. Circuit Diagram of Supercapacitor setup in Proteus.

In our setup, a threshold value of 50 units is predefined, serving as the boundary between the operating states of the battery and the supercapacitor. An algorithm, implemented through Arduino programming, monitors the throttle difference in real time. If the throttle difference between two-time instances is less than or equal to 50 units, the system draws power from the battery as shown in **Figure 4**.

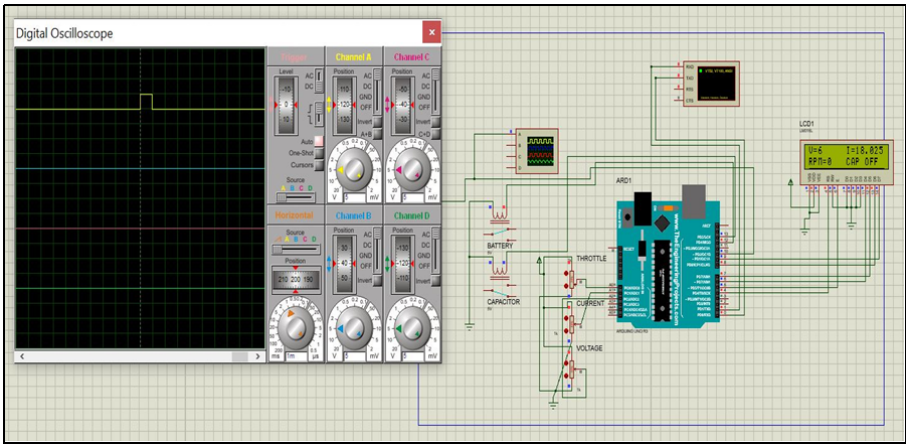

Figure 4. Simulation performance under a throttle difference of less than 50 units.

The throttle variation required to compute this difference is generated using a throttle potentiometer, which simulates acceleration and deceleration states in the prototype. The potentiometer shown in **Figure 1** is used to measure the throttle

difference. When this throttle difference remains below the preset threshold value, the microcontroller continuously sends a signal to the relay connected to the battery, keeping the battery circuit closed and supplying power to the system. This state persists until the microcontroller sends a signal to open the battery relay.

Whenever the throttle difference exceeds the set threshold, the system requires more energy. If this high energy demand is supplied solely by the battery within a short time, it can cause rapid battery drain, reducing the battery's overall lifecycle. To prevent this, the microcontroller sends a signal to open the battery relay and simultaneously closes the relay connected to the supercapacitor, as shown in **Figure 5**. The supercapacitor then acts as the primary energy source, quickly discharging to provide the extra charge needed by the system. This switching process continues with the microcontroller monitoring the throttle difference every 3 s. When the throttle difference drops below the threshold again, the system switches back to the battery as the power source. By offloading these short bursts of high energy demand to the supercapacitor, the battery is protected from rapid drain, thereby extending its lifetime. Additionally, the SOC of both the battery and the supercapacitor is continuously monitored and displayed via a mobile app connected through a Wi-Fi modem. This allows real-time tracking of the charge levels at any given time.

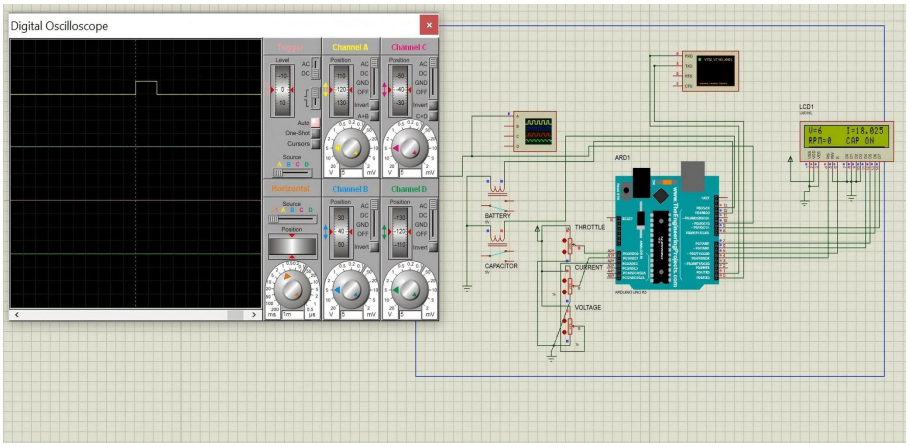

Figure 5. Simulation performance under a throttle difference greater than 50 units.

Before building the physical prototype, the expected results were first verified using Proteus Design Suite software. After confirming the simulation results, the prototype hardware was developed, as shown in **Figure 6**. The system's performance was evaluated in two conditions: a) With only the battery; b) Supercapacitor along with the battery. **Figure 7** presents a detailed comparison between the conventional battery-only energy storage system and the proposed battery–supercapacitor hybrid system under identical operating conditions. The results clearly demonstrate the advantages of hybridization in terms of voltage stability, energy consumption behavior, and operational duration.

Figure 7a illustrates the schematic voltage response of a lithium-ion battery and the hybrid battery-supercapacitor system when subjected to step load conditions. In the battery-only case, the voltage response is relatively slow and settles at a lower level due to the limited power handling capability of the battery and its internal resistance. On the other hand, the hybrid system shows a much faster voltage rise and achieves a higher and more stable voltage profile. This improved response is mainly due to the

supercapacitor, which can rapidly supply or absorb power during sudden load changes. As a result, voltage fluctuations are minimized, leading to smoother and more reliable system operation.

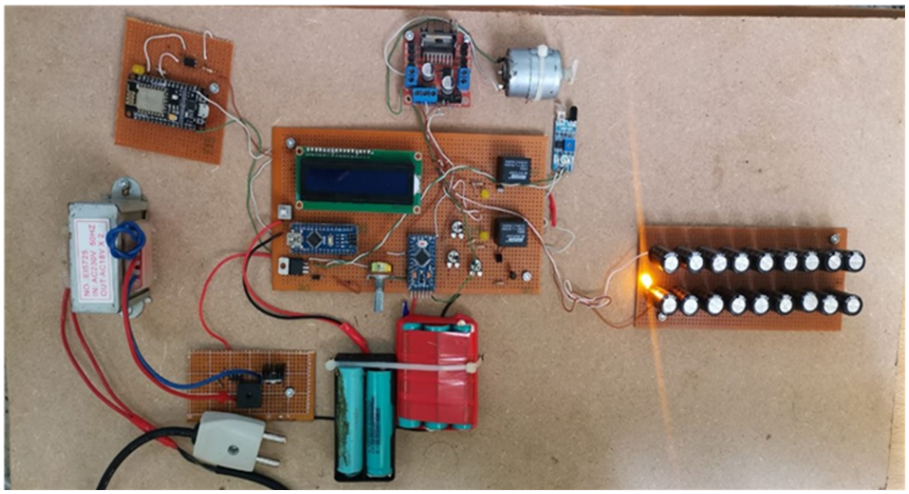

Figure 6. Hardware implementation of a prototype of a hybrid battery-supercapacitor system.

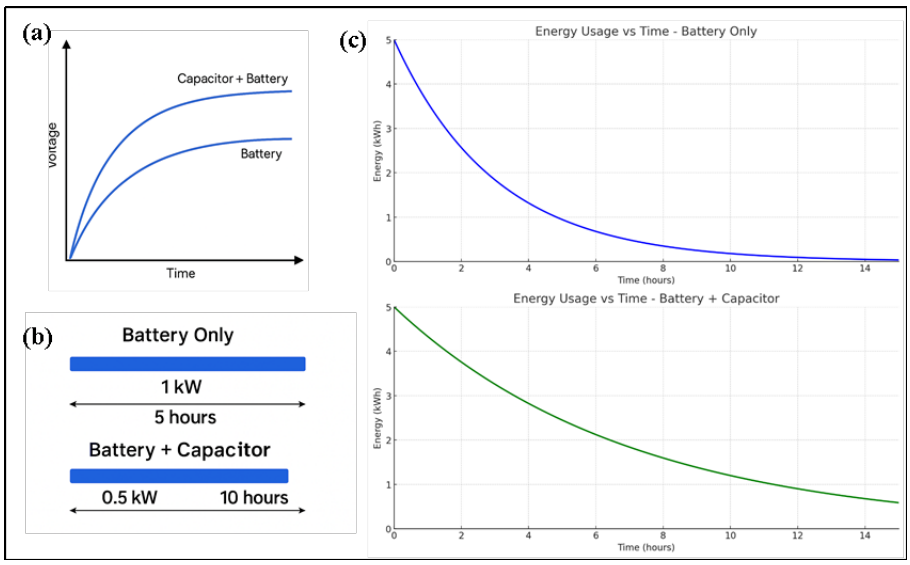

Figure 7. **(a)** Schematic voltage response of a lithium-ion battery and the proposed battery–supercapacitor hybrid system under step load conditions; **(b)** Comparison of energy consumption profiles for a battery-only system and the hybrid configuration under equivalent load conditions, showing reduced peak energy demand and slower decay in the hybrid system; **(c)** Operational time comparison between battery only and hybrid storage systems for a constant power requirement; **(d)** Power supply duration comparison between battery-only and hybrid system.

Figure 7b compares the energy consumption profiles of the battery-only system and the hybrid configuration under equivalent load conditions. It can be observed that the battery-only system experiences a rapid decline in stored energy, indicating higher peak energy demand and faster battery depletion. In contrast, the hybrid system exhibits a slighter and more gradual decrease in energy. This behavior confirms that the supercapacitor effectively supports transient and peak power demands, thereby reducing the energy drawn from the battery. Consequently, the battery operates under

less stressful conditions, which is beneficial for extending its lifetime. By offloading peak energy demands to the supercapacitor, battery degradation is estimated to decrease by 20–30% compared to traditional single-source systems. **Figure 7c** presents a direct comparison of the operational time for both configurations under a constant power requirement. When operating solely with the battery, the system supplies approximately 1 kW of power for nearly 5 hours before the stored energy is exhausted. However, in the hybrid configuration, the battery supplies a reduced average power of about 0.5 kW, while the supercapacitor assists during high-power demands. This load sharing allows the system to operate for approximately 10 h, effectively doubling the operational duration compared to the battery-only case. This result clearly highlights the significant improvement in battery usage efficiency achieved through hybridization. **Figure 7d** further illustrates the power supply duration comparison between the two systems. The battery-only configuration delivers a higher power level for a shorter time, followed by a sudden drop once the battery energy is depleted. In contrast, the hybrid system maintains a lower but more stable power output over a longer duration. This sustained power delivery demonstrates that the supercapacitor successfully reduces high current stress on the battery and enables a more controlled and gradual discharge process.

The results presented in **Figure 8** further analyze the performance of the proposed battery–superacapacitor hybrid system by comparing its energy output and power supply duration with a conventional battery-only configuration. These results provide deeper insight into how hybridization affects energy utilization and operational sustainability. **Figure 8a** shows the variation of cumulative energy output with time for both the battery-only system and the hybrid battery–supercapacitor system. In the battery-only case, the energy output increases rapidly during the initial hours due to the higher power draw from the battery. However, this rapid energy delivery leads to faster depletion of the battery. In contrast, the hybrid system exhibits a more gradual increase in energy output over time. Although the rate of energy output is lower, the hybrid configuration maintains energy delivery for a longer duration. This behavior indicates that the supercapacitor assists in meeting short-term power demands, allowing the battery to discharge at a slower and more controlled rate. **Figure 8b** presents a direct comparison of power supply duration between the two configurations. The battery-only system supplies a constant power of approximately 1 kW, but this power delivery is sustained only for about 5 h, after which the battery energy is exhausted, and the output abruptly drops to zero. On the other hand, the hybrid battery–supercapacitor system supplies a reduced but stable power of approximately 0.5 kW for nearly 10 h. This extended power supply duration clearly demonstrates the effectiveness of load sharing between the battery and the supercapacitor.

The results highlight that, while the battery-only system delivers higher power for a short time, the hybrid system prioritizes energy efficiency and longevity by spreading the energy output over a longer period. This trade-off is particularly desirable in electric vehicle applications, where sustained operation and reduced battery stress are more critical than short-term high-power output.

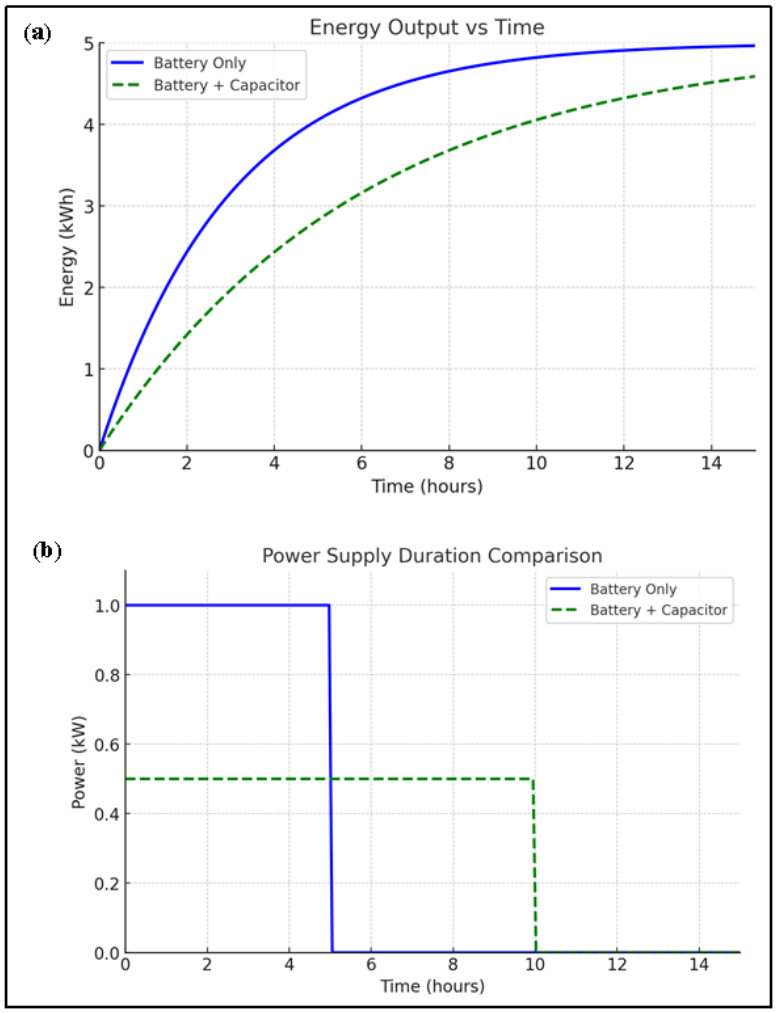

Figure 8. **(a)** Energy output as a function of time for a battery-only system and the proposed battery–supercapacitor hybrid, showing that the hybrid configuration delivers a smoother and more gradual energy profile over extended operation; **(b)** Power supply duration comparison for both configurations, highlighting that the hybrid system maintains continuous power for a longer period by reducing instantaneous load on the battery.

4.2. IoT hybrid energy storage system

The results presented in this work clearly demonstrate the effectiveness of the proposed IoT-based hybrid energy storage system that integrates a lithium-ion battery with a supercapacitor for electric vehicle applications. By analyzing voltage behavior, energy consumption, power delivery, and operational duration, the comparative evaluation between the battery-only system and the hybrid configuration provides strong evidence of the benefits achieved through energy storage hybridization. One of the most important observations from the results is the improvement in voltage stability under dynamic load conditions. The voltage response analysis shows that the battery-only system exhibits a slower response and lower steady-state voltage due to its limited power handling capability and internal resistance. In contrast, the hybrid battery–supercapacitor system responds more rapidly and maintains a higher and smoother voltage profile. This improvement is primarily attributed to the supercapacitor's ability to deliver high power almost instantaneously. Stable voltage behavior is critical for electric vehicle operation, as it directly influences motor performance, control reliability, and overall

system efficiency.

Energy consumption analysis further highlights the advantages of the hybrid system. The battery-only configuration experiences rapid energy depletion when subjected to equivalent load conditions, indicating higher peak energy demand and increased battery stress. When the supercapacitor is introduced, the energy decay becomes noticeably slower. This demonstrates that the supercapacitor successfully absorbs transient and peak power requirements, allowing the battery to operate in a more favorable and less stressful regime. As a result, the battery is protected from sudden high current draws, which are known to accelerate aging and thermal degradation. A key outcome of this study is the significant improvement in operational time achieved through hybridization. The results show that, for a constant power demand, the battery-only system supplies approximately 1 kW of power for about 5 h. In contrast, the hybrid system delivers a reduced average power of around 0.5 kW for nearly 10 h. This effectively doubles the operating duration of the system. Such an improvement is particularly valuable for electric vehicles, where extended driving range and efficient energy utilization are major performance indicators.

The energy output analysis further supports these findings. While the battery-only system delivers energy at a faster rate initially, it does so at the cost of rapid energy depletion. The hybrid system, on the other hand, provides a more gradual and sustained energy output over time. This controlled energy delivery reflects better load sharing between the battery and the supercapacitor, resulting in improved system endurance and reliability. Although the instantaneous energy output of the hybrid system is lower, its ability to maintain power delivery over an extended period makes it more suitable for real-world driving conditions. Power supply duration comparison also reveals a clear distinction between the two configurations. The battery-only system delivers higher power for a short duration, followed by an abrupt cutoff once the battery energy is exhausted. In contrast, the hybrid system maintains a steady and consistent power output for a longer period. This smoother power profile reduces mechanical and electrical stress on the drivetrain and power electronics, contributing to improved system durability.

Overall, the results confirm that integrating a supercapacitor with a lithium-ion battery significantly enhances energy management performance. The hybrid energy storage system improves voltage stability, reduces peak energy demand, extends battery operating time, and enhances overall system reliability. Additionally, the IoT-based monitoring framework enables real-time observation of key parameters, making the system more transparent and suitable for future optimization and intelligent energy management strategies.

5. Conclusions

The study developed an IoT-based energy management framework to enable real-time monitoring, control, and optimization of energy systems. The proposed system integrates sensors, microcontrollers, and wireless communication modules to continuously collect operational data such as voltage, current, power flow, state of charge, and load conditions. This data is transmitted to a remote interface, allowing users to observe system behavior and make informed decisions in real time. The IoT framework supports coordinated operation of energy storage devices, loads, and power electronics,

enabling efficient energy utilization and improved system reliability. By leveraging real-time data acquisition and communication, the proposed system enhances operational transparency, enables remote diagnostics, and supports intelligent energy management strategies. The major findings of the study are summarized as follows.

a. The IoT-based monitoring system successfully enables real-time visualization of key electrical and operational parameters, improving system awareness and facilitating timely detection of abnormal operating conditions.
b. Real-time data transmission and remote accessibility allow effective supervision and control of the energy system, reducing manual intervention and enhancing overall operational efficiency.
c. The integration of IoT technology improves coordination between energy sources, storage devices, and loads, leading to more stable system operation and optimized energy flow.
d. The proposed system demonstrates potential for reducing energy losses and improving system performance through data-driven monitoring and control, while also providing a scalable platform for future extensions such as predictive maintenance and intelligent energy optimization.

Despite its contributions, this study has several limitations that should be acknowledged. The proposed IoT-based energy system was implemented under controlled conditions and does not fully account for communication delays, data loss, cybersecurity concerns, or hardware reliability issues that may arise in real-world deployments. In addition, the system does not incorporate advanced data analytics or machine-learning-based decision-making, which could further enhance performance. Therefore, future work should focus on integrating intelligent data analytics, addressing cybersecurity and communication reliability, and validating the proposed framework through long-term real-world implementation to improve its robustness and practical applicability.

Author contributions: Both authors contribute equally to this work. AH: Conceptualization, investigation, formal analysis, review and editing, writing-original draft. MFA: Methodology, data curation, and writing-original draft, review and editing. Both authors have read and approved the final version of the paper.

Funding: There is no funding acquisition associated with the preparation of this manuscript.

Institutional review board statement: Not applicable.

Informed consent statement: Not applicable.

Data availability statement: All data and materials generated or analyzed during this study are available from the corresponding author on reasonable request.

Acknowledgment: The authors gratefully acknowledge the support and facilities provided by the University of Tsukuba and the National Institute for Materials Science (NIMS), Japan.

Conflict of interest: The authors declare no conflict of interest.

AI use statement: ChatGPT was used solely for rephrasing and polishing English sentences to improve clarity and fluency. All scientific ideas, experimental design, data acquisition, analysis, and conclusions were entirely conceived and carried out by the authors. The use of AI tools did not influence the scientific validity, originality, or integrity of the work. Accordingly, a statement specifying this limited use of AI assistance has been included in the final declaration of the manuscript.

References

1. Bocklisch T. Hybrid energy storage systems for renewable energy applications. Energy Procedia. 2015; 73: 103–111.
2. Hajiaghasi S, Salemnia A, Hamzeh M. Hybrid energy storage system for microgrids applications: A review. Journal of Energy Storage. 2019; 21: 543–570.
3. Zhao S, Peng W, Zhou L, et al. Metal-organic cage crosslinked nanocomposites with enhanced high-temperature capacitive energy storage performance. Nature Communications. 2025; 16: 769.
4. Chong LW, Wong YW, Rajkumar RK, et al. Hybrid energy storage systems and control strategies for stand-alone renewable energy power systems. Renewable and Sustainable Energy Reviews. 2016; 66: 174–189.
5. Gao Z, Fang C, Gao Y, et al. Hybrid electromagnetic and moisture energy harvesting enabled by ionic diode films. Nature Communications. 2025; 16: 312.
6. Hemmati R, Saboori H. Emergence of hybrid energy storage systems in renewable energy and transport applications–A review. Renewable and Sustainable Energy Reviews. 2016; 65: 11–23.
7. Nkwanyana TB, Siti MW, Wang Z, et al. An assessment of hybrid-energy storage systems in the renewable environments. Journal of Energy Storage. 2023; 72: 108307.
8. Bocklisch T. Hybrid energy storage approach for renewable energy applications. Journal of Energy Storage. 2016; 8: 311–319.
9. Choi M-E, Kim S-W, Seo S-W. Energy management optimization in a battery/supercapacitor hybrid energy storage system. IEEE Transactions on Smart Grid. 2011; 3: 463–472.
10. Fan Y, Qu W, Qiu H, et al. High entropy modulated quantum paraelectric perovskite for capacitive energy storage. Nature Communications. 2025; 16: 3818.
11. Lukatskaya MR, Dunn B, Gogotsi Y. Multidimensional materials and device architectures for future hybrid energy storage. Nature Communications. 2016; 7: 12647.
12. Cao J, Emadi A. A new battery/ultracapacitor hybrid energy storage system for electric, hybrid, and plug-in hybrid electric vehicles. IEEE Transactions on Power Electronics. 2011; 27: 122–132.
13. Wang S, Wang S, Wei Z, et al. A parts-per-million scale electrolyte additive for durable aqueous zinc batteries. Nature Communications. 2025; 16: 1800.
14. Ma H, Chen H, Chen M, et al. Biomimetic and biodegradable separator with high modulus and large ionic conductivity enables dendrite-free zinc-ion batteries. Nature Communications. 2025; 16: 1014.
15. Song Z, Hofmann H, Li J, et al. Energy management strategies comparison for electric vehicles with hybrid energy storage system. Applied Energy. 2014; 134: 321–331.
16. Tummuru NR, Mishra MK, Srinivas S. Dynamic energy management of renewable grid integrated hybrid energy storage system. IEEE Transactions on Industrial Electronics. 2015; 62: 7728–7737.
17. Vosen S. Hybrid energy storage systems for stand-alone electric power systems: optimization of system performance and cost through control strategies. International Journal of Hydrogen Energy. 1999; 24: 1139–1156.
18. Kumar K, Kwon S, Bae S. Deep reinforcement learning-based control strategy for integration of a hybrid energy storage system in microgrids. Journal of Energy Storage. 2025; 108: 114936.
19. Emrani A, Berrada A. A comprehensive review on techno-economic assessment of hybrid energy storage systems integrated with renewable energy. Journal of Energy Storage. 2024; 84: 111010.
20. Song Z, Hofmann H, Li J, et al. Optimization for a hybrid energy storage system in electric vehicles using dynamic programing approach. Applied Energy. 2015; 139: 151–162.
21. Babu TS, Vasudevan KR, Ramachandaramurthy VK, et al. A comprehensive review of hybrid energy storage systems: Converter topologies, control strategies and future prospects. IEEE Access. 2020; 8: 148702–148721.
22. Pan C, Fan H, Zhang R, et al. An improved multi-timescale coordinated control strategy for an integrated energy system

with a hybrid energy storage system. Applied Energy. 2023; 343: 121137.
23. Leon JI, Dominguez E, Wu L, et al. Hybrid energy storage systems: Concepts, advantages, and applications. IEEE Industrial Electronics Magazine. 2020; 15: 74–88.
24. Kong L, Yan G, Hu K, et al. Electro-driven direct lithium extraction from geothermal brines to generate battery-grade lithium hydroxide. Nature Communications. 2025; 16: 806.
25. Zhang Y, Jiang Z, Yu X. Control strategies for battery/supercapacitor hybrid energy storage systems. Publisher. 2008.
26. Geetha A, Subramani C. A comprehensive review on energy management strategies of hybrid energy storage system for electric vehicles. International Journal of Energy Research. 2017; 41: 1817–1834.
27. Liu H, Li C, Hu X, et al. Multi-modal framework for battery state of health evaluation using open-source electric vehicle data. Nature Communications. 2025; 16: 1137.
28. Podder AK, Chakraborty O, Islam S, et al. Control strategies of different hybrid energy storage systems for electric vehicles applications. IEEE Access. 2021; 9: 51865–51895.
29. Zheng C, Li W, Liang Q. An energy management strategy of hybrid energy storage systems for electric vehicle applications. IEEE Transactions on Sustainable Energy. 2018; 9: 1880–1888.
30. Atawi IE, Al-Shetwi AQ, Magableh AM, et al. Recent advances in hybrid energy storage system integrated renewable power generation: Configuration, control, applications, and future directions. Batteries. 2022; 9: 29.
31. Zhao P, Dai Y, Wang J. Design and thermodynamic analysis of a hybrid energy storage system based on A-CAES (adiabatic compressed air energy storage) and FESS (flywheel energy storage system) for wind power application. Energy. 2014; 70: 674–684.
32. Adeyinka AM, Esan OC, Ijaola AO, et al. Advancements in hybrid energy storage systems for enhancing renewable energy-to-grid integration. Sustainable Energy Research. 2024; 11: 26.
33. Sutikno T, Arsadiando W, Wangsupphaphol A, et al. A review of recent advances on hybrid energy storage system for solar photovoltaics power generation. IEEE Access. 2022; 10: 42346–42364.
34. Lukic SM, Wirasingha SG, Rodriguez F, et al. Power management of an ultracapacitor/battery hybrid energy storage system in an HEV. In: Proceedings of the 2006 IEEE Vehicle Power and Propulsion Conference; 6–8 September 2006; Windsor, UK.
35. Kim Y, Koh J, Xie Q, et al. A scalable and flexible hybrid energy storage system design and implementation. Journal of Power Sources. 2014; 255: 410–422.
36. Wang Y, Song F, Ma Y, et al. Research on capacity planning and optimization of regional integrated energy system based on hybrid energy storage system. Applied Thermal Engineering. 2020; 180: 115834.
37. Shen W, Zeng B, Zeng M. Multi-timescale rolling optimization dispatch method for integrated energy system with hybrid energy storage system. Energy. 2023; 283: 129006.
38. Das DC, Roy A, Sinha N. GA based frequency controller for solar thermal–diesel–wind hybrid energy generation/energy storage system. International Journal of Electrical Power & Energy Systems. 2012; 43: 262–279.
39. Pedram M, Chang N, Kim Y, et al. Hybrid electrical energy storage systems. In: Proceedings of the 16th ACM/IEEE International Symposium on Low Power Electronics and Design; 18–20 August 2010; Austin, TX, USA.
40. Garcia F, Ferreira A, Pomilio J, et al. Control strategy for battery-ultracapacitor hybrid energy storage system. In: Proceedings of the 2009 Twenty-Fourth Annual IEEE Applied Power Electronics Conference and Exposition; 15–19 February 2009; Washington, DC, USA.
41. Jing W, Lai CH, Wong WS, et al. A comprehensive study of battery-supercapacitor hybrid energy storage system for standalone PV power system in rural electrification. Applied Energy. 2018; 224: 340–356.
42. Xiong R, Chen H, Wang C, et al. Towards a smarter hybrid energy storage system based on battery and ultracapacitor—A critical review on topology and energy management. Journal of Cleaner Production. 2018; 202: 1228–1240.
43. Al-Ghussain L, Ahmad AD, Abubaker AM, et al. An integrated photovoltaic/wind/biomass and hybrid energy storage systems towards 100% renewable energy microgrids in university campuses. Sustainable Energy Technologies and Assessments. 2021; 46: 101273.
44. Aktas A, Erhan K, Ozdemir S, et al. Experimental investigation of a new smart energy management algorithm for a hybrid energy storage system in smart grid applications. Electric Power Systems Research. 2017; 144: 185–196.
45. Balachander K, Kuppusamy S, Vijayakumar P, et al. Comparative study of hybrid photovoltaic-fuel cell system/hybrid wind-fuel cell system for smart grid distributed generation system. In: Proceedings of the 2012 International Conference on Emerging Trends in Science, Engineering and Technology (INCOSET); 13–14 December 2012; Tiruchirappalli, India.
46. Zhang X, Wang Y, Lai X, et al. Ultrasound-based intelligent identification method for regions and defects of lithium-ion

batteries using a random forest model. Journal of Energy Storage. 2025; 132: 117746.
47. Wang Z, Feng Z, Hu C, et al. Enhancing battery performance under motor overload drive with a battery–supercapacitor hybrid energy storage system. Journal of Power Sources. 2025; 642: 236680.
48. Fang Z, Shek JK, Sun W. A review of grid-connected hybrid energy storage systems: Sizing configurations, control strategies, and future directions. Journal of Energy Storage. 2025; 118: 116226.
49. Zhang Y, Yuan C, Du X, et al. Capacity configuration of hybrid energy storage system for ocean renewables. Journal of Energy Storage. 2025; 116: 116090.
50. Ma B, Li P-H. Optimal flexible power allocation energy management strategy for hybrid energy storage system with genetic algorithm based model predictive control. Energy. 2025; 324: 135958.
51. Aruna P, Prabhu VV, Krishnakumar V, et al. Innovative optimization of hybrid energy storage systems for electric vehicles: Integrating FBPINN-SAO to enhance performance and efficiency. Journal of Energy Storage. 2025; 108: 115021.
52. Soonmin H, Taghavi M. Solar Energy Development: Study Cases in Iran and Malaysia. International Journal of Engineering Trends and Technology. 2022; 70: 408–422. doi: 10.3126/kjse.v8i1.69268
53. Taghavi M, Salarian H, Ghorbani B. Thermodynamic and exergy evaluation of a novel integrated hydrogen liquefaction structure using liquid air cold energy recovery, solid oxide fuel cell and photovoltaic panels. Journal of Cleaner Production. 2021; 320: 128821.
54. Ebrahimi A, Ghorbani B, Taghavi M. Novel integrated structure consisting of CO2 capture cycle, heat pump unit, Kalina power, and ejector refrigeration systems for liquid CO2 storage using renewable energies. Energy Science & Engineering. 2022; 10: 3167–3188.
55. Taghavi M, Lee CJ. Development of novel hydrogen liquefaction structures based on waste heat recovery in diffusion-absorption refrigeration and power generation units. Energy Conversion and Management. 2024; 302: 118056.

Energy Storage and Conversion 2025, 3(4), 3826.
doi: https://doi.org/10.59400/esc3826

Review

Ammonia synthesis and decomposition mediated by hydrides, imides, and amides

Muhammad Anis Aslam[1], Sajad Hussain[2], Ismat Ullah Khan[3,*]

[1] Shanghai Key Laboratory of Hydrogen Science & Centre of Hydrogen Science, School of Materials Science and Engineering, Shanghai Jiao Tong University, Shanghai 200240, China

[2] Department of Environmental Sciences, Comsats University Islamabad, Vehari Campus, Vehari 61100, Pakistan

[3] Department of Chemistry, Government Post Graduate College (GPGC), Lakki Marwat 28420, Pakistan

*** Corresponding author:** Ismat Ullah Khan, iukhan@chem.qau.edu.pk

CITATION

Aslam MA, Hussain S, Khan IU. Ammonia synthesis and decomposition mediated by hydrides, imides, and amides. Energy Storage and Conversion. 2025; 3(4): 3826. https://doi.org/10.59400/esc3826

ARTICLE INFO

Received: 3 August 2025
Revised: 7 September 2025
Accepted: 11 September 2025
Available online: 5 October 2025

Abstract: Ammonia is used for global fertilizer production and is increasingly viewed as a viable carrier for renewable hydrogen and long-duration energy storage. Realizing this potential requires catalysts and process architectures that enable both N_2-to-NH_3 synthesis and NH_3-to-H_2 decomposition at substantially reduced temperature and pressure. This review surveys recent advances in which alkali- and alkaline-earth metal hydrides, amides, and imides act as dynamic redox and hydrogen/nitrogen-transfer media, undergoing reversible interconversion with N_2, H_2, and NH_3. We summarize thermocatalytic systems where hydridic H^- and electron-rich lattices promote N_2 activation, heterolytic H_2 cleavage, and N–H bond formation, including composite catalysts that exploit cooperative interfaces with transition metals and complex or mixed-anion hydrides that relax constraints imposed by conventional metal-only surfaces. We also discuss photo-assisted routes that leverage defect-stabilized charge carriers in hydrides to drive nitrogen conversion under illumination, and chemical-looping strategies that decouple nitrogen fixation from hydrogenation (or hydrogen release) to tune thermodynamics and mitigate competitive adsorption. Across these platforms, recurring motifs include lattice-mediated hydride/proton shuttling, interfacial electron donation, and reversible nitride–imide–amide formation that can be engineered to balance activity, selectivity, and stability. Finally, we outline key barriers to practical deployment, air/moisture sensitivity, carrier volatility, phase segregation, and limited operando understanding and highlight design priorities for stabilizing reactive phases and integrating reactors compatible with renewable heat, photons, or electricity, thereby enabling scalable and decentralized ammonia and hydrogen technologies.

Keywords: ammonia synthesis; hydrogen production; hydrides; imides; amides

1. Introduction

The consequences of global warming witnessed in the past century have led to the need to design and develop clean and sustainable sources of energy [1, 2]. Renewable energy is by far one of the most imperative sustainable solutions to the reduction of the environmental damage that the vast use of fossil fuels has created. Nonetheless, intermittency and uncertainty of renewable energy and the geographical disparity between energy production and consumption centers are serious obstacles to power generation through these sources. Such a gap complicates the provision of energy needs in the world. Thus, to narrow these time and space gaps, a special supply-demand

management system should be developed [3]. Replacement of carbon-based fuel by hydrogen-based energy carriers can be done through the fact that hydrogen is a high-energy storer, and its gravimetric density of 120 MJ per kilogram is very high [4]. However, hydrogen is not an efficient long-range energy carrier because its volumetric energy density of 9.8 kJ/L at standard temperature and pressure (STP) is much less than that of gasoline (31.7 MJ/L) and methanol (15.8 MJ/L) [5, 6]. The carbon footprint should be mitigated by coming up with sustainable technologies that would utilize, or utilize rather indirectly, carbon-free energy carriers. Hydrogen production through sustainable means is a subject that has been receiving a lot of attention in the last few decades, and this has led to the introduction of new and more efficient processes of producing H_2 using various hydrogen-based resources [7–10]. Hydrogen, being the lightest gas, has a much lower liquefaction temperature (about −250 °C) than the rest and needs a significantly greater volume per unit mass. To overcome these challenges, hydrogen can be transported and stored safely by converting it to a different chemical, which is commonly referred to as an energy vector. It can then be applied on-site by decomposing thermally or endothermically reforming it to the desired form [11]. Other promising materials to store liquid hydrogen transportable are chemical hydrides, ammonia, methanol, methylcyclohexane, formic acid, and methanol. Methanol was one of the initial alternatives to be considered in making hydrogen locally, but as it emits CO_X, it cannot be used in car engines. In addition, some of the metal hydrides, including $NaAlH_4$, $Mg(BH_4)_2$, and $LiAlH_4$, have been investigated as carbon-neutral sources to recycle hydrogen but were incapable of meeting the demands of on-site, reversible hydrogen storage. In the same way, the metal amine salts and metal–organic frameworks (MOFs) have been studied in terms of sustainable hydrogen production. Nevertheless, such techniques are not as viable as commercial applications because of the low capacity of MOFs to store hydrogen, and the challenges of thermal manipulation of amine-containing systems (including ammonia production). The Haber-Bosch process is the most common method of producing industrial amounts of ammonia today, with N_2 and H_2 reacting at high temperature (350–500 °C) and pressure (15–35 MPa) in the presence of an iron-based catalyst to produce NH_3 [12–14]. This process is known to be energy-demanding, and its carbon footprint is high, with an estimated consumption of 1~2% of the worldwide energy input and an annual carbon dioxide emission of more than 670 million tons. The proportion of the energy input into the process converted to the chemical energy of the ammonia molecule is approximately 60%; the remainder of the energy is lost, primarily in the hydrogen production of natural gas, production of ammonia, and gas separation [15–17]. The dissociation of ammonia is an endothermic reaction and is accompanied by rising entropy, and theoretical equilibrium conversion is greater than 99% at 400 °C. Nevertheless, high conversion rates are typically attained at high temperatures exceeding 600 °C because of a large kinetic barrier. Thus, the creation of an efficient catalyst is an issue of burning importance, and Ni-based and Ru-based catalysts are under analysis to this day. Ammonia synthesis and decomposition [18–21] are shown in **Figure 1**.

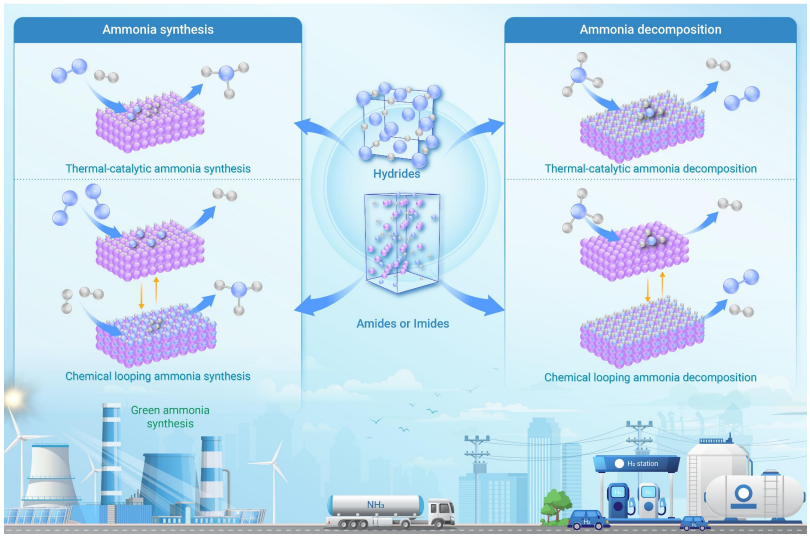

Figure 1. Roadmap: ammonia synthesis and decomposition were mediated by Hydrides, Imides, and Amides [22].

Recent work shows that alkali and alkaline-earth metal hydrides, amides, and imides can participate dynamically in nitrogen and hydrogen transformations. Their strongly reducing character, reversible interconversion among H- and N-containing phases, and cooperative behavior with transition metals enable alternative pathways for N_2 activation, N–H bond formation, and NH_3 decomposition, often under milder conditions than traditional metal catalysts. These materials also support chemical-looping concepts that separate nitrogen fixation from hydrogenation (or hydrogen release), reducing competitive adsorption and allowing thermodynamic tuning.

This review consolidates advances in thermocatalytic ammonia synthesis and cracking enabled by hydride/amide/imide chemistry, surveys photo-assisted routes that exploit long-lived charge carriers in hydrides, and evaluates chemical-looping strategies for both ammonia production and hydrogen generation. We highlight mechanistic insights, performance-limiting steps, and materials/reactor challenges—particularly air/moisture sensitivity, carrier volatility, phase segregation, and the need for operando understanding—to guide the design of robust, scalable systems compatible with renewable heat, photons, or electricity.

2. Ammonia as a hydrogen storage medium

Ammonia is a hydrogen storage and transportation medium that has a number of advantages. These are a large hydrogen storage capacity (17.7 wt.%), a comparatively simple liquefaction (at low temperatures, 0.86 MPa), a high volumetric energy density (108 kg H_2 m^{-3}), zero emissions of carbon, and the capability to generate the gas in large amounts by the well-established Haber-Bosch (HB) process. Still, the conventional HB process consumes a lot of energy and generates a lot of CO_2. Numerous methods of modernizing the existing technology have been suggested to make the synthesis of ammonia sustainable, with an emphasis on the use of water electrolysis to generate hydrogen [23,24]. The steam reforming of methanol or methane ($CH_4 + H_2O \rightleftharpoons CO + 3H_2$, with an enthalpy change of +68.7 kJ per mole of H_2) consumes more energy

compared to the decomposition of ammonia ($2NH_3 \rightleftharpoons N_2 + 3H_2$, with an enthalpy change of +30.6 kJ per mole of H_2). Therefore, ammonia decomposition is more economically feasible for on-site hydrogen regeneration [25]. The decomposition of ammonia in the production of H_2 has received significant attention, especially in the efforts to have a complete understanding of the reaction process. This is aimed at keeping the lowest practical reaction temperature and maximizing the conversion and hydrogen generation rate [26–29].

Thermodynamically, high conversion is achievable at 300 to 350 °C, ammonia can be broken down, and the conversion back to 96.0 to 98.0%. Nevertheless, the degradation of NH_3 catalyzed is normally at higher temperatures (above 450 °C) due to kinetic limitations. As a result, past researches have paid significant attention to the creation of catalysts that can decompose NH_3 at reduced temperatures [30–32]. Numerous strategies have been explored to lower the operating temperature of NH_3 decomposition, including tuning active-metal composition and particle size, optimizing supports, modifying reactor architectures, and engineering adsorption energetics. Reported intrinsic activity trends for NH_3 decomposition commonly place Ru among the most active metals; however, Ru catalysts can still show limited performance at ≤450 °C and are constrained by high cost. These limitations motivate the development of Ru-free alternatives, including Fe-, Ni-, and Co-based catalysts and bimetallic systems (e.g., CoMo, NiFe), often combined with high-surface-area supports (Al_2O_3, SiO_2, CaNH) and electronic promoters (K, Na, La, Ce) to improve activity and stability under practical conditions [33–42].

The comparison between ammonia and other common fuels is presented in detail in **Table 1**, but special attention is given to the energy density, heating values, and the volumetric and energetic costs [43]. Previous research has demonstrated that alkali metal hydrides and ammonia could offer a form of reversible hydrogen storage substance with a high capacity and the capability to liberate hydrogen under moderate conditions spontaneously. In this process, the reaction of desorption of hydrogen can be represented:

$$MH + NH_3 \rightarrow MNH_2 + H_2 (M = Li, K \text{ and } Na)$$

Table 1. Comparison between NH_3 and conventional fuels.

Type of fuel/storage	HHV ($MJkg^{-1}$)	Density (kgm^{-3})	Energy density (GJm^{-1})	P (MPa)	Specific energetic cost ($\$GJ^{-1}$)	Specific volumetric cost ($\$m^{-3}$)
H_2/metal hydrides	142	25	3.5	1.4	35.2	125
CNG (CH_4)/integrated storage system	55.5	188	10.4	25	38.3	400
Gasoline (C_8H_{28})/liquid tank	46.7	736	34.4	1	29.1	1000
Methanol	15.2	749	11.4	1	60.9	693
LPG	48.9	288	19	1.4	28.5	542
NH_3/metal amines	17.1	610	10.4	1	17.5	183
NH_3/pressurized tank	22.5	603	13.5	1	13.3	181

Note: HHV: Higher heating value, CNG: compressed natural gas, and LPG: liquefied petroleum gas.
Source: Reprinted with permission from the studies by Zamfirescu and Dincer [43] and Klerke et al. [44].

The key difficulty in creating hydrogen storage material using alkali metal hydrides and ammonia is to attain not only excellent kinetics of both hydrogenation and dehydrogenation taking place, but also a high storage capacity. The Li-NH_3 system contains the most hydrogen (8.1 wt.%) of the systems examined, and due to its exothermic hydrolysis-type reaction, it is possible to operate at relatively lower temperatures [45–48]. Li-NH_3 can also be improved with 5 mol.% of KH and KNH_2, which will enhance the kinetics of hydrogen desorption/absorption significantly. Attractive research is underway to study the catalytic properties of these compounds on the Li-NH_3 system, depending on potassium. Hydrogen desorption characteristics of the reactions between lithium hydride and NH_3 at temperatures of 50–200 °C in the presence of various particle sizes. The possibility of applying multiple potassium compounds to serve as catalysts to enhance the kinetics of the hydrogen desorption process of the Li-NH_3 system. In a study, it was revealed that three methods are efficient in enhancing the desorption kinetics of this system: doping by using potassium compounds, increasing the reaction temperature, and ball milling of the LiH particles to decrease their size [49]. As of late, new advancements in large-scale water electrolysis have provided significant promise in terms of the commercial generation of green hydrogen. A water electrolysis method should be sustainable, and to achieve this, power that is generated in a carbon-neutral environment, e.g., solar and wind energy, can be used. Then, in the cases where the commercial use is applicable, the nitrogen in the cryogenic air distilled mix and the green H_2 generated in the process could be combined to create carbon-free green ammonia. The NH_3 can then be cheaply distributed to all parts of the world and stored through the large capacity infrastructure that is now in existence. Finally, ammonia breakdown units that are located on-site could generate carbon-free, renewable H_2, which can be applicable in hydrogen refueling stations, fuel cells, internal combustion engines, or power generation systems. This discussion examines the prospects and challenges of the use of ammonia as an energy carrier and emphasizes the importance of hydrogen as a future fuel. It evaluates the methods of H_2 generation with the breakdown of NH_3 in different working conditions with reactor types and catalysts. The three major barriers to the establishment of a hydrogen-based economy of tomorrow are the creation of effective reactor systems, the advancement of H_2 purification technology, and the creation of cheap and efficient catalysts. At this point, there is a lot of research being conducted on the utilization of metal hydrides in ammonia synthesis and degradation. This research also has a comprehensive techno-economic analysis and operational feasibility study of a number of reactor designs. It gives recommendations to hasten the commercialization process, as per the literature, as well as our experience, to achieve maximum efficiency of the NH_3 breakdown and generation of green H_2. Considering the above, the creation of efficient catalysts and innovative processes of ammonia generation and breakdown under moderate conditions is urgent but extremely difficult for the development of the energy economy of ammonia-hydrogen. Indicatively, these recent reports have shown many types of new catalysts to ammonia synthesis, including electrodes supported metals (Ru/C12A7: e^- [50], Ru/Ca_2N: e^- [51,52], etc.), intermetallic compounds (LaCoSi [53], LaRuSi [54], etc.), rare earth metal nitrides or carbides supported transition metals

(LaN [55,56], CeN [57], CeC_2 [58], etc.). Moreover, since one of the centers of this review is hydrides, which contain hydride ions (H^-), strong reducing activities, and have a special role in the activation of nitrogen, they contain hydrogen [59]. At present, the hydrides mostly being utilized in the production of ammonia are: (i) binary metal hydrides (LiH [16], BaH_2 [60], TiH_2 [61] etc.), (ii) complex hydrides (Li_4RuH_6, Ba_2RuH_6, etc.) [62], (iii) mixed anion hydrides (Ln-OH [63], Sm_2O_3 (Sm-H) [64], $TiO_{2-x}H_y$ [65], Ba_5CrN_4H [66], $BaCeO_{3-x}N_yH$ [67], Hydride materials above, either (co)-catalysts or catalyst supportes in thermocatalytic ammonia production, alkali or alkaline earth metal hydrides (such as LiH, BaH_2) [68,69] as nitrogen carriers in chemical looping ammonia synthesis (CLAS) have been shown to perform well. The primary catalysts used in the breakdown of ammonia are (i) supported or non-supported monometallic catalysts (e.g., Fe, Co, Ni, Ru, Rh, Pt, Ir) [70–74]; (ii) supported or non-supported metal alloy catalysts (e.g., FeCo, CoNi) [75–78]; (iii), metal carbide catalysts (e.g., WC, MoC) [79]; (iv), metal nitride [2,6,25,80–87].

3. Thermocatalytic ammonia synthesis

3.1. Alkali and alkaline earth hydrides as catalysts

Ammonia synthesis, the opposite of ammonia breakdown, is a more significant process in catalysis and is regarded as a bellwether [61]. It is one of the reactions that has been most studied regarding heterogeneous catalysis. Over the previous century, the majority of periodic table elements have been sieved and judged on their catalytic ability in the rate of ammonia generation [88]. Fused iron and supported Ru catalysts have also been prepared in the case of the KAAP process and the Haber-Bosch process. There has been a well-established trend in volcanoes, which shows the extent to which the action of the ammonia synthesis process is sensitive to the nature of the transition metals. This pattern of activity has been successfully explained by the concept of energy scaling relations, i.e., the idea that the energies of the adsorption of reactive species on transition-metal surfaces scale with one another. Alloys or transition metals with small N adsorption energies, such as Fe, Ru, and CoMo, are useful catalysts in the synthesis of ammonia. Other transition metals do not because they will not bind N at all (strongly enough; Ni), or bind it too strongly (early 3d metals V, Cr, and Mn). A major challenge to the production of ammonia is the energy scaling relations [89,90].

3.2. Transition metals alkali hydride composite catalysts

The active for ammonia synthesis would make a suitable ammonia decomposition catalyst. We should naturally investigate the TM-Li_2NH combination for ammonia production. Higher H_2 partial pressure causes Li_2NH to convert to LiH, as shown in **Figure 2**. Therefore, in ammonia synthesis conditions, the TM-Li_2NH composite would change to TM-LiH. When early and late 3d transition metals from V to Ni come into contact with LiH, their kinetic behaviors and catalytic performances are dramatically changed [16]. **Figure 3a,b** illustrates how the addition of LiH at 573 K and WHSV of 600.000 mL g_{cat}^{-1} h^{-1} can increase ammonia synthesis rates by up to 3–4 orders of magnitude (except for Fe) when compared to bare TM(N). It has been

demonstrated that certain TMs, namely VN and CrN, as well as Ni, a late TM, are catalytically inactive; yet, they can catalyze the creation of ammonia at the proper rates when they combine with LiH. It's important to note that the Cr-, Mn-, Fe-, and Co-LiH catalysts have measurable activity at 423 K; at 523 and 573 K, they perform 12–20 and 2–3 times better, respectively, than the reference RuCs/MgO catalyst, as shown in **Figure 3c**.

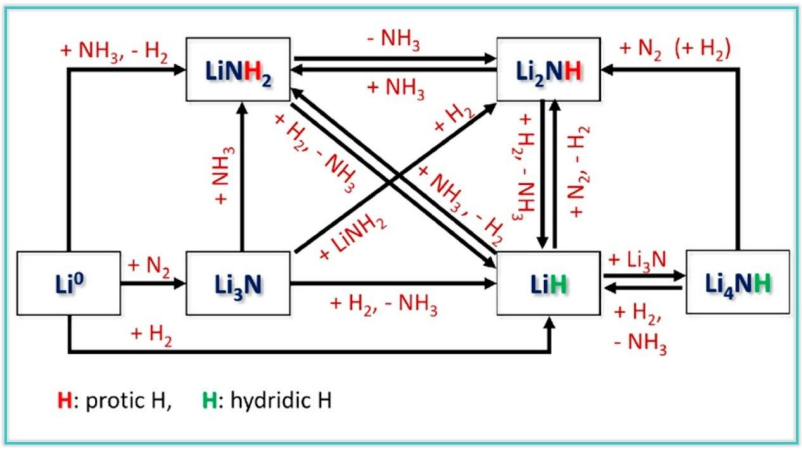

Figure 2. The lithium metal, hydride, nitride, amide, imide, and nitride-hydride interconvert [90].

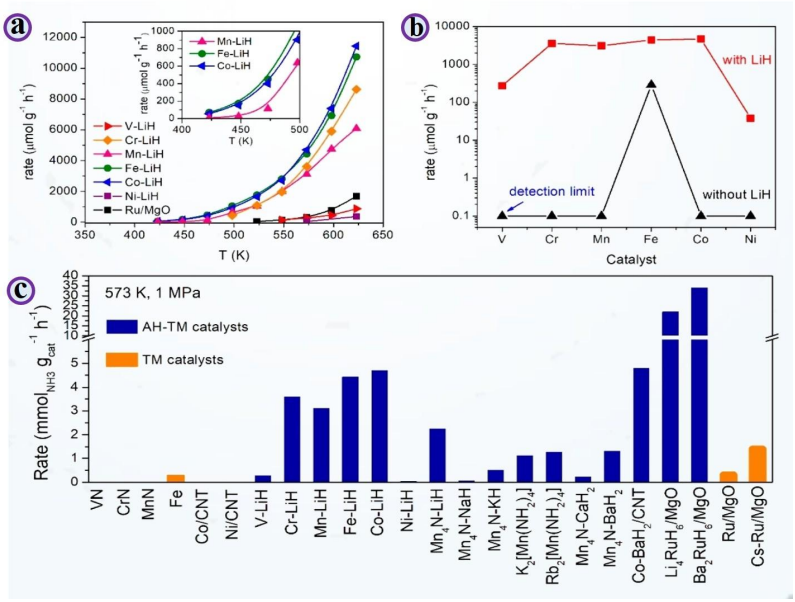

Figure 3. **(a)** Synthesis rate of ammonia of a series of TM-LiH catalysts versus temperature; The inset is the magnified version of the rates in the temperature range 420 to 500 K. N_2/H_2 = 1:3, pressure = 1 MPa; **(b)** activity of 3d TM (V to Ni) with or without LiH at 573 K and 1 MPa [16]; **(c)** Rates of ammonia synthesis regarding a sequence of alkali/alkaline earth hydroxide-containing catalysts and reference catalysts [22].

The most interesting experimental observation is the fact that, rather than the normal volcano-like behavior, the Cr-, Mn-, Fe-, and Co-LiH catalysts display similar activities and a high-land-like behavior (**Figure 3b**). This indicates that LiH enhances the catalytic activity of these TM(N) or causes an absence of catalysis depending on the binding energy of the transition metals to N. It is a clear indication that the

scaling relations of TM-only surfaces have been overused. Li was demonstrated to have the least promoting effect on transition metals in the synthesis of ammonia, with known ample promoting effects of the hydroxides of alkali or alkaline earth metals, in particular those of K, Cs, and Ba, on transition metals. The notable impact of LiH on TM is not typical. LiH is primarily distinguished from its (hydro)oxide counterparts by the existence of H–, an electron and proton carrier essential to its operation (i.e., H– in LiH may undergo reductive addition to form an N–H bond and weaken the N≡N triple bond). Additional research with other alkali and alkaline earth metal hydrides for ammonia catalysis highlights the significance of H^-. One way to increase the catalytic activity of Co metal is to combine it with barium hydride (BaH_2) [91]. The rate of ammonia synthesis of the Co-BaH_2 catalyzed by carbon nanotubes (CNTs) is around two orders of magnitude faster than the rate of BaO-Co/CNTs at 573 K and 1 MPa. On the same note, the catalytic activity of Mn nitride (e.g., Mn_4N) is enhanced one to three orders of magnitude by the presence of NaH, KH, CaH_2, or BaH_2. Mn nitride is mainly promoted in the AH order of BaH_2, LiH, KH, CaH_2, and NaH. This is not similar to conventional alkali or alkaline earth (hydra)oxide promoters [60]. **Figure 3c** shows the rates of ammonia synthesis of a series of TM-AH composite catalysts at different temperatures of 573 K and pressures of 1 MPa.

The linkage between transition metals, hydrogen, nitrogen, alkali/alkaline earth metals, and nitrogen is intuitive, and thus it is not surprising that hydride catalysts exhibit a great deal of increased activity. We proposed a two-active-center paradigm, which shows the synergy between the use of AHs and TM in catalyzing ammonia production. The rationale behind this model is the fact that separate TM and AH phases comprise the functional 3d TM-AH catalysts. This model entails three steps (**Figure 4a**) [16]. A useful framework is a dual-site mechanism in which adjacent transition-metal (TM) and alkali/alkaline-earth hydride (AH) phases cooperate. In this view, (i) N_2 is activated on TM sites, (ii) activated N species are transferred to the neighboring hydride phase, where hydridic H^- and electron density facilitate N–H bond formation, and (iii) subsequent hydrogenation steps proceed via heterolytic H_2 activation at the TM–AH interface, ultimately releasing NH_3 while regenerating reactive sites. This cooperative chemistry can mitigate limitations imposed by scaling relationships on TM-only surfaces, although key details—including interfacial structure, charge/proton (hydride) transfer pathways, and the dominant adsorption modes of N_2 and H_2—remain active topics of investigation.

Gas-phase cluster reaction experiments to provide profound mechanistic insights into the relationship between hydrides and transition metals. It has been suggested that structurally well-defined gas-phase clusters produced by a catalyst are appropriate models to match the catalyst's reactive site. Clusters formed from an Fe-LiH catalyst by laser ablation using gas-phase optical spectroscopy combined with mass spectrometry and quantum chemical computations [93, 94]. Several intricate hydride clusters, including $[LiNH2]^-$ [95] and $[Li_5FeH_6]^-$, were discovered. These hydride clusters changed into $[FeNH_2]^-$ and $[LiNH_2]^-$ moieties upon coming into contact with N_2, demonstrating the cleavage of the N≡N link as well as the production of N–H, Li–N, and Fe–N bonds (**Figure 4b**). While it is challenging to use traditional methods to

define the Fe-LiH catalyst's surface composition, the aforementioned cluster reactions suggest that [Li–Fe–H] species might be present and operate as the reactive site for N_2 activation and hydrogenation through an alternative mechanism. We speculated on the possibility that complex transition-metal hydrides could serve as effective catalysts for the synthesis of ammonia in light of these findings [92].

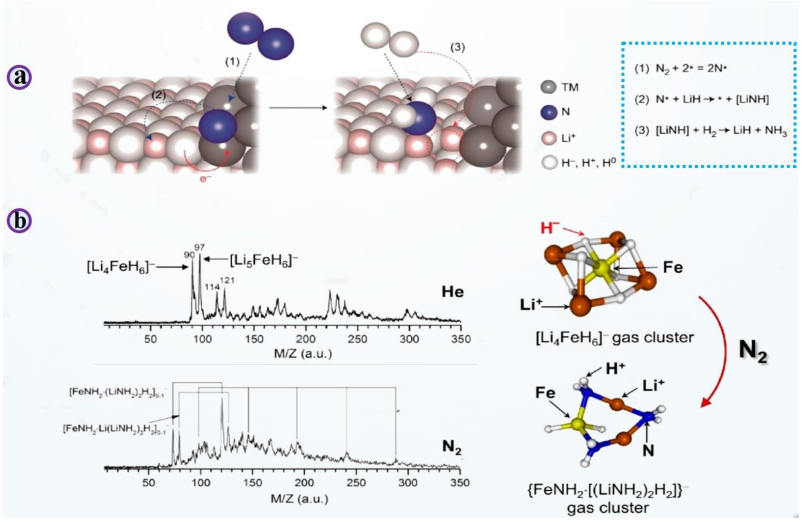

Figure 4. **(a)** Proposed reaction mechanism of ammonia synthesis catalyzed by TM-AH composite catalysts [16]; **(b)** Lithium iron hydride gas clusters react with N_2 to form [$LiNH_2$]-containing clusters [92].

3.3. Complex hydride catalysts

Although Li_4FeH_6 is known, it requires extreme synthesis conditions, whereas several ternary Ru hydrides (e.g., Li_4RuH_6 and Ba_2RuH_6) can be prepared under far milder conditions. These materials provide a practical testbed for the concept that complex hydrides can function as catalytic platforms for ammonia synthesis. Reported activity data show that Ba_2RuH_6 (often used with MgO) is among the most active catalysts under comparatively mild conditions; for example, at 573 K, its NH_3 synthesis rate exceeds that of conventional Cs–Ru/MgO, and ppm-level effluent NH_3 has been detected near ambient pressure at lower temperatures, as shown in **Figure 5a** [95–97].

It is generally accepted that on a standard TM catalyst, N_2 is largely adsorbed dissociatively on active sites that contain many metal atoms, like C7 or B5 sites on the surface of Fe or Ru, respectively. The active sites on Li_4RuH_6 and Ba_2RuH_6 are, however, constituted by the electron- and H-rich [RuH_6] anion and the Li or Ba cations surrounding it, and the long RuRu atomic distance defines why N_2 is not an adsorbate in a dissociative manner. A chemical alternative pathway was discovered through effective collaborative work with Vegge et al. Theoretical calculations on a Li_4RuH_6 model confirmed the (110) facet by showing an H-assisted associative activation of N_2 on the [RuH_6] center (**Figure 5b,c**). Firstly, N_2 adsorbs on the [RuH_6] site in an end-on complex. H^- is gradually carried to the polarized N-N antenna to generate a set of NxHy (x = 0–2, y = 0–3) intermediates by reducing it with protons of the surrounding Li cations. H_2 is then switched on to replenish the surface. It is the interaction of the transition metals, hydridic hydrogen, and alkali cations that allows the unique reaction pathway of the synthesis of ammonia with a short energy span of 1.75 eV, which prefers N_2 to NH_3 at

lower temperatures. This mechanism is experimentally supported by FTIR of adsorbed N_2 and NH_2 compounds, and tests involving $15N_2$-$14N_2$ isotope exchange [97–99].

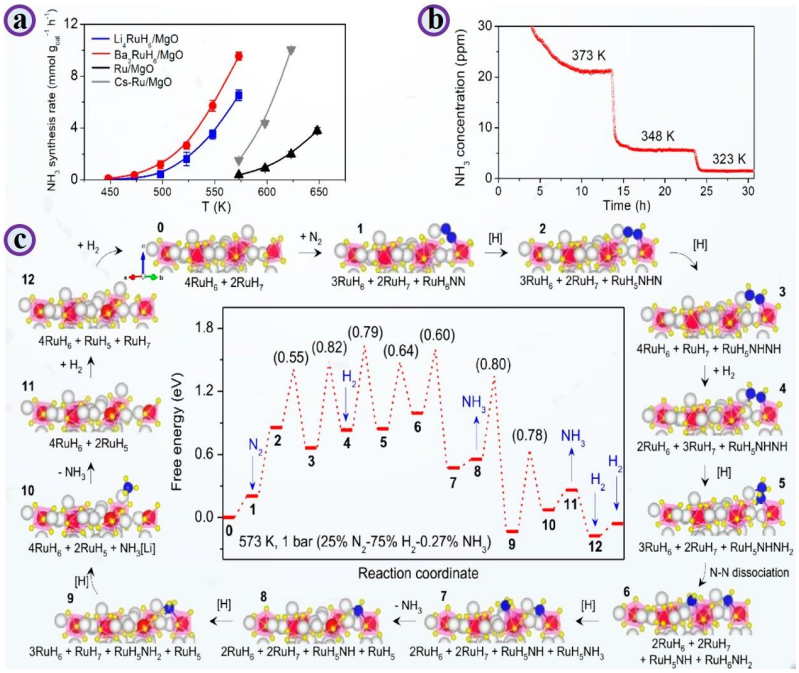

Figure 5. **(a)** Temperature-dependent NH_3 synthesis rate of various Ru catalysts at 0.1 MPa with H_2: N_2 = 3:1; **(b)** Time course effluent concentration of the ammonia synthesis of various Ru complex catalysts at 0.1 MPa with H_2N_2 = 1:3 and WHSV = 10800 $mLg^{-1}h^{-1}$; **(c)** calculates the free-energy pathway of the associative mechanism of ammonia synthesis over Ru complex catalysts [97].
Note: Color code: Ru: red, Li: white, H: yellow, N: blue.

3.4. Mixed-anion hydride catalysts

Recently, there has been a lot of interest in mixed-anion materials, including oxyhydrides and oxynitrides, because of their unusual characteristics, like rapid hydride ion conductivity, increased ferroelectric behavior, and significant catalytic activity [67, 100]. The kinetic and isotope exchange experiments showed that the hydrogen of the lattice in the $Ru/BaTiO_{2.5}H_{0.5}$ took part in the catalytic cycle, according to the Mars-van Krevelen mechanism of NH_3 formation (**Figure 6a**), and the phenomenon of hydrogen poisoning the catalyst was significantly reduced. His performance is higher than that of Co-based catalysts of the state of the art. The $BaAl_2O_{4-x}H_y$ has a stuffed tridymite structure and interstitial cage sites that contain anionic electrons. The surface of it has an ultralow work function (1.7–2.6 eV), and thus, it can strongly contribute to electron donation to Co, significantly reducing N_2 to NH_3 with the help of lattice H^- ions (**Figure 6b**). This three-dimensional, tetrahedrally built structure of the stuffed tridymite structure based on AlO_4 affords a high degree of chemical stability, which guards against oxidation of both the anionic electrons and hydrogen ions that are present in the structure. This structural strength guarantees a higher level of resistance to the environment and reusability of the catalysts compared to other reported hydride-based systems [101]. **Figure 6c** shows the Development of perovskite-type oxyhydrides such as Ru-loaded $BaCeO_{3-x}N_\gamma H_x$, enabling highly active ammonia synthesis, with N_2 dissociation on

$BaCeO_{3-x}N_\gamma H_x$ surfaces faster than N–H bond formation. Ru/$BaCeO_3$ follows a Langmuir–Hinshelwood mechanism where N_2 and H_2 are dissociatively adsorbed on Ru, with N_2 dissociation as the rate-determining step. For Ru/$BaCeO_{3-x}N_\gamma H_x$, Hosono et al. proposed a Mars–van Krevelen mechanism involving lattice N or anion-vacancy-activated N_2 reacting with lattice H^- to form NNH intermediates that hydrogenate to NH_3 [87].

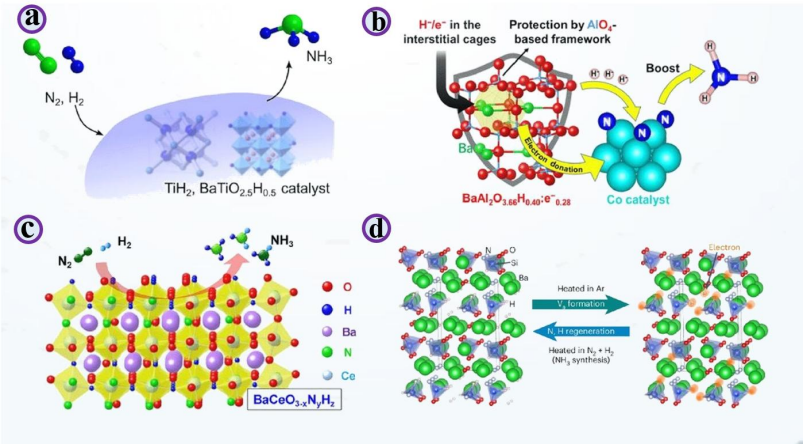

Figure 6. Schematics for catalytic ammonia synthesis over: **(a)** $BaTiO_{2.5}H_{0.5}$ [61]; **(b)** $BaAl_2O_{4-x}H_y$ [101]; **(c)** $BaCeO_{3-x}N_yH_z$ [67]; **(d)** $Ba_3SiO_{2.87}N_{0.80}H_{1.86}$ [102] and their supported catalysts.

The above oxyhydride or oxynitride-hydride catalysts all tend to have a transition metal site in their lattice structure or have the transition metal site on them as an active site, whereas in oxide materials containing no transition metal sites, there are very few effective catalysts. In the recent past, Kitano et al. have published a new orthosilicate oxynitride-hydride ($Ba_3SiO_{2.87}N_{0.80}H_{1.86}$) with ammonia synthesis capability through a catalytic reaction involving anion vacancy. The lattice can easily be desorbed to produce H^- and surface N_3^- anions under conditions of ammonia synthesis. The crystal has a great structural malleability, thus enabling it to produce and host a large number of electrons at anion vacancy sites. In the absence of any transition metal sites, these anion vacancies can directly activate N_2 molecules and generate ammonia in an associative hydrogenation reaction (**Figure 6d**).

3.5. Photo-driven ammonia synthesis using hydrides

The fact that solar energy is a renewable and plentiful resource has attracted a lot of interest among researchers in terms of artificial solar-driven chemical reactions and catalytic processes. Research has found that some alkali/alkaline earth metal hydrides are semiconducting [103,104]. It caused people to be immediately interested in studying the photon-hybrid interactions to trigger new chemical reactions [105]. Recently, Guan et al. found that LiH can be rapidly colored in the ultraviolet (UV) light as white turns to pale blue (**Figure 7a**) and that electron paramagnetic resonance (EPR) spectroscopy (**Figure 7b**) showed the occurrence of F-center defects (color centers) in the lattice of UV-irradiated LiH samples. The presence of this phenomenon suggests that LiH is dehydrogenated by UV radiation. Fourier-transform infrared spectroscopy

(FTIR) showed evidence of N-H stretching vibrations to be observed in samples of LiH when subjected to UV ray irradiation in the presence of N_2.

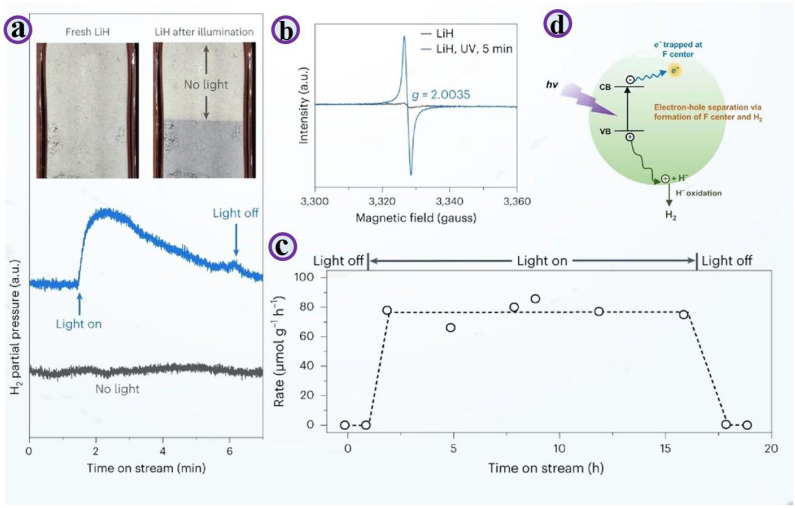

Figure 7. **(a)** Mass spectrometry of LiH with the presence or absence of UV light and the presence or absence of Ar at room temperature. Inset is the digital photographs of LiH under UV and no UV light, **(b)** LiH EPR spectra under illumination or no illumination. The rate is written as: **(c)** The rate of photocatalytic ammonia synthesis LiH during the UV irradiation; **(d)** Processing schemes of the charge carrier separation processes of the LiH photolysis process [106].

Follow-up measurements showed that introducing an N_2/H_2 feed with low H_2 content to LiH enables photocatalytic NH_3 formation under ambient-temperature illumination. Mechanistic analyses suggest that UV illumination generates electron–hole pairs; photogenerated holes oxidize H^- to form H_2, while electrons are trapped in long-lived color centers associated with hydrogen vacancies (**Figure 7d**). These trapped electrons facilitate N_2 activation and enable photo-switchable nitrogen conversion, allowing NH_3 formation without transition-metal catalysts. This work highlights hydrides as mediators for photocatalytic nitrogen fixation and suggests potential solar-driven routes for ammonia synthesis [106].

4. Chemical looping ammonia synthesis (CLAS)

4.1. Fundamental concepts and thermodynamics

Chemical looping ammonia synthesis (CLAS) separates NH_3 formation into sequential steps mediated by solid nitrogen carriers, reducing direct competition between N_2 and H_2 adsorption that constrains conventional single-surface catalysis. Depending on the hydrogen source, CLAS can operate as H_2O-CLAS (water as the hydrogen source) or H_2-CLAS (hydrogen gas). In H_2O-CLAS, metals first fix N_2 to form metal nitrides, which are then hydrolyzed to release NH_3 and form oxides that are subsequently reduced back to the metal. Thermodynamic analyses of hydride-based carriers indicate that nitrogen fixation to imide/nitride phases can be favorable over broad temperature windows (≈0–500 °C) for selected Li/Mg/Ca/Ba systems, while the corresponding hydrogenation steps are often endothermic and strongly dependent on carrier composition. These trends help identify hydride/imide pairs

that are both thermodynamically viable and potentially tunable for practical looping conditions [107–112].

4.2. Nitrogen carriers and advanced CLAS strategies

Experiments using LiH/Li_2NH and BaH_2/BaNH carrier pairs demonstrated CLAS at atmospheric pressure around 350 °C. Kinetic analysis indicated that nitrogen fixation has a substantially higher apparent activation barrier than the subsequent hydrogenation step, making carrier nitridation the rate-determining process in BaH_2/BaNH-mediated looping. Introducing transition metals (Fe, Co, Ni) markedly improved kinetics; Ni showed the strongest effect, reducing the apparent activation energy for nitrogen fixation (e.g., from ~109 to ~46 kJ mol^{-1} in Ni–BaH_2) and enabling measurable NH_3 formation at lower temperatures. Reported rates reached ~1533 and ~3125 μmol g^{-1} h^{-1} at 300 °C for Ni–LiH and Ni–BaH_2, respectively, and supporting Ni–BaH_2 on high-surface-area Al_2O_3 enabled NH_3 formation below 100 °C. Cycling tests also indicated multi-cycle operation, although phase segregation can contribute to activity decay shows in (**Figure 8a,b**).

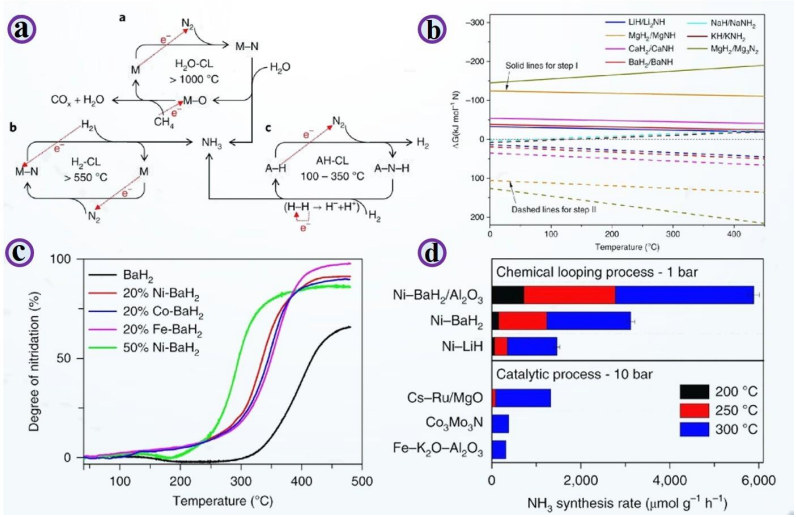

Figure 8. **(a)** A: H_2O-CL, B: H_2-CL, C: AH-CL (three different types of CLAS). Where M, A is metal and alkali/alkaline earth metal; **(b)** Thermodynamic investigations of processes I and II of AH-CL. TM catalyzed; **(c)** BaH_2 nitridation; **(d)** The rate of NH_3 in Ni-catalyzed AH-CL as compared to some of the active catalysts in the traditional thermocatalytic process [68].

More experiments demonstrated that ammonia production can be realized below 100 °C with the support of Ni-BaH_2 on the high-surface-area Al_2O_3. The Ni-BaH_2/Al_2O_3 CLAS performance in the ammonia synthesis reaction at 250 °C and 1 bar pressure was found to be an order of magnitude higher than the high-activity Cs-Ru/MgO catalyst under the same temperature and 10 bar pressure. And cycling tests were also performed on the Ni-BaH_2 sample, which showed that at least 10 cycles can be performed at 250 °C. The 10th cycle activity was nearly 80% of the original value. Additional studies found that the process of activity decay could be caused by phase segregation of Ni and BaH_2 following repeated cycles. Amazingly, re-ball milling the sample allowed restoring the activity to some extent shows in **Figure 8c,d** [68].

The CLAS process separates the ammonia synthesis into two or more consecutive stages through the use of nitrogen carriers [107]. This method is successful in overcoming the scaling relations of the single transition metal catalysts. CLAS does not require the competitive adsorption of N_2 and H_2 by step-wise feeding, as conventional catalytic methods of ammonia synthesis do. Also, the thermodynamics and the kinetics of each step may be optimized by adjusting the properties of the carriers of nitrogen [108]. A multifunctional composite nitrogen carrier was developed by Feng et al., which combined BaH_2/BaNH nitrogen carriers with the conventional nitride carriers (Mn_4N) (**Figure 9a**) [69]. Findings showed that Mn_4N not only catalyzes nitrogen fixation and ammonia release in the course of transformations of hydrogen and imides but also plays a secondary transport role in nitrogen through Mn_4N-Mn_2N conversion. This compound carrier pledged CLAS at 200–400 °C, where Mn_4N-BaH_2 gave a rate of ammonia synthesis of 3142 μmol g^{-1} h^{-1} at 300 °C, which was many times better than the performance of the individual carriers. Those outcomes of cycle stability indicate that the Mn_4N-BaH_2 performance is fundamentally stable after 6 complete cycles at 275 °C and atmospheric pressure. Moon et al. provide an in-situ neutron spectroscopy and diffraction analysis that is supported by first-principles simulations to examine the structural change throughout the nitridation and hydrogenation of Ni-BaH_2 [113]. They determined that ball-milling of the Ni-BaH_2 precursor triggers a dramatic reduction in the size of the BaH_2 particles and an increment of its defect density and potential elevation of its reactivity.

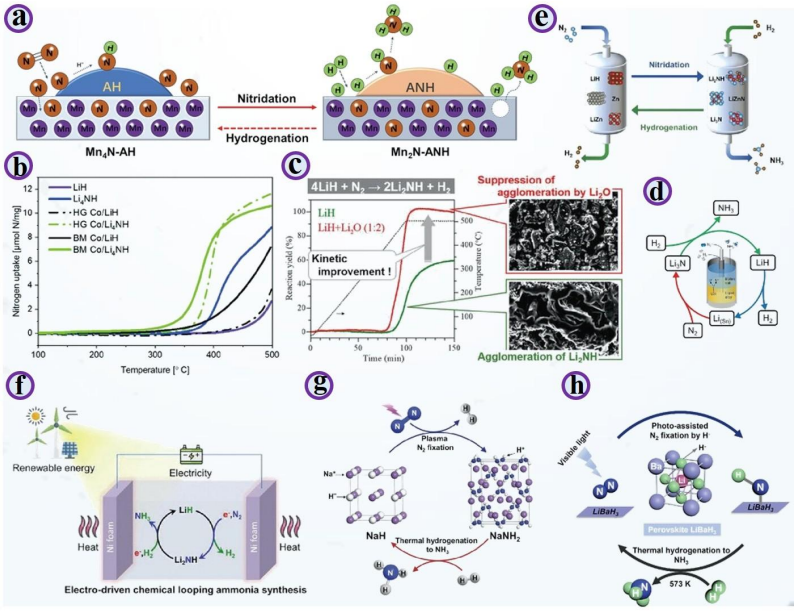

Figure 9. **(a)** The mediating scheme of CLAS with MnN_x-BaNH composite N carrier [69]; **(b)** N_2 -TPR of plain and cobalt-composite LiH and Li_4NH [114]; **(c)** The results of the LiH in the presence of Li_2O in the TG-MS reaction were compared with the results without Li_2O [114]; **(d)** CLAS: Molten LiCl-KCl eutectic molten Salt, Li-Sn alloy [115]; **(e)** Schematic diagram of the CLAS reaction mediated by ZnLiH-Li_2NH [116]; **(f)** Electro-directed CLAS reaction mediated by LiH/Li_2NH cycle Conceptual cycle [117]; **(g)** NaH/$NaNH_2$-mediated NaH/$NaNH_2$-mediated conceptual cycle of Plasma-driven CLAS [118]; **(h)** Photo-driven CLAS process mediated by $LiBaH_3$ Conceptual cycle [119].

The findings of inelastic neutron scattering and diffraction confirm the transformation of BaH_2 into BaNH when it reacts with N_2. In the hydrogenation, along with the recovery of the product of hydrogenation, a barium imide intermediate lacking nitrogen can be detected. It was found that hydrogenation is more difficult than the nitridation process compared to other catalysts, and this supports the preferential N_2 activation property of the Ni/BaH_2 catalyst. In the case of LiH, Yan et al. examined the impact of Pd on the CLAS mediated by LiH [120]. The LiH-Li_2NH reaction was modified by the formation of the tertiary Pd Li-Pd-H and Li-Pd alloys in the reaction, and the rate of the reaction was greatly accelerated. Makepeace et al. discovered that the compositions of Li-N-H over a wide range may be made through either solid-state synthesis or N_2 reaction [121]. LiH can be nitridated at 300–500 °C to form partially reduced imides of the general formula $Li_2 + {}_xNH$ ($0 \leq x \leq 2$), a solid solution of Li_2NH and Li_4NH [114]. The nitride-hydride (Li_4NH) reacts subsequently with N_2 by almost an order of magnitude faster than LiH under similar conditions to form imide and nitride phases (**Figure 9b**). Nevertheless, the mechanisms that regulate the transformation of LiH to $Li_2+{}_xNH$, and the theoretical ammonia yield when subjected to the hydrogenation process, are only poorly known. Ichikawa et al. found that Li_2O was ball-milled into LiH-Li_2NH, inhibiting reactant agglomeration to increase the kinetics of LiH in the fixation of nitrogen (**Figure 9c**) [122]. Tang et al. have created a lithium-based alloy cycle system of CLAS (**Figure 9d**) in which nitrogen reacts with a Li-Sn alloy at 510 °C to form Li_3N [115]. Li_3N is then dissolved in a LiCl-KCl eutectic salt, and then reacts with H_2 at 450 °C to produce LiH and generate NH_3. They were also able to determine that the formation of some intermediate species, like $LiNH_2$ or Li_2NH, was possible during the course of the reaction. According to Wang et al., Zn-LiH produced H_2 in the process of nitrogen fixing, which gave rise to many $LiZn_x$ intermetallic compounds and nitrogen-bearing species, including Li_2NH, Li_3N, and LiZnN (**Figure 9e**) [116]. In further hydrogenation, these species produced ammonia and returned to LiH, Zn, LiZn, and the CLAS cycle was concluded. Kinetic experiments demonstrated that Zn lowered the apparent activation energy of fixation of LiH nitrogen between 102 kJ mol^{-1} and 50 kJ mol^{-1}. Within 350 °C and atmospheric pressure, Zn-LiH generated ammonia 19 times faster than LiH, with a rate of 956 μmol g^{-1} h^{-1}.

The nitrogen fixation through hydrides is a process that is very different from the classic process of nitrogen activation on the transition metals. The study by Guan et al. aimed to examine the process of N_2 activation and transformation on BaH_2 by combining the theoretical and experimental methodologies [123]. Over the recent years, the use of electricity, light, plasma, etc., as external fields to drive CLAS processes has been studied by researchers, and significant progress has been made. Although CLAS catalyzed by the AH/ANH complexes may work at fairly mild conditions, at high temperatures, hydrogenation of ANH to ammonia is thermodynamically constrained. As an example, the concentration of ammonia in the equilibrium of the ANH hydrogenation process at 400 °C is just 626 ppm. In order to solve this problem, Feng et al. came up with an electro-driven LiH/Li_2NH-mediated H_2-CLAS process (**Figure 9f**) [117]. Hemodynamic studies showed that at room

temperature and pressure, as little as 0.05 V was required to raise the equilibrium concentration of ammonia in the course of Li_2NH hydrogenation between 0.19% and 8.5%. A voltage of 0.11 V at 400 °C and atmospheric pressure would increase the equilibrium concentration of ammonia to 27.1% further. This paper used molten salt electrolyte (LiCl-NaCl-KCl) to facilitate the two-step electrochemical reaction by electrical energy: nitridation of LiH and hydrogenation of Li_2NH. The experimental findings revealed that electrical energy contributed greatly to the hydrogenation of lithium imide as well as the fixation of nitrogen by lithium hydride; the apparent rate of the ammonia synthesis was increased by almost eight times relative to the thermochemical process. Moreover, such a technique theoretically provides better reaction thermodynamics than the existing Li^+-mediated electrochemical ammonia synthesis reactions and has been experimentally demonstrated to operate at low-voltage conditions (available currents up to 2.0 V). Wu et al. created a process of H_2-CLAS by a plasma-driven reaction between NaH (**Figure 9g**) [118]. As stated above, Guan et al. have found that lithium hydride (LiH) would mediate the process of photocatalytic ammonia production [69, 106]. These results indicate that external fields may have a major effect in enhancing the thermodynamic and kinetic performance of the CLAS process, resulting in ammonia production that is more efficient. Moreover, the combination of the external field-based processes with the storage and use of renewable energy may help develop the miniaturized and distributed ammonia production systems. Nevertheless, studies conducted by external fields to enhance CLAS are infrequent, and the mechanisms behind the beneficial effect are still unclear, posing tremendous opportunities in future research and advancements.

5. Thermocatalytic decomposition of ammonia

Over the past decade, substantial progress has been made in ammonia decomposition technologies aimed at producing high-purity, COx-free H_2 [19, 124–128]. Thermodynamically, NH_3 decomposition approaches near-complete equilibrium conversion at elevated temperatures (e.g., ~99% at 400 °C and ~99.7% at 500 °C), but residual NH_3 in the product stream can necessitate additional purification steps. Achieving scalable and energy-efficient cracking, therefore, depends on advances in three areas: highly active (preferably Ru-free) catalysts, efficient reactor designs, and integrated separation/purification strategies. Mechanistically, NH_3 decomposition proceeds through NH_3 adsorption, stepwise dehydrogenation to surface NHx species, and recombination/desorption of N_2 and H_2; catalyst choice strongly influences the rate-limiting steps and the operating temperature window [129–132].

This part discusses the kinetic and thermodynamic concepts of NH_3 breakdown on the basis of the appropriate examples explaining how various catalysts influence the process. Moreover, the NH_3 decomposition mechanisms, including the photodecomposition, electrochemical decomposition, and thermochemical decomposition, are also discussed in the article. The initial two have been briefly discussed, but the third one has been presented in detail, and a discussion about the kinetics, the processes involved in a reaction, the stability, and the catalytic efficiency has been presented. Further subsections address the purification of H_2 and the

separation processes involved in getting the N_2 out of the mixture of unreacted NH_3 and the generated H_2 [85] is shown in **Figure 10**.

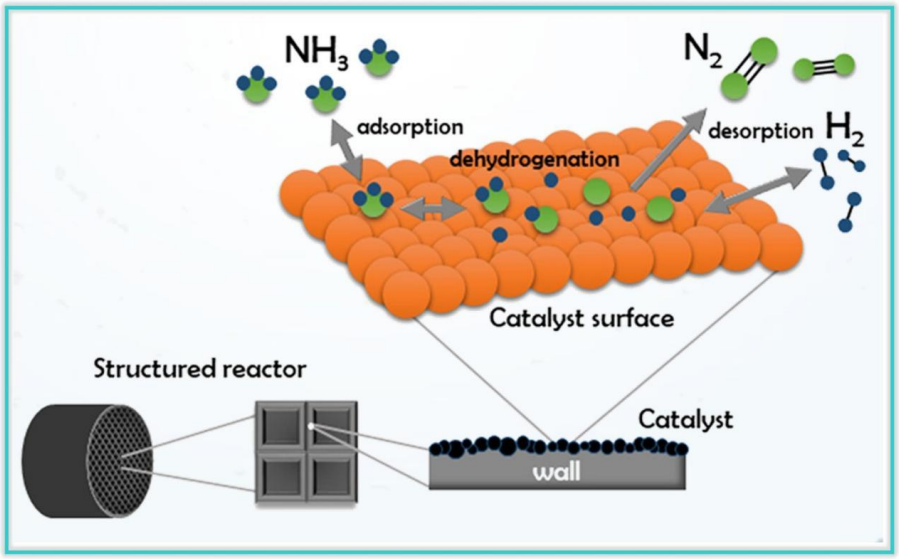

Figure 10. Decomposition of NH_3 into N_2 and H_2 via catalysis [133].

5.1. Amide- and imide-based catalysts

The breakdown of ammonia is also effective to produce green hydrogen, not contributing carbon because only nitrogen and hydrogen are emitted, which has attracted extensive interest. This reaction is thermodynamically preferred by the high temperatures (low pressures). Indicatively, when the temperature is at 400 °C, the conversion of ammonia can be at over 99% equilibrium (**Figure 11a**) [134]. The supported Ni-based catalysts in use today in industries demand temperatures over 700 °C to convert 99%. Thus, the creation of new and effective catalysts to decompose ammonia at moderate or low temperatures and the investigation of new processes will make the reaction temperatures and the use of energy even lower, allowing the mass production of ammonia decomposition technologies. The Sabatier principle indicates that the optimal catalyst to use in the decomposition of ammonia must possess an intermediate nitrogen adsorption energy. As in the case of ammonia synthesis catalysts, the activity of ammonia decomposition catalysts follows a volcano plot with respect to nitrogen dissociative adsorption energy (**Figure 11b**). Since Ru has a moderate energy of adsorption of nitrogen, it is positioned at the top of the curve and has the highest intrinsic activity. But the cost is high, and its availability is low, which limits its application; thus, the aim of finding alternative non-noble metal catalysts to Ru-based catalysts is a key area of concern in this sphere. Ammonia decomposition catalysts have been studied by researchers in great depth and volume within the past decades. The transition metals, alloys, metal nitrides, carbides, and sulfides are the major types of catalytic systems developed. The most promising have been group IX transition metals like Ru and Ni, and Mo or W nitride and carbide ammonia decomposers. Those who may want to learn more can use recent reviews on the same [135,136].

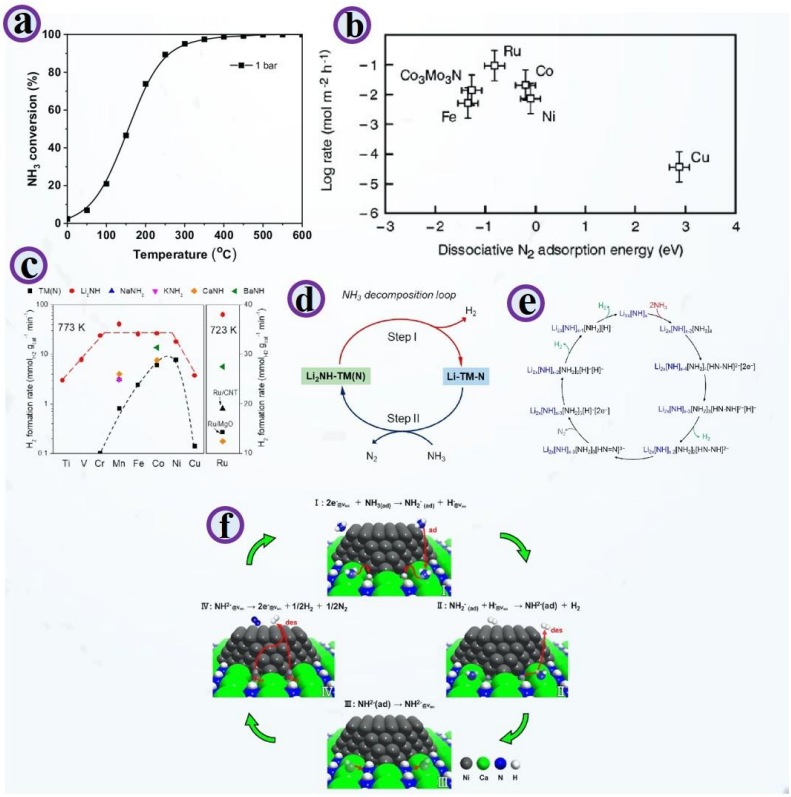

Figure 11. **(a)** At different temperatures, NH_3 was converted to equilibrium at 1 atm; **(b)** Experimental rate of ammonia decomposition with various catalysts as a function of reaction energy of dissociative N_2 adsorption [136]; **(c)** The decomposition rate of ammonia by selected transition metals in the presence of alkali/alkaline earth metals, amides/imides [90]; **(d)** Schematic representation of the mechanism of ammonia decomposition on TM-Li_2NH composite catalysts [90]; **(e)** The streamlined diagram of the catalytic ammonia decomposition process of Li_2NH [137]; **(f)** Schematic diagram explanation of the decomposition of ammonia on Ni/CaNH [81].

The possible use of alkali and alkaline earth metal imide compounds as hydrogen storage materials has influenced researchers to carry out thorough investigations of their structures, physicochemical characteristics, and chemical reactions [138]. Earlier on, in 1894, Tethered et al. found the degradation of ammonia to N_2 and H_2 when subjected to heated $NaNH_2$ that had attained a dark red color [139]. Chen et al. found in 2003 that $LiNH_2$ breaks down in the presence of temperatures higher than 400 °C, and releases gas-phase products that contained NH_3, N_2, and H_2 [140]. Scientists have thought that N_2 and H_2 could be a result of NH_3 decomposition, which is catalyzed by $LiNH_2$/Li_2NH. Using this finding, Guo et al. performed systematic and in-depth research on the alkali metal amides' participation in the ammonia decomposition. They discovered by extensive experimental validation that N_2 and H_2 do not directly result in catalytic decomposition of NH_3 by $LiNH_2$/Li_2NH but are closely associated with the stainless-steel reactor on which the test was conducted [141]. $LiNH_2$ decomposes at temperatures under 450 °C to produce mostly NH_3, the gaseous product in a quartz reactor. Within a stainless-steel reactor, however, it is possible to observe N_2 and H_2 signals below 300 °C of temperature, and $NaNH_2$ behaves in the same manner. This observation shows clearly that pure alkali metal amide or imide compounds have very

low levels of catalytic activity to decompose NH_3, and the presence of transition metals is important in catalyst imide/amide catalysis. At this time, David et al. had reported that $NaNH_2$ had a good exponential ammonia decomposition activity on stainless steel reactors [142].

The authors proposed the possibility of $NaNH_2$ as a new catalyst in ammonia decomposition, similar to the Ru-based catalysts. In 2015, Guo et al. synthesized a group of composite catalysts that incorporate Li_2NH and either transition metals or their nitrides (TM-Li_2NH) as the components [80]. **Figure 11c** demonstrates that the intrinsic activities of Ti, V, Cr, Mn, and Cu were low and had a volcano plot. Introduction of Li_2NH gave a big boost to the ammonia decomposition property of 3d transition metals, with Cr and Mn having their activity improved by 1 to 2 orders of magnitude, and Co and Ni, which are regarded as good catalysts in ammonia decomposition, improving activity by 2 to 3-fold. MnN-Li_2NH was the most active with a rate of Hydrogen permeation of 37.5 mmolH_2 $g_{cat}^{-1}min^{-1}$ at 500 °C, 40 times more active than MnN and similar to highly active Ru/CNTs [90,143]. In their paper on the alkali metal promoters in ammonia synthesis catalysts, Medford et al. theoretically showed that the introduction of promoters does not change the shape of the volcano curve [144]. In the TM(N)-Li2NH system, however, the activities of Li_2NH-promoted Cr, Mn, Fe, Co, and Ni catalysts were fairly close, and not like the volcano-shaped curve of pure 3d TM catalysts.

This observation indicates that the mechanism of decomposition of ammonia in this system is different from conventional ammonia decomposition by alkali metal-promotion of transition metals and their nitrides. According to the XRD, XAS, TPR, and the isotope experiment results, the authors have suggested a new two-step ammonia decomposition mechanism (**Figure 11d**). Firstly, Li_2NH is reacted with TM(N) to give ternary nitrides (LiTMN) and H_2. LiTMN, on the other hand, interacts with NH_3 to form Li_2NH and emits N_2 to form a complete catalytic cycle. In contrast to the conventional electronically promoted electronics, Li_2NH is an NH_3 transfer medium that allows the reaction to form transition metal nitride intermediates. In 2023, Yang et al. and Mambretti et al. made an ab initio molecular dynamics simulation (AIMD) discovery that shows that the dynamic surface structure variations of Li_2NH contribute to the catalytic ammonia decomposition behavior (**Figure 11e**) considerably [137,145]. In this situation, the surface composition and structure of Li_2NH are subjected to a sequence of dynamic processes that eventually cause the extraction of N_2 and H_2. Another point that is made in this research is the role of Li_2NH in ammonia breakdown as opposed to the orthodox role of alkali metals as electronic promoters. Besides the TM(N)-Li_2NH system, Guo et al. transferred these catalyst systems to other metals with alkali/alkaline earth metal amides/imides and prepared catalytic systems including Ru-$Ba(NH_2)_2$ [15], Mn_6N_5-CaNH [146], MnN-Li_2NH [147], Ni-$NaNH_2$ [148], and Ru-Li_2NH [149] with all of them showing excellent ammonia decomposition activity. Moreover, according to Kishida et al., the oblate-spherical Ru particles that are large and oblate in shape are efficient catalysts of the decomposition of ammonia in the presence of $Ca(NH_2)_2$ [150]. The characteristically increasing size of the particle of Ru resulted in a two-order increase in the TOF of Ru-Ca $(NH_2)_2$. The authors attributed

that being very active Ru-Ca $(NH_2)_2$, the shape and the optimal size of the particles of Ru, and the density of the active sites. Subsequently, they reported an effective ammonia decomposition reactor called Ni-CaNH catalyst that uses an NH_2^- vacancy based Mars-von Krevelen mechanism [81]. The ammonia decomposition activity of Ni-CaNH was found to have an operating temperature that is lower by 100 °C than in the reference Ni-based catalysts. The main locations of decomposition of ammonia, according to the results of the experimental and DFT calculations, are the VNH sites at the Ni-CaNH interface. To begin with, the VNH sites are created in the process of pretreatment. The addition of a 1:3 N_2/H_2 mixed gas stream leads to the oxidation of NH_2-species in the CaNH lattice to form N_2 and H_2 by the nickel catalyst, yielding VNH sites that have two anionic electrons in them. Next, the NH_3 breaks down at the VNH sites through a four-step reaction. In step I, the adsorption of NH_3 to the positively charged Ca^{2+} sites that surround the VNH sites and the reaction of the two anionic electron donors on the VNH sites to generate NH_2 anion and H anion take place. The reaction of the H-captured at the VNH site with a proton at the NH_2-site results in the production of H_2 and the generation of NH_2^-. In Step III, the formed NH_2^- fills in the VNH site. The NH_2^- lattice (IV) dissociates into N_2 and H_2 (step IV) and initiates the regeneration of the VNH sites at the Ni-CaNH interface (**Figure 11f**) [81]. These data indicate that NH_2^- vacancies on CaNH are highly significant in enhancing the reaction of decomposing ammonia. The above-discussed works and the findings provided evidence of a tremendous potential of alkali/alkaline earth metal amides and alkaline earth metal imides as catalysts in ammonia decomposition.

The thermodynamic properties of a catalytic reaction are crucial for the strategic development of catalysts with industrial relevance. The equation expresses the decomposition of NH_3 into H_2 and N_2:

$$2NH_3(g) \rightarrow N_2(g) + 3H_2(g),\ \Delta H = +46\ \text{kJ/mol}$$

Several theoretical works have reported on the relationship between temperature (250–700 °C) and the rate of NH_3 conversion (90–100%). Gibbs free energy is less, resulting in thermodynamic conversion of NH_3. The relationship between temperature and decomposition of NH_3 is not linear in the range of temperatures between 250–450 °C, yet the reaction rate does not considerably increase beyond 450 °C. Thus, in the high temperature regime, kinetic factors dominate the NH_3 breakdown. The awareness of these kinetic properties is pivotal in the establishment of effective catalytic devices, and how the process of breaking down takes place [151].

5.2. Hydride-mediated hydrogen production

Certain elements may form metal hydrides, particularly those in groups I–IV. These substances react readily with ammonia to produce a variety of amides/imides and nitrides. To create extensive amides, Bergstrom and Fernelius methodically compiled the reaction between an alkali metal and ammonia in 1933 [152]. The breakdown processes of these materials have been studied (**Table 2**), and SEM micrographs of the raw LiH **Figure 12a–d**. Kojima et al. have also examined the amides' capacity to be recycled. $LiNH_2$, $NaNH_2$, and KNH_2 spent 4, 4, and 2 h, respectively, in a hydrogen

flow environment (0.5 MPa). Then, samples were converted to LiH, NaH, and KH, respectively, in 96%, 100%, and 92% of cases [46,47,153]. Pure hydrogen can be made using the reaction between MH and NH_3 and later fed into a fuel cell once purified. Two hydrogen atoms in $LiNH_2$ are bound covalently to a nitrogen atom to produce the amide ion $[NH_2]^-$, which is in turn ionically bound to the Li-ion. As a result, the enthalpy of formation of $LiNH_2$ is less than that of ionic bonded hydrides, such as LiH; $LiNH_2$ breaks down at a relatively high temperature to yield the end product, Li_3N. The same trend can be noted with $NaNH_2$. Interestingly, both thermodynamic and kinetic considerations show that decomposition of the $Mg(NH_2)_2$ and $Ca(NH_2)_2$ is less stable when compared to that of $LiNH_2$. Thus, the electronegativity of the metal cation and the anion of the amide may affect the decomposition properties of the respective amide. Typically, Mg is more electronegative than Li or Na, and thus the ionic bond formed between Mg^{2+} and $[NH_2]^-$ is weaker than between Li^+ and $[NH_2]^-$, which explains the faster formation at the cost of the higher temperature decomposition observed with $LiNH_2$ than with other amides studied in this work. In addition, it was established that these metal hydrides are the ones that react with ammonia more easily, with a lower electronegativity of the metal cation. On the other hand, ammonia can be released more effectively by the formation of metal amides with cations possessing a greater value of the electronegativity [142].

Table 2. Metal Amide Synthesis by Ball Milling Reaction between Metal Hydrides and Gaseous NH_3.

Reaction	Time (h)	NH_3 pressure (MPa)	Decomposition temp (°C)
$LiH + NH_3 \rightleftharpoons LiNH_2 + H_2$	2	0.4	230–500
$NaH + NH_3 \rightleftharpoons NaNH_2 + H_2$	1	-	240–500
$KH + NH_3 \rightleftharpoons KNH_2 + H_2$	1	-	500–600
$MgH_2 + 2NH_3 \rightleftharpoons Mg(NH_2)_2 + 2H_2$	13	-	180–500
$CaH_2 + 2NH_3 \rightleftharpoons Ca(NH_2)_2 + 2H_2$	8	-	70–500

The design of a LiH-NH_3 hydrogen storage system with improved kinetic characteristics included a comprehensive investigation of the hydrogen desorption properties for reactions between lithium hydride with various particle sizes and NH_3 (0.5 MPa, NH_3/MH 1mol/mol) at 50–200 °C. Additionally, various potassium compounds were investigated as possible catalysts to enhance the system's hydrogen desorption reaction's kinetic characteristics. It is discovered that as the reaction temperature rises or the particle size of LiH decreases, the kinetic characteristics of the hydrogen desorption in the LiH-NH_3 system improve. **Figure 11** presents the hydrogen generation patterns of an hour at varying temperatures of raw LiH, ball-milled LiH, and KBr-enhanced LiH with NH_3 (0.5 MPa, NH_3/LiH = 1 mol/mol). The time-dependent hydrogen generation profiles for reactions carried out at 100 °C are offered in an inset of the figure. To improve the kinetic characteristics, KBr, KCl, KF, and KOH are useful; KBr has the most impact [49]. The hydrolysis-type reaction is exothermic; interestingly, the hydrogen desorption process may occur at ambient temperature. It has been shown that the response that recycles the by-product $LiNH_2$ back into LiH and NH_3 occurs at 300 °C when the partial pressure of NH_3 is lowered

under a 0.5 MPa flow of H_2 [46]. Ammonia must be converted to hydrogen at an average temperature in order for it to function as a hydrogen carrier. As a result, using what is already known, systems incorporating NH_3 and metal hydrides (MeH, where Me = Li, Na, K, Mg, and Ca) have been designed for this purpose. The reaction is formulated as follows [154, 155]. Moreover, several potassium-based substances were considered as possible catalysts, the goal of which was to increase the kinetic characteristics of the hydrogen desorption reaction of the system. The results were that the higher the temperature of the reaction or the size of the particles of LiH, the better the kinetic characteristics of desorption of hydrogen in the system LiH-NH_3. The compounds identified as most effective in enhancing these kinetic properties are KBr, KCl, KF, and KOH.

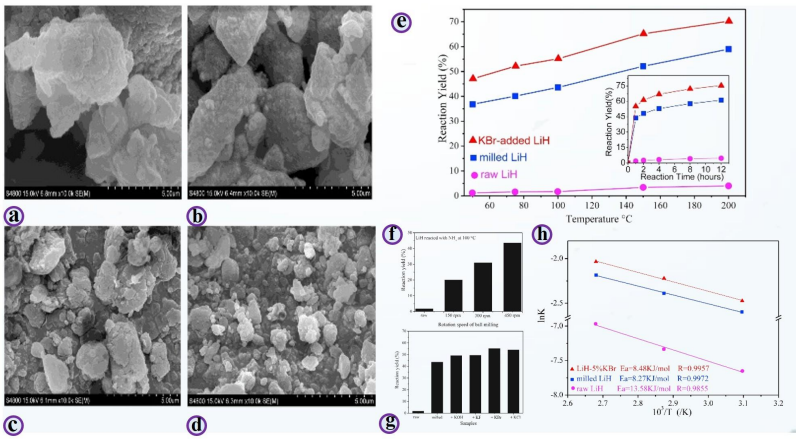

Figure 12. Hydrogen generation profile of the reaction of the raw LiH, ball-milled LiH, and the reaction of KBr-added LiH with NH_3: **(a–d)** SEM micrographs of the unprocessed LiH; **(e)** Percentage of reaction yield and the LiH ball-milled under rotation rates of 150 rpm, 300 rpm, and 450 rpm of 2 h; **(f–g)** Reaction yield on reactions between the raw LiH and the LiH ball-milled at various rotation speeds in the presence of NH_3 (0.5 MPa, NH_3/LiH = 1 mol/mol) at 100 °C with 1 h reaction time; **(h)** Arrhenius plot of the kinetic constant of the raw, ball-milled and KBr-added LiH at the measurement temperatures of 50, 75, 100, 150 and 200 °C [49].

$$MH + NH_3 \rightarrow MNH_2 + H_2 (M = Li, K, \text{and } Na) \quad (1)$$

5.3. Amide- and chemical looping–mediated hydrogen production

NH_3 suppression using various metal hydride additions. These systems, which have great volumetric and gravimetric hydrogen densities, are currently under investigation as materials to store hydrogen, such as LiNH, CaNH, Li/MgNH, and NaNH [138, 153, 156, 157]. This method is a significant difference from the previous surface catalytic practice since it involves the stoichiometric reduction and recovery of sodium amide ($NaNH_2$) through sodium metal. The Na/$NaNH_2$ system using 0.5 g of $NaNH_2$ and 60 sccm of NH_3 at 530 °C gives a 99.2% decomposition efficiency, which is favorable compared to other nickel and ruthenium-based catalysts in NH3 decomposition studies, which used a basic flow reactor. The development of $NaNH_2$-based ammonia cracking devices might increase the usage of NH_3 as a sustainable energy storage medium since it is an inexpensive and easily available substance. Sodium amide acts as a very effective catalyst for the stoichiometric

breakdown of ammonia, generating $NaNH_2$ from sodium metal. With an eye on sustainable energy applications, this technique departs from traditional transition metal catalysis by presenting a new class of amide-based materials for hydrogen extraction from ammonia. At different temperatures, the $NaNH_2$ decomposition efficiency of the supported ruthenium catalyst is shown in **Figure 13a**, which performs better at higher conversion levels [142]. Transition metals are the main catalysts for low-temperature NH_3 cracking; ruthenium has the best catalytic efficiency.

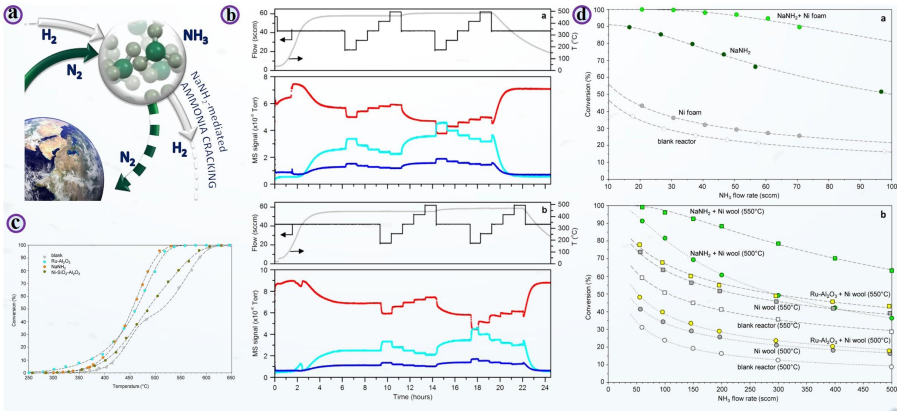

Figure 13. **(a)** Ammonia decomposition mechanism; **(b)** Results of the mass spectrometry of NH_3 (17, red), H_2 (2, cyan), and N_2 (28, blue) of the reaction of 0.25 g of $NaNH_2$ and 0.15 g of Na. The rates of temperature (light gray) and the flow rate of NH_3 (dark gray) in the course of the experiment at atmospheric pressure are shown in the upper pane of a given reaction; **(c)** Comparison of the NH_3 conversion; **(d)** Impact of containment methods and conversions obtained at different SCCM flow [142].

When the metal is incorporated with promoter species into complex support structures, its efficiency is significantly enhanced [158–161]. For the continuous stoichiometric breakdown of NH_3, sodium amide works equally well as a supported ruthenium catalyst, but at a far cheaper cost of materials. Given its reasonable cost and excellent efficiency, the Na/$NaNH_2$ system may constitute a novel class of NH_3 decomposition catalysts. Because of this potential, NH_3 decomposition should be given a second look as a practical hydrogen delivery technique for various purposes, including large-scale grid balancing, transportation, and distributed power production [162]. The mass spectrometry traces 0.25 g of NH_3 (red, m/z = 17), H_2 (cyan, m/z = 2), and N_2 (blue, m/z = 28) of the reaction of 0.25 g of $NaNH_2$ and 0.15 g of Na (**Figure 13b**). The temperature (light gray) and rate of flow of NH_3 (dark gray) in the course of the experiment at atmospheric pressure are shown in the upper panels of each reaction. Effects of containment techniques. conversion time (**Figure 13c**) time to obtain conversion of 0.5 g of $NaNH_2$ at 475 °C under a flow of 0.2 and 100 sccm in a reactor with a height of 1.6 mm and 1.141 cm^3. The reference data of blank reactor, Ni foam (only), and 0.5 g of $NaNH_2$ (only) are presented. Conversion at higher flows (50–500 sccm) of NH_3, in a 21.3 cm^3 reactor, of 0.5 g of $NaNH_2$ (green symbols), at 0.500 °C (solid circles) and 0.600 °C (solid squares) in the presence of 2 g nickel wool (**Figure 13d**). It is shown that the (i) alumina-supported ruthenium (2 g of nickel wool) (yellow symbols), (ii) 2 g of nickel wool (only) (gray symbols), and (iii) blank reactor data (open symbols) may be used as a reference.

The CLADH concept proceeds in two coupled steps. First, metallic Na (or K) reacts with NH_3 to form $NaNH_2$ (or KNH_2) while releasing one-third of the hydrogen. Second, the amide decomposes to regenerate the alkali metal with concomitant N_2 and H_2 formation, completing the loop. Thermodynamic analysis indicates that the ammoniation reactions are feasible below ~342 °C (Na) and ~301 °C (K), whereas amide decomposition to regenerate Na/K becomes favorable above ~275 °C ($NaNH_2$) and ~252 °C (KNH_2) under relevant gas atmospheres. Moreover, at sufficiently high temperatures, the Gibbs free energy for amide decomposition can be more favorable than direct NH_3 decomposition, suggesting a stronger driving force for hydrogen generation via the looping route. Experimental characterization (e.g., XRD/FTIR before and after reaction) supports room-temperature ammoniation to form amides and high-temperature amide decomposition to regenerate the metals. Adding MnN accelerates both stages, increasing hydrogen production rates by more than an order of magnitude relative to the pure amides under comparable conditions, as shown in **Figure 14a–d**.

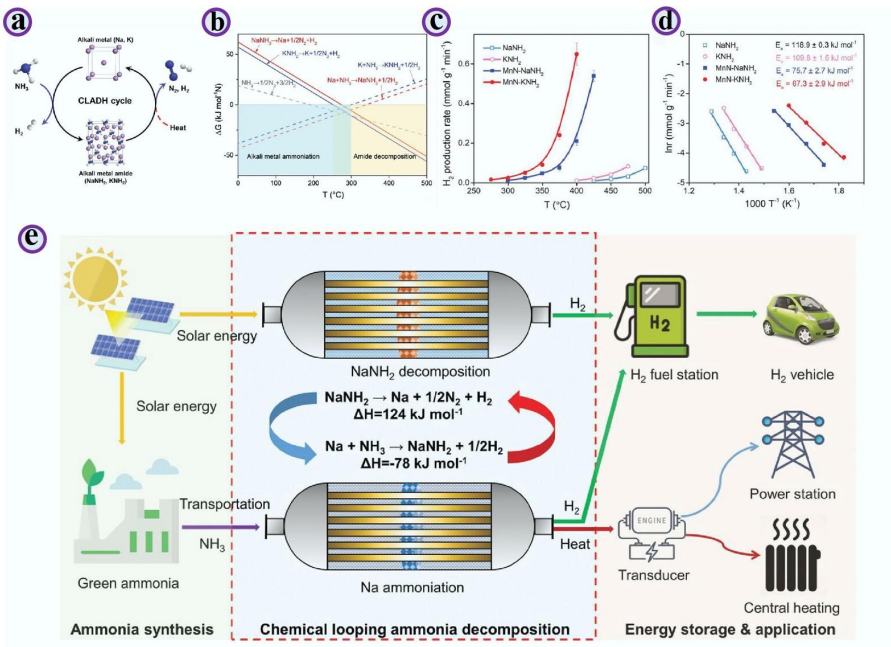

Figure 14. **(a)** Schematic scheme of CLADH with the use of alkali metals and all the corresponding pairs of alkali metals and amides; **(b)** Thermodynamics of CLADH. The solid curves are the temperature dependence of Gibbs free energy **(a–g)** of the degradation of $NaNH_2$ and KNH_2; **(c–d)** Temperature dependence of hydrogen production rates of CLADH [22]; The Arrhenius plot of the temperature-dependent rate of hydrogen production over $NaNH_2$ and KNH_2 with or without MnN; **(e)** CLADH process on the production of hydrogen and the storage of solar energy [163].

With MnN addition, hydrogen production was observed at temperatures as low as ~275–300 °C, consistent with a large decrease in apparent activation energy. At 400 °C, MnN–KNH_2 produced H_2 at ~0.65 mmol g^{-1} min^{-1} (≈59 × faster than KNH_2), and at 425 °C MnN–$NaNH_2$ reached ~0.54 mmol g^{-1} min^{-1} (≈54 × faster than $NaNH_2$). The apparent activation energies decreased to ~67.3 and ~75.7 kJ mol^{-1} for KNH_2 and $NaNH_2$, respectively, indicating a strong MnN–amide synergy. Under optimized

CLADH conditions, near-complete amide conversion was achieved (≈99% for KNH_2 at 400 °C and ≈98% for $NaNH_2$ at 425 °C). By contrast, when MnN–amide materials are evaluated under conventional thermal catalytic NH_3 decomposition conditions (i.e., without operating the full looping sequence), much lower net conversion is observed (reported as ~7% and ~13%), highlighting that the high performance is specific to the looping pathway, as shown in **Figure 14e** [22,163,164].

6. Conclusion

Alkali and alkaline-earth metal hydrides, amides, and imides have emerged as a versatile materials family for ammonia synthesis and decomposition, not merely as inert supports or promoters but as dynamic participants that store, transfer, and activate hydrogen and nitrogen. Across the studies reviewed here, a common theme is that these materials enable reaction pathways that differ from classical transition-metal surface chemistry: lattice hydride and interfacial hydride/electron transfer can facilitate heterolytic H_2 activation, stabilize reactive NxHy intermediates, and, in favourable cases, relax scaling constraints that limit metal-only catalysts. These features underpin advances in thermocatalytic ammonia synthesis using hydride/oxyhydride/complex hydride phases, photo-assisted routes in which hydrides generate long-lived charge carriers that promote nitrogen conversion, and chemical-looping schemes that separate nitrogen fixation and hydrogenation to reduce competitive adsorption and tune thermodynamic driving forces. For ammonia decomposition, amide/imide chemistry and looping-type concepts offer promising routes to COx-free hydrogen, with the additional advantage that operating modes can be designed to manage equilibrium limitations and mitigate residual NH_3 when paired with suitable purification strategies.

Despite clear progress, several barriers must be addressed to translate hydride/amide/imide-enabled chemistry into practical, scalable technologies. First, many of these materials are highly sensitive to air and moisture, and their long-term stability under realistic feeds (including trace contaminants) and repeated thermal cycling remains insufficiently understood. Second, performance often depends on evolving multiphase microstructures and interfaces (e.g., metal–hydride contacts, nitride/amide gradients, segregating promoters), yet these dynamic features are rarely controlled deliberately, leading to variability in activity and deactivation through sintering, phase separation, volatilization of carriers, or loss of active interfacial area. Third, while chemical-looping approaches demonstrate compelling thermodynamic and kinetic advantages, overall process efficiency will hinge on integrating fast solid-state transport, rapid gas–solid reaction steps, and energy-efficient heat management at scale. Finally, mechanistic interpretations are frequently inferred from ex situ characterization; robust operando evidence is still limited for key steps such as N_2 activation sites, hydride migration pathways, and the identity of dominant NxHy intermediates under working conditions.

Future research should therefore prioritize four directions. (1) Stabilize materials and interfaces: develop protective architectures (core–shells, passivation layers that remain permeable to $H_2/N_2/NH_3$), compositional tuning to suppress volatility, and supports/porous scaffolds that preserve interfacial contact and resist sintering. (2)

Mechanism-resolved design: combine isotopic labeling with operando spectroscopy and diffraction (e.g., in situ XRD/neutron methods, XAS, DRIFTS/IR, solid-state NMR where feasible) to quantify hydride and nitrogen mobility, identify rate-limiting steps, and distinguish true catalytic cycles from stoichiometric conversion. (3) Rational promotion and microstructure control: move beyond empirical promoter selection by mapping how alkali/alkaline-earth species, transition metals, and defects (vacancies, colour centres, oxyhydride composition) control electron/hydride transfer and adsorption energetics; design catalysts where the active phase and the active interface are engineered reproducibly. (4) Process and reactor integration: for thermocatalysis, couple catalysts to intensified reactors and downstream purification tailored to ultra-low residual NH_3; for photo-assisted routes, improve light harvesting and charge utilization while quantifying solar-to-chemical efficiencies; for chemical looping, optimize cycle scheduling, particle engineering, and heat integration, and evaluate system-level metrics (energy efficiency, durability, safety, and cost) against incumbent Haber–Bosch and conventional cracking.

Overall, hydride/amide/imide chemistry provides a powerful framework for rethinking ammonia as both a product and an energy vector. Continued progress will require aligning fundamental mechanistic insight with materials stabilization and process engineering so that the most promising laboratory demonstrations evolve into robust, efficient, and scalable platforms for low-carbon ammonia production and COx-free hydrogen delivery.

Author contributions: MAA, SH, and IUK conceived the idea, MAA and SH collected data, and wrote the first draft. IUK carried out data analysis and revised the manuscript. The whole project was administrated and supervised by the IUK. All authors have read and agreed to the published version of the manuscript.

Funding: This work received no external funding.

Institutional review board statement: Not applicable.

Informed consent statement: Not applicable.

Data availability statement: Not applicable.

Conflict of interest: The authors declare no conflict of interest.

References

1. Matthews HD, Wynes S. Current global efforts are insufficient to limit warming to 1.5 °C. Science. 2022; 376(6600): 1404–1409.
2. Aslam MA, Mustaqeem M, Abbas MS, et al. Hydrogen Revolution: Advances in Catalytic Ammonia Decomposition. Clean Energy Technologies. 2025; 1(1): 49–69.
3. Møller KT, Jensen TR, Akiba E, et al. Hydrogen-A sustainable energy carrier. Progress in Natural Science: Materials International. 2017; 27(1): 34–40.
4. He T, Pachfule P, Wu H, et al. Hydrogen carriers. Nature Reviews Materials. 2016; 1(12): 1–17.
5. Cha J, Park Y, Brigljević B, et al. An efficient process for sustainable and scalable hydrogen production from green ammonia. Renewable and Sustainable Energy Reviews. 2021; 152: 111562.
6. Aslam MA, Abbas MS, Irfan RM, et al. From ammonia to hydrogen: Evolution of ruthenium-based catalysts. ACS

Catalysis. 2025; 15(21): 18631–18662.
7. Liu M, Yao Z, Gu J, et al. Issues and opportunities facing hydrolytic hydrogen production materials. Chemical Engineering Journal. 2023; 461: 141918.
8. Dotan H, Landman A, Sheehan SW, et al. Decoupled hydrogen and oxygen evolution by a two-step electrochemical–chemical cycle for efficient overall water splitting. Nature Energy. 2019; 4(9): 786–795.
9. Hodges A, Hoang AL, Tsekouras G, et al. A high-performance capillary-fed electrolysis cell promises more cost-competitive renewable hydrogen. Nature Communications. 2022; 13(1): 1304.
10. Hauch A, Küngas R, Blennow P, et al. Recent advances in solid oxide cell technology for electrolysis. Science. 2020; 370(6513): eaba6118.
11. Clark D, Malerød-Fjeld H, Budd M, et al. Single-step hydrogen production from NH_3, CH_4, and biogas in stacked proton ceramic reactors. Science. 2022; 376(6591): 390–393.
12. Simagina VI, Vernikovskaya NV, Komova OV, et al. Experimental and modeling study of ammonia borane-based hydrogen storage systems. Chemical Engineering Journal. 2017; 329: 156–164.
13. Sørensen RZ, Hummelshøj JS, Klerke A, et al. Indirect, reversible high-density hydrogen storage in compact metal ammine salts. Journal of the American Chemical Society. 2008; 130(27): 8660–8668.
14. Humphries TD, Sheppard DA, Buckley CE. Recent advances in the 18-electron complex transition metal hydrides of Ni, Fe, Co and Ru. Coordination Chemistry Reviews. 2017; 342: 19–33.
15. Yu P, Guo J, Liu L, et al. Effects of alkaline earth metal amides on Ru in catalytic ammonia decomposition. The Journal of Physical Chemistry C. 2016; 120(5): 2822–2828.
16. Wang P, Chang F, Gao W, et al. Breaking scaling relations to achieve low-temperature ammonia synthesis through LiH-mediated nitrogen transfer and hydrogenation. Nature Chemistry. 2017; 9(1): 64–70.
17. Chang F, Tezsevin I, de Rijk JW, et al. Potassium hydride-intercalated graphite as an efficient heterogeneous catalyst for ammonia synthesis. Nature Catalysis. 2022; 5(3): 222–230.
18. Yin S, Xu B, Zhou X, et al. A mini-review on ammonia decomposition catalysts for on-site generation of hydrogen for fuel cell applications. Applied Catalysis A: General. 2004; 277(1–2): 1–9.
19. Schüth F, Palkovits R, Schlögl R, et al. Ammonia as a possible element in an energy infrastructure: catalysts for ammonia decomposition. Energy & Environmental Science. 2012; 5(4): 6278–6289.
20. Wan Z, Tao Y, Shao J, et al. Ammonia as an effective hydrogen carrier and a clean fuel for solid oxide fuel cells. Energy Conversion and Management. 2021; 228: 113729.
21. Le TA, Do QC, Kim Y, et al. A review on the recent developments of ruthenium and nickel catalysts for CO x-free H_2 generation by ammonia decomposition. Korean Journal of Chemical Engineering. 2021; 38(6): 1087–1103.
22. Feng S, Gao W, Guo J, et al. Progress of metal hydrides, amides and imides for ammonia synthesis and decomposition. The Innovation Energy. 2025; 100122-1–100122-18.
23. MacFarlane DR, Cherepanov PV, Choi J, et al. A roadmap to the ammonia economy. Joule. 2020; 4(6): 1186–1205.
24. Morlanés N, Katikaneni SP, Paglieri SN, et al. A technological roadmap to the ammonia energy economy: Current state and missing technologies. Chemical Engineering Journal. 2021; 408: 127310.
25. Mukherjee S, Devaguptapu SV, Sviripa A, et al. Low-temperature ammonia decomposition catalysts for hydrogen generation. Applied Catalysis B: Environmental. 2018; 226: 162–181.
26. Fang H, Wu S, Ayvali T, et al. Disperced surface Ru ensembles on MgO (111) for catalytic ammonia decomposition. Nature Communications. 2023; 14(1): 647.
27. Tabassum H, Mukherjee S, Chen J, et al. Hydrogen generation via ammonia decomposition on highly efficient and stable Ru-free catalysts: approaching complete conversion at 450 °C. Energy & Environmental Science. 2022; 15(10): 4190–4200.
28. Xie P, Yao Y, Huang Z, et al. Highly efficient decomposition of ammonia using high-entropy alloy catalysts. Nature Communications. 2019; 10(1): 4011.
29. Fang H, Liu D, Luo Y, et al. Challenges and opportunities of Ru-based catalysts toward the synthesis and utilization of ammonia. ACS Catalysis. 2022; 12(7): 3938–3954.
30. Cerrillo JL, Morlanés N, Kulkarni SR, et al. High purity, self-sustained, pressurized hydrogen production from ammonia in a catalytic membrane reactor. Chemical Engineering Journal. 2022; 431: 134310.
31. Maleki H, Fulton M, Bertola V. Kinetic assessment of H_2 production from NH_3 decomposition over CoCeAlO catalyst in a microreactor: Experiments and CFD modelling. Chemical Engineering Journal. 2021; 411: 128595.
32. Lee J, Ga S, Lim D, et al. Carbon-free green hydrogen production process with induction heating-based ammonia decomposition reactor. Chemical Engineering Journal. 2023; 457: 141203.

33. Brunauer S, Love KS, Keenan RG. Adsorption of nitrogen and the mechanism of ammonia decomposition over iron catalysts. Journal of the American Chemical Society. 1942; 64(4): 751–758.
34. Novell-Leruth G, Valcárcel A, Pérez-Ramírez J, et al. Ammonia dehydrogenation over platinum-group metal surfaces. Structure, stability, and reactivity of adsorbed NH_x species. The Journal of Physical Chemistry C. 2007; 111(2): 860–868.
35. Lorenzut B, Montini T, Pavel CC, et al. Embedded Ru@ZrO_2 catalysts for H_2 production by ammonia decomposition. ChemCatChem. 2010; 2(9): 1096–1106.
36. Niu L, Liu X, Zhou X, et al. Genesis of an Fe_5C_2@Fe_3O_4 core/shell structure during CO carburization of metallic iron nanoparticles. Journal of Catalysis. 2022; 407: 97–103.
37. Wang L, Zhao Y, Liu C, et al. Plasma driven ammonia decomposition on a Fe-catalyst: eliminating surface nitrogen poisoning. Chemical Communications. 2013; 49(36): 3787–3789.
38. Okura K, Okanishi T, Muroyama H, et al. Ammonia decomposition over nickel catalysts supported on rare-earth oxides for the on-site generation of hydrogen. ChemCatChem. 2016; 8(18): 2988–2995.
39. Im Y, Muroyama H, Matsui T, et al. Ammonia decomposition over nickel catalysts supported on alkaline earth metal aluminate for H_2 production. International Journal of Hydrogen Energy. 2020; 45(51): 26979–26988.
40. Duan X, Ji J, Yan X, et al. Understanding Co-Mo catalyzed ammonia decomposition: influence of calcination atmosphere and identification of active phase. ChemCatChem. 2016; 8(5): 938–945.
41. Podila S, Driss H, Zaman SF, et al. MgFe and Mg–Co–Fe mixed oxides derived from hydrotalcites: highly efficient catalysts for CO_x free hydrogen production from NH_3. International Journal of Hydrogen Energy. 2020; 45(1): 873–890.
42. Leybo DV, Baiguzhina AN, Muratov DS, et al. Effects of composition and production route on structure and catalytic activity for ammonia decomposition reaction of ternary Ni–Mo nitride catalysts. International Journal of Hydrogen Energy. 2016; 41(6): 3854–3860.
43. Zamfirescu C, Dincer I. Using ammonia as a sustainable fuel. Journal of Power Sources. 2008; 185(1): 459–465.
44. Klerke A, Christensen CH, Nørskov JK, et al. Ammonia for hydrogen storage: challenges and opportunities. Journal of Materials Chemistry. 2008; 18(20): 2304–2310.
45. Miyaoka H, Ichikawa T, Hino S, et al. Compressed hydrogen production via reaction between liquid ammonia and alkali metal hydride. International Journal of Hydrogen Energy. 2011; 36(14): 8217–8220.
46. Kojima Y, Tange K, Hino S, et al. Molecular hydrogen carrier with activated nanohydride and ammonia. Journal of Materials Research. 2009; 24: 2185–2190.
47. Yamamoto H, Miyaoka H, Hino S, et al. Recyclable hydrogen storage system composed of ammonia and alkali metal hydride. International Journal of Hydrogen Energy. 2009; 34(24): 9760–9764.
48. Hino S, Ogita N, Udagawa M. Thermodynamic properties of lithium amide under hydrogen pressure determined by Raman spectroscopy. Journal of Applied Physics. 2009; 105(2): 023521.
49. Dong BX, Song L, Teng YL, et al. Enhanced hydrogen desorption reaction kinetics by optimizing the reaction conditions and doping potassium compounds in the LiH–NH_3 system. International Journal of Hydrogen Energy. 2014; 39(25): 13838–13843.
50. Kitano M, Inoue Y, Yamazaki Y, et al. Ammonia synthesis using a stable electride as an electron donor and reversible hydrogen store. Nature Chemistry. 2012; 4(11): 934–940.
51. Kitano M, Inoue Y, Ishikawa H, et al. Essential role of hydride ion in ruthenium-based ammonia synthesis catalysts. Chemical Science. 2016; 7(7): 4036–4043.
52. Abe H, Niwa Y, Kitano M, et al. Anchoring bond between Ru and N atoms of Ru/Ca_2NH catalyst: crucial for the high ammonia synthesis activity. The Journal of Physical Chemistry C. 2017; 121(38): 20900–20904.
53. Gong Y, Wu J, Kitano M, et al. Ternary intermetallic LaCoSi as a catalyst for N_2 activation. Nature Catalysis. 2018; 1(3): 178–185.
54. Li J, Wu J, Wang H, et al. Acid-durable electride with layered ruthenium for ammonia synthesis: boosting the activity via selective etching. Chemical Science. 2019; 10(22): 5712–5718.
55. Ye TN, Park SW, Lu Y, et al. Vacancy-enabled N_2 activation for ammonia synthesis on an Ni-loaded catalyst. Nature. 2020; 583(7816): 391–395.
56. Ye TN, Lu Y, Kobayashi Y, et al. Efficient ammonia synthesis over phase-separated nickel-based intermetallic catalysts. The Journal of Physical Chemistry C. 2020; 124(52): 28589–28595.
57. Zhang K, Cao A, Wandall LH, et al. Spin-mediated promotion of Co catalysts for ammonia synthesis. Science. 2024; 383(6689): 1357–1363.

58. Yiliguma, Park SW, Li J, et al. C_2 vacancy-mediated N_2 activation over Ni-loaded rare-earth dicarbides for ammonia synthesis. ACS Catalysis. 2021; 11(12): 7595–7603.
59. Wang Q, Guan Y, Guo J, et al. Hydrides mediate nitrogen fixation. Cell Reports Physical Science. 2022; 3(3): 100796.
60. Chang F, Guan Y, Chang X, et al. Alkali and alkaline earth hydrides-driven N2 activation and transformation over Mn nitride catalyst. Journal of the American Chemical Society. 2018; 140(44): 14799–14806.
61. Kobayashi Y, Tang Y, Kageyama T, et al. Titanium-based hydrides as heterogeneous catalysts for ammonia synthesis. Journal of the American Chemical Society. 2017; 139(50): 18240–18246.
62. Wang Q, Pan J, Guo J, et al. Ternary ruthenium complex hydrides for ammonia synthesis via the associative mechanism. Nature Catalysis. 2021; 4(11): 959–967.
63. Yamashita H, Broux T, Kobayashi Y, et al. Chemical pressure-induced anion order–disorder transition in LnHO enabled by hydride size flexibility. Journal of the American Chemical Society. 2018; 140(36): 11170–11173.
64. Zhang X, Liu L, Wu A, et al. Synergizing surface hydride species and Ru clusters on Sm_2O_3 for efficient ammonia synthesis. ACS Catalysis. 2022; 12(4): 2178–2190.
65. Mao C, Wang J, Zou Y, et al. Hydrogen spillover to oxygen vacancy of TiO_2–xH_y/Fe: breaking the scaling relationship of ammonia synthesis. Journal of the American Chemical Society. 2020; 142(41): 17403–17412.
66. Guan Y, Zhang W, Wang Q, et al. Barium chromium nitride-hydride for ammonia synthesis. Chem Catalysis. 2021; 1(5): 1042–1054.
67. Kitano M, Kujirai J, Ogasawara K, et al. Low-temperature synthesis of perovskite oxynitride-hydrides as ammonia synthesis catalysts. Journal of the American Chemical Society. 2019; 141(51): 20344–20353.
68. Gao W, Guo J, Wang P, et al. Production of ammonia via a chemical looping process based on metal imides as nitrogen carriers. Nature Energy. 2018; 3(12): 1067–1075.
69. Feng S, Gao W, Wang Q, et al. A multi-functional composite nitrogen carrier for ammonia production via a chemical looping route. Journal of Materials Chemistry A. 2021; 9(2): 1039–1047.
70. Deng QF, Zhang H, Hou XX, et al. High-surface-area $Ce_{0.8}Zr_{0.2}O_2$ solid solutions supported Ni catalysts for ammonia decomposition to hydrogen. International Journal of Hydrogen Energy. 2012; 37(21): 15901–15907.
71. Huang C, Yu Y, Tang X, et al. Hydrogen generation by ammonia decomposition over Co/CeO2 catalyst: Influence of support morphologies. Applied Surface Science. 2020; 532: 147335.
72. Nagaoka K, Eboshi T, Abe N, et al. Influence of basic dopants on the activity of Ru/Pr_6O_{11} for hydrogen production by ammonia decomposition. International Journal of Hydrogen Energy. 2014; 39(35): 20731–20735.
73. Okura K, Okanishi T, Muroyama H, et al. Promotion effect of rare-earth elements on the catalytic decomposition of ammonia over Ni/Al_2O_3 catalyst. Applied Catalysis A: General. 2015; 505: 77–85.
74. Lu AH, Nitz JJ, Comotti M, et al. Spatially and size selective synthesis of Fe-based nanoparticles on ordered mesoporous supports as highly active and stable catalysts for ammonia decomposition. Journal of the American Chemical Society. 2010; 132(40): 14152–14162.
75. Simonsen SB, Chakraborty C, Chorkendorff I, et al. Alloyed Ni-Fe nanoparticles as catalysts for NH_3 decomposition. Applied Catalysis A: General. 2012; 447: 22–31.
76. Zhang J, Müller JO, Zheng W, et al. Individual Fe−Co alloy nanoparticles on carbon nanotubes: structural and catalytic properties. Nano Letters. 2008; 8(9): 2738–2743.
77. Duan X, Qian G, Zhou X, et al. MCM-41 supported CoMo bimetallic catalysts for enhanced hydrogen production by ammonia decomposition. Chemical Engineering Journal. 2012; 207: 103–108.
78. Choi JG. Ammonia decomposition over vanadium carbide catalysts. Journal of Catalysis. 1999; 182(1): 104–116.
79. Zheng W, Cotter TP, Kaghazchi P, et al. Experimental and theoretical investigation of molybdenum carbide and nitride as catalysts for ammonia decomposition. Journal of the American Chemical Society. 2013; 135(9): 3458–3464.
80. Guo J, Wang P, Wu G, et al. Lithium imide synergy with 3d transition-metal nitrides leading to unprecedented catalytic activities for ammonia decomposition. Angewandte Chemie. 2015; 127(10): 2993–2997.
81. Ogasawara K, Nakao T, Kishida K, et al. Ammonia decomposition over CaNH-supported Ni catalysts via an NH_2–vacancy-mediated Mars–van Krevelen mechanism. ACS Catalysis. 2021; 11(17): 11005–11015.
82. Chen C, Wu K, Ren H, et al. Ru-based catalysts for ammonia decomposition: a mini-review. Energy & Fuels. 2021; 35(15): 11693–11706.
83. Afonso RV, Gouveia JD, Gomes JR. Catalytic reactions for H_2 production on multimetallic surfaces: a review. Journal of Physics: Energy. 2021; 3(3): 032016.
84. Hirscher M, Yartys VA, Baricco M, et al. Materials for hydrogen-based energy storage–past, recent progress and future outlook. Journal of Alloys and Compounds. 2020; 827: 153548.

85. García-Bordejé E, Armenise S, Roldán L. Toward practical application of H_2 generation from ammonia decomposition guided by rational catalyst design. Catalysis Reviews. 2014; 56(2): 220–237.
86. Hosono H, Kitano M. Advances in materials and applications of inorganic electrides. Chemical Reviews. 2021; 121(5): 3121–3185.
87. Hosono H. Field-assisted green ammonia synthesis. Science Bulletin. 2024; 69(1): 7–8.
88. Aika K, Christiansen LJ, Dybkjaer I, et al. Ammonia: Catalysis and Manufacture. Springer; 2011.
89. Cao H, Guo J, Chand F, et al. Transition and alkali metal complex ternary amides for ammonia synthesis and decomposition. Chemistry—A European Journal. 2017; 23(41): 9766–9771.
90. Guo J, Chen P. Interplay of alkali, transition metals, nitrogen, and hydrogen in ammonia synthesis and decomposition reactions. Accounts of Chemical Research. 2021; 54(10): 2434–2444.
91. Gao W, Wang P, Guo J, et al. Barium hydride-mediated nitrogen transfer and hydrogenation for ammonia synthesis: a case study of cobalt. ACS Catalysis. 2017; 7(5): 3654–3661.
92. Wang P, Xie H, Guo J, et al. The formation of surface lithium–iron ternary hydride and its function on catalytic ammonia synthesis at low temperatures. Angewandte Chemie. 2017; 129(30): 8842–8846.
93. Luo Z, Castleman AW, Khanna SN. Reactivity of metal clusters. Chemical Reviews. 2016; 116(23): 14456–14492.
94. Cui C, Jia Y, Zhang H, et al. Plasma-Assisted Chain Reactions of Rh_3^+ Clusters with Dinitrogen: N≡ N Bond Dissociation. The Journal of Physical Chemistry Letters. 2020; 11(19): 8222–8230.
95. Saitoh H, Takagi S, Matsuo M, et al. Li_4FeH_6: Iron-containing complex hydride with high gravimetric hydrogen density. APL Materials. 2014; 2(7): 076103.
96. Yvon K, Renaudin G. Hydrides: solid state transition metal complexes. In: Encyclopedia of Inorganic Chemistry. Wiley; 2006.
97. Wang Q, Pan J, Guo J, et al. Ternary ruthenium complex hydrides for ammonia synthesis. ChemRxiv preprint. 2020. doi: 10.26434/chemrxiv.13465760.v1
98. Strongin D, Carrazza J, Bare SR, et al. The importance of C_7 sites and surface roughness in the ammonia synthesis reaction over iron. Journal of Catalysis. 1987; 103(1): 213–215.
99. Dahl S, Logadottir A, Egeberg RC, et al. Role of steps in N_2 activation on Ru (0001). Physical Review Letters. 1999; 83(9): 1814–1817.
100. Fukui K, Iimura S, Iskandarov A, et al. Room-temperature fast H–conduction in oxygen-substituted lanthanum hydride. Journal of the American Chemical Society. 2022; 144(4): 1523–1527.
101. Jiang Y, Takashima R, Nakao T, et al. Boosted Activity of Cobalt Catalysts for Ammonia Synthesis with $BaAl_2O_{4-x}H_y$ Electrides. Journal of the American Chemical Society. 2023; 145(19): 10669–10680.
102. Zhang Z, Miyashita K, Wu T, et al. Anion vacancies activate N_2 to ammonia on Ba–Si orthosilicate oxynitride-hydride. Nature Chemistry. 2025: 1–9.
103. Doyle W, Ingram D, Smith M. Detection of colloidal centers in lithium hydride by electron resonance. Physical Review Letters. 1959; 2(12): 497.
104. Cornelius S, Colombi G, Nafezarefi F, et al. Oxyhydride nature of rare-earth-based photochromic thin films. The Journal of Physical Chemistry Letters. 2019; 10(6): 1342–1348.
105. Cheng Z, Guan Y, Wen H, et al. Light-driven de/rehydrogenation of a LiH surface under ambient conditions. The Journal of Physical Chemistry Letters. 2024; 15(25): 6662–6667.
106. Guan Y, Wen H, Cui K, et al. Light-driven ammonia synthesis under mild conditions using lithium hydride. Nature Chemistry. 2024; 16(3): 373–379.
107. Feng S, Gao W, Cao H, et al. Advances in the chemical looping ammonia synthesis. Acta Chimica Sinica. 2020; 78(9): 916.
108. Zhang X, Pei C, Zhao ZJ, et al. Towards green and efficient chemical looping ammonia synthesis: design principles and advanced redox catalysts. Energy & Environmental Science. 2024; 17(7): 2381–2405.
109. Gálvez M, Halmann M, Steinfeld A. Ammonia production via a two-step Al_2O_3/AlN thermochemical cycle. 1. Thermodynamic, environmental, and economic analyses. Industrial & Engineering Chemistry Research. 2007; 46(7): 2042–2046.
110. Michalsky R, Pfromm PH. Chromium as reactant for solar thermochemical synthesis of ammonia from steam, nitrogen, and biomass at atmospheric pressure. Solar Energy. 2011; 85(11): 2642–2654.
111. Michalsky R, Pfromm PH. Thermodynamics of metal reactants for ammonia synthesis from steam, nitrogen and biomass at atmospheric pressure. AIChE Journal. 2012; 58(10): 3203–3213.
112. Michalsky R, Steinfeld A. Computational screening of perovskite redox materials for solar thermochemical ammonia

synthesis from N_2 and H_2O. Catalysis Today. 2017; 286: 124–130.
113. Moon J, Cheng Y, Daemen LL, et al. On the structural transformation of Ni/BaH_2 during a N_2-H_2 chemical looping process for ammonia synthesis: a joint in situ inelastic neutron scattering and first-principles simulation study. Topics in Catalysis. 2021; 64(9): 685–692.
114. Ravi M, Makepeace JW. Lithium–nitrogen–hydrogen systems for ammonia synthesis: exploring a more efficient pathway using lithium nitride–hydride. Chemical Communications. 2022; 58(41): 6076–6079.
115. Tang Z, Meng X, Shi Y, et al. Lithium-based loop for ambient-pressure ammonia synthesis in a liquid alloy-salt catalytic system. ChemSusChem. 2021; 14(21): 4697–4707.
116. Wang R, Gao W, Feng S, et al. Zn Promotes chemical looping ammonia synthesis mediated by LiH−Li_2NH couple. ChemSusChem. 2023; 16(22): e202300813.
117. Feng S, Gao W, Guo, J, et al. Electrodriven chemical looping ammonia synthesis mediated by lithium imide. ACS Energy Letters. 2023; 8(3): 1567–1574.
118. Wu H, Yang L, Wen J, et al. Plasma-driven nitrogen fixation on sodium hydride. Advanced Energy Materials. 2023; 13(27): 2300722.
119. Cui K, Guan Y, Cai Y, et al. Perovskite LiBaH3 for photo-assisted dinitrogen fixation. Science China Chemistry. 2025; 68(3): 1169–1174.
120. Yan H, Gao W, Wang Q, et al. Lithium palladium hydride promotes chemical looping ammonia synthesis mediated by lithium imide and hydride. The Journal of Physical Chemistry C. 2021; 125(12): 6716–6722.
121. Makepeace JW, Brittain JM, Manghnani AS, et al. Compositional flexibility in Li–N–H materials: implications for ammonia catalysis and hydrogen storage. Physical Chemistry Chemical Physics. 2021; 23(28): 15091–15100.
122. Tagawa K, Gi H, Shinzato K, et al. Improvement of kinetics of ammonia synthesis at ambient pressure by the chemical looping process of lithium hydride. The Journal of Physical Chemistry C. 2022; 126(5): 2403–2409.
123. Guan Y, Liu C, Wang Q, et al. Transition-metal-free barium hydride mediates dinitrogen fixation and ammonia synthesis. Angewandte Chemie International Edition. 2022; 61(39): e202205805.
124. Lim D, Kim A, Cheon S, et al. Life cycle techno-economic and carbon footprint analysis of H_2 production via NH_3 decomposition: A Case study for the Republic of Korea. Energy Conversion and Management. 2021; 250: 114881.
125. Jiao F, Xu B. Electrochemical ammonia synthesis and ammonia fuel cells. Advanced Materials. 2019; 31(31): 1805173.
126. Ramalingam S, DhakshinaMoorthy M, Subramanian S. Effect of natural antioxidant additive on hydrogen-enriched biodiesel operated compression ignition engine. International Journal of Hydrogen Energy. 2022; 47(48): 20771–20783.
127. Giddey S, Badwal S, Kulkarni A. Review of electrochemical ammonia production technologies and materials. International Journal of Hydrogen Energy. 2013; 38(34): 14576–14594.
128. Bell TE, Torrente-Murciano L. H_2 production via ammonia decomposition using non-noble metal catalysts: A review. Topics in Catalysis. 2016; 59: 1438–1457.
129. Cechetto V, Di Felice L, Medrano JA, et al. H_2 production via ammonia decomposition in a catalytic membrane reactor. Fuel Processing Technology. 2021; 216: 106772.
130. Pashchenko D, Mustafin R. Ammonia decomposition in the thermochemical waste-heat recuperation systems: A view from low and high heating value. Energy Conversion and Management. 2022; 251: 114959.
131. Ju X, Liu L, Yu P, et al. Mesoporous Ru/MgO prepared by a deposition-precipitation method as highly active catalyst for producing CO_x-free hydrogen from ammonia decomposition. Applied Catalysis B: Environmental. 2017; 211: 167–175.
132. Wang S, Yin S, Li L, et al. Investigation on modification of Ru/CNTs catalyst for the generation of CO_x-free hydrogen from ammonia. Applied Catalysis B: Environmental. 2004; 52(4): 287–299.
133. Moszczyńska J, Liu X, Wiśniewski M. Green hydrogen production through ammonia decomposition using non-thermal plasma. International Journal of Molecular Sciences. 2023; 24(18): 14397.
134. Lucentini I, Garcia X, Vendrell X, et al. Review of the decomposition of ammonia to generate hydrogen. Industrial & Engineering Chemistry Research. 2021; 60(51): 18560–18611.
135. Verschoor JC, de Jongh PE, Ngene P. Recent advances in thermocatalytic ammonia synthesis and decomposition. Current Opinion in Green and Sustainable Chemistry. 2024; 50: 100965.
136. Turaeva N, Fushimi R, Yablonsky G. Kinetic expression for optimal catalyst electronic configuration: The case of ammonia decomposition. The Journal of Physical Chemistry C. 2020; 124(48): 26310–26319.
137. Yang M, Raucci U, Parrinello M. Reactant-induced dynamics of lithium imide surfaces during the ammonia

decomposition process. Nature Catalysis. 2023; 6(9): 829–836.
138. Chen P, Zhu M. Recent progress in hydrogen storage. Materials Today. 2008; 11(12): 36–43.
139. Titherley AW. XLV.—Sodium, potassium, and lithium amides. Journal of the Chemical Society, Transactions. 1894; 65: 504–522.
140. Chen P, Xiong Z, Luo J, et al. Interaction between lithium amide and lithium hydride. The Journal of Physical Chemistry B. 2003; 107(39): 10967–10970.
141. Gao W, Guo J, Chen P. Hydrides, amides and imides mediated ammonia synthesis and decomposition. Chinese Journal of Chemistry. 2019; 37(5): 442–451.
142. David WI, Makepeace JW, Callear SK, et al. Hydrogen production from ammonia using sodium amide. Journal of the American Chemical Society. 2014; 136(38): 13082–13085.
143. Guo J, Chang F, Wang P, et al. Highly Active MnN–Li_2NH Composite Catalyst for Producing COx-Free Hydrogen. ACS Catalysis. 2015; 5(5): 2708–2713.
144. Medford AJ, Vojvodic A, Hummelshøj JS, et al. From the Sabatier principle to a predictive theory of transition-metal heterogeneous catalysis. Journal of Catalysis. 2015; 328: 36–42.
145. Mambretti F, Raucci U, Yang M, et al. How does structural disorder impact heterogeneous catalysts? The case of ammonia decomposition on non-stoichiometric lithium imide. ACS Catalysis. 2024; 14(3): 1252–1256.
146. Yu P, Guo J, Liu L, et al. Ammonia decomposition with manganese nitride–calcium imide composites as efficient catalysts. ChemSusChem. 2016; 9(4): 364–369.
147. Chang F, Guo J, Wu G, et al. Influence of alkali metal amides on the catalytic activity of manganese nitride for ammonia decomposition. Catalysis Today. 2017; 286: 141–146.
148. Chang F, Wu H, van der Pluijm R, et al. Effect of pore confinement of $NaNH_2$ and KNH_2 on hydrogen generation from ammonia. The Journal of Physical Chemistry C. 2019; 123(35): 21487–21496.
149. Guo J, Chen Z, Wu A, et al. Electronic promoter or reacting species? The role of $LiNH_2$ on Ru in catalyzing NH3 decomposition. Chemical Communications. 2015; 51(82): 15161–15164.
150. Kishida K, Kitano M, Inoue Y, et al. Large oblate hemispheroidal ruthenium particles supported on calcium amide as efficient catalysts for ammonia decomposition. Chemistry—A European Journal. 2018; 24(31): 7976–7984.
151. Chiuta S, Everson RC, Neomagus HW, et al. Reactor technology options for distributed hydrogen generation via ammonia decomposition: A review. International Journal of Hydrogen Energy. 2013; 38(35): 14968–14991.
152. Bergstrom F, Fernelius WC. The Chemistry of the Alkali Amides. Chemical Reviews. 1933; 12(1): 43–179.
153. Kojima Y, Miyaoka H, Ichikawa T. Hydrogen Storage Materials. In: New and Future Developments in Catalysis. Elsevier; 2013. pp. 99–136.
154. Leng H, Ichikawa T, Hino S, et al. Synthesis and decomposition reactions of metal amides in metal–N–H hydrogen storage system. Journal of Power Sources. 2006; 156(2): 166–170.
155. Leng H, Ichikawa T, Isobe S, et al. Desorption behaviours from metal–N–H systems synthesized by ball milling. Journal of Alloys and Compounds. 2005; 404: 443–447.
156. Zhang T, Isobe S, Wang Y, et al. A solid–solid reaction enhanced by an inhomogeneous catalyst in the (de) hydrogenation of a lithium–hydrogen–nitrogen system. RSC Advances. 2013; 3(18): 6311–6314.
157. Sudik A, Yang J, Halliday D, et al. Kinetic improvement in the Mg $(NH_2)_2$− LiH storage system by product seeding. The Journal of Physical Chemistry C. 2007; 111(17): 6568–6573.
158. Yin SF, Xu BQ, Wang SJ, et al. Magnesia–carbon nanotubes (MgO–CNTs) nanocomposite: Novel support of Ru catalyst for the generation of CO x-free hydrogen from ammonia. Catalysis Letters. 2004; 96: 113–116.
159. Raróg-Pilecka W, Szmigiel D, Kowalczyk Z, et al. Ammonia decomposition over the carbon-based ruthenium catalyst promoted with barium or cesium. Journal of Catalysis. 2003; 218(2): 465–469.
160. Sørensen RZ, Nielsen LJE, Jensen S, et al. Catalytic ammonia decomposition: miniaturized production of COx-free hydrogen for fuel cells. Catalysis Communications. 2005; 6(3): 229–232.
161. Klerke A, Klitgaard SK, Fehrmann R. Catalytic ammonia decomposition over ruthenium nanoparticles supported on nano-titanates. Catalysis Letters. 2009; 130: 541–546.
162. Hull S, Smith RI, David WI, et al. The Polaris powder diffractometer at ISIS. Physica B: Condensed Matter. 1992; 180: 1000–1002.
163. Dong X, Zhu S, Li H. Recent research progress of catalysts for thermocatalytic ammonia decomposition. International Journal of Hydrogen Energy. 2025; 143: 286–306.
164. Feng S, Gao W, Wang R, et al. Chemical looping ammonia decomposition mediated by alkali metal and amide pairs for H_2 production and thermal energy storage. Advanced Energy Materials. 2024; 14(43): 2401252.

Energy Storage and Conversion 2025, 3(4), 3842.
doi: https://doi.org/10.59400/esc3842

Review

Effect of different pretreatments and their parameters on biogas production performance: A review

Himan Khodkam

Department of Biosystem Engineering, Faculty of Agricultural and Natural Resources, University of Mohaghegh Ardabili, Ardabil P.O.Box 178, Iran; h.khodkam@uma.ac.ir

CITATION

Khodkam H. Effect of different pretreatments and their parameters on biogas production performance: A review. Energy Storage and Conversion. 2025; 3(4): 3842. https://doi.org/10.59400/esc3842

ARTICLE INFO

Received: 11 September 2025
Revised: 14 November 2025
Accepted: 16 November 2025
Available online: 10 December 2025

Abstract: Energy supply is fundamental to modern society, yet its current reliance on fossil fuels is a major contributor to global warming. A transition to renewable energy is therefore critical, offering both climate mitigation and economic opportunities. Biogas is a particularly effective renewable source, addressing energy needs and waste management simultaneously by converting organic matter into clean fuel. Production occurs through a four-stage anaerobic digestion process, influenced by parameters such as temperature, pH, C/N ratio, retention time, mixing, and moisture. Pretreatment methods can significantly enhance efficiency and yield. For lignocellulosic materials, sodium hydroxide is a common chemical choice, while biological pretreatment offers a low-energy alternative. Among additives, zero-valent iron nanoparticles have shown considerable promise. This article aims to identify optimal conditions to make biogas production more cost-effective. Synthesized studies indicate that maximum biogas yield is achieved by: reducing feedstock particle size, maintaining an inlet concentration near 8%, applying a ratio of 25, ensuring neutral pH, and operating at mesophilic temperatures. A key finding is that pretreatment effectiveness is not universal; it is highly dependent on the specific feedstock and digestion conditions. In conclusion, biogas exemplifies the potential of renewables to create a more sustainable and resilient energy system. By optimizing its production, we can advance toward a greener future that reduces environmental impact while supporting economic growth.

Keywords: energy crisis; biogas; pre-treatment; optimal state; production; nanoparticles; anaerobic digestion

1. Introduction

The main cause of the energy crisis in society is the need to change the pattern of energy consumption and strive for sustainability. Despite the increasing energy demand, fossil fuel resources are depleting, and they currently account for approximately 85% of the world's primary energy consumption [1]. Fuel consumption occurs at a much faster rate than the time it takes for production and replenishment, leading to a rapid depletion of resources. Moreover, the use of these fuels results in the release of greenhouse gases, the most significant impact of which is the rising global temperature, posing a threat to human well-being. The consequences of this temperature increase can be multiple and devastating, necessitating society to take action to mitigate the upward trend.

With the growing human impact on the environment and the advancement of societal structures, waste management has become a crucial consideration. Inefficient

waste disposal practices can result in unpleasant odors, pose risks to human health, and contribute to surface and groundwater pollution [2]. While there are various methods available for waste disposal, the most effective approach is to transform this challenge into an opportunity, aligning with the primary development policy in many countries. Anaerobic digestion (AD) has emerged as the most favorable and efficient method for waste management and addressing global warming concerns [3]. Considering its economic, environmental, and social benefits, anaerobic digestion stands out as the most promising solution [4]. Anaerobic digestion has significant potential due to its ability to utilize a wide range of resources and its minimal carbon emissions during the production process [5]. The process of anaerobic digestion can generate various forms of energy, including heat, electricity, and transportation fuel, utilizing renewable sources [6]. In general, biomass resources can be categorized into five main groups (**Figure 1**) [7]:

- Urban solid waste;
- Animal waste;
- Agricultural waste;
- Urban sewage;
- Industrial waste.

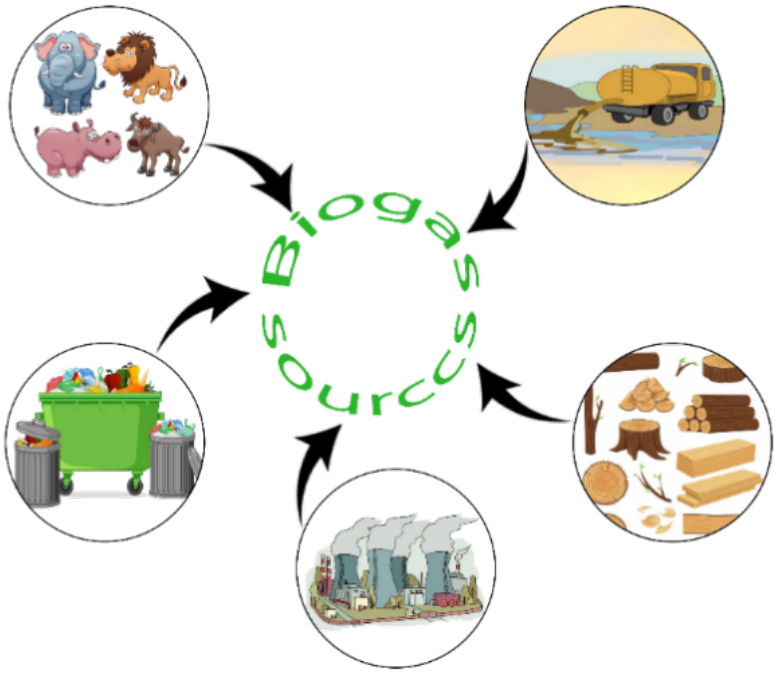

Figure 1. Biomass sources for biogas production.

The biogas industry has its unique characteristics in different parts of the world due to the availability of primary resources. Switzerland and Sweden primarily obtain a significant portion of biogas through the decomposition of wastewater. On the other hand, Denmark, Germany, and Great Britain utilize more food waste due to the abundance and accessibility of animal manure [8]. Lignocellulosic materials serve as one of the most valuable sources of organic materials for biogas production. These materials are widely available in agricultural and industrial wastes and represent a renewable resource that is more cost-effective compared to other organic materials.

Agricultural biomass undergoes a short time lag, resulting in a low biogas yield. To enhance its productivity and efficiency, pre-treatment is necessary before subjecting it to anaerobic digestion [9]. The digestion of cellulose in biomass is mainly hindered by factors such as the presence of lignin, cellulose crystallinity, and particle size [10].

To enhance the absorption of carbohydrates in lignocellulosic biomass during fermentation processes, it is crucial to decrease the rigidity of the cell fiber, leading to the breakdown of lignin and the hydrolysis of cellulose and hemicellulose. This ultimately results in the conversion of these components into polysaccharides and monomers. Consequently, pretreatments involving physical, chemical, or biological methods may be required to facilitate the hydrolysis of lignocellulosic constituents [11].

However, there is no consensus on the most appropriate type of pretreatment for lignocellulosic waste applications, as their effects may vary depending on the source [12]. The rate of biogas production is influenced by various factors including the type of pretreatment utilized, operating conditions, bed type, and AD parameters [13]. Other factors such as reactor type, feed material composition, concentration, temperature, pH, C/N ratio, residence time, stirring, and moisture percentage also impact the biogas yield [14]. The objective is to achieve the optimal biogas production rate while considering the aforementioned factors. The production cost of biogas can be reduced and made more economical by increasing the amount of biogas generated. Optimization techniques can lead to a 57% increase in biogas performance [15]. Therefore, it is essential to search for the ideal conditions and the best pretreatment methods to achieve the maximum yield of biogas.

2. Biogas

Biogas is the gas generated during the anaerobic digestion of biomass waste, including animal waste, plant residues, sewage, urban and human solid waste, industrial waste, and agricultural waste [16]. The anaerobic digestion process involves four stages in which different bacteria interact with each other [17]. These stages include hydrolysis, acidogenesis, acetogenesis, and methanogenesis. First step: To harness the energy contained within biomass, it is necessary to first convert long molecular chains into smaller units or monomers that can be easily decomposed by bacteria. This process, known as hydrolysis, involves breaking down these chains and dissolving smaller molecules in a solution. Hydrolysis plays a crucial role in anaerobic digestion as it is the initial step in converting complex organic molecules into simple sugars, amino acids, and fatty acids [18].

The second stage involves the biological process of acidogenesis, which leads to the further decomposition of the remaining components through the activity of acid-producing bacteria. During this stage, certain components from the previous stage, such as acetate and hydrogen, can be directly utilized by methanogens. However, there are also volatile fatty acids (VFAs) with longer chain lengths than acetate, which require conversion into compounds that are directly usable by methanogens. The acidification stage exhibits a rich microbial diversity. During the process of hydrolysis, a majority of the bacteria involved also contribute to acidification. Additional bacteria from the genera Enterobacterium, Streptococcus, and Eubacterium are also involved in the

acidification process [19]. It is important to maintain a pH level above six during acidification to optimize the conversion process [20].

Third stage: During the steatogenesis phase (stratigraphy), the steatogenic bacteria interact with newly formed compounds, resulting in the production of acetic acid, carbon dioxide, and hydrogen. Microbial species such as Clostridium, Syntrophus, Syntrophomonas, and Syntro-bacteria have been found to contribute to the osteogenesis process [19]. Fourth stage: In the methanogenesis stage, methanogens utilise the by-products generated from the preceding stages (acetic acid, carbon dioxide, and hydrogen) and convert them into methane, carbon dioxide, and water [17]. Methanogenesis is sensitive to pH levels, with optimal conditions occurring between 6 and 8.5. This process involves two distinct groups of bacteria: hydrogenotrophic bacteria, which facilitate the anaerobic oxidation of hydrogen, and acetoclastic bacteria, which facilitate the anaerobic conversion of acetic acid, resulting in the production of methane and carbon dioxide [21]. The synergistic interaction between the acidogenic bacteria and methanogens renders the entire biogas production process thermodynamically efficient [22]. **Figure 2** illustrates the four stages of biogas production.

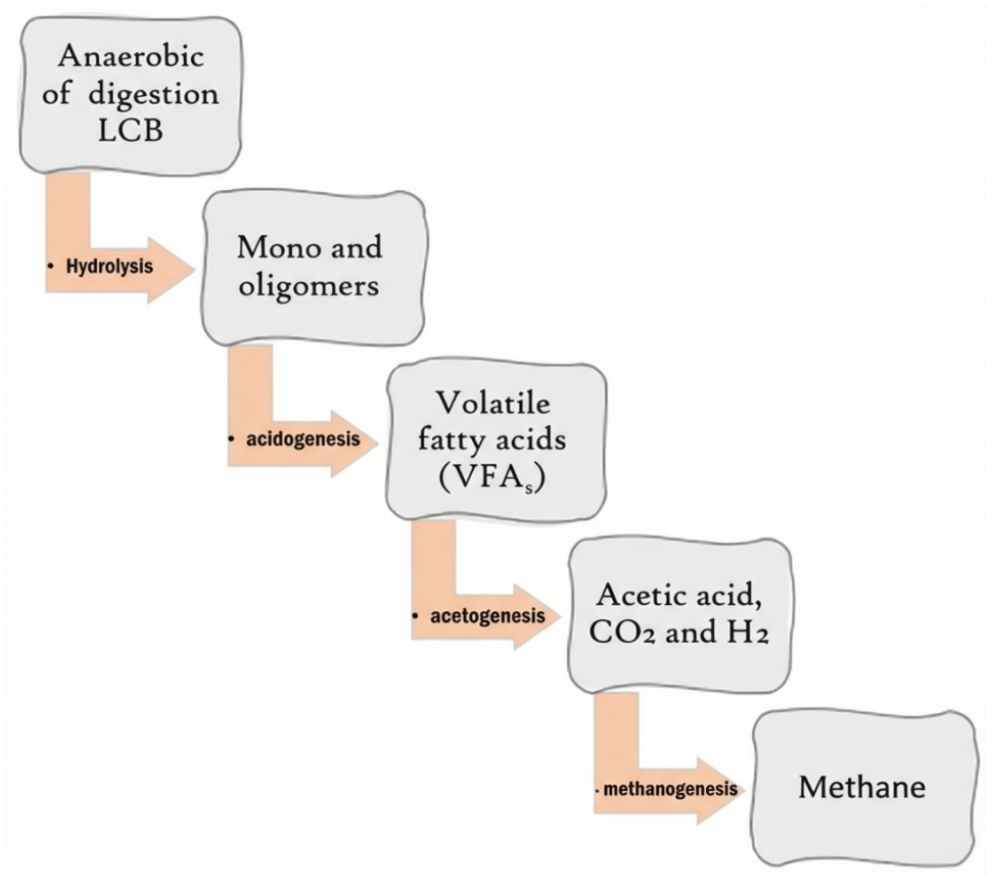

Figure 2. Wood lignocellulosic biomass (WLB) degradation processing.

The components of biogas include H_2O, N_2, O_2, H_2S, NH_3, and CO_2 [23]. The composition of biogas typically consists of 50–70% methane and 30–50% carbon dioxide [24]. This renewable energy source is produced from abundant raw materials, making it a cost-effective option with significant economic value [25]. Additionally,

the waste generated from the anaerobic digestion process serves as fertilizer, enhancing agricultural fertility while reducing the need for chemical pesticides [26].

2.1. Biogas applications

Biogas serves as a versatile energy carrier with critical applications across multiple sectors, underpinning its role in the transition to a sustainable energy system. Its primary uses can be categorized into three key areas: power generation, thermal energy production, and the provision of renewable fuel. When purified to biomethane (typically >95% methane content) through upgrading processes, biogas becomes fully compatible with existing natural gas infrastructure. This allows for its direct injection into the national gas grid. Consequently, biomethane can be utilized for household and industrial heating, electricity generation in gas-fired power plants, or as a high-quality vehicle fuel in the form of compressed natural gas (CNG). A distinct advantage of biomethane is its storability, which provides essential flexibility to balance supply and demand within the energy system [27].

The conversion of biogas into electricity via internal combustion engines, gas turbines, or fuel cells represents one of its most widespread and rapidly growing applications globally. This pathway delivers significant environmental benefits by simultaneously displacing fossil fuel-based power and mitigating greenhouse gas emissions. Crucially, it captures methane—a potent greenhouse gas—that would otherwise be released from the anaerobic decomposition of organic waste, thereby contributing to climate change mitigation and improved waste management.

Biogas can be used directly for thermal applications in boilers, furnaces, or in combined heat and power (CHP) systems. In such processes, a substantial portion of the biogas's chemical energy is efficiently converted into usable heat for industrial processes, space heating, or drying applications [28]. Direct thermal use, especially when implemented near the production site, offers a highly efficient and cost-effective energy solution. In summary, the diverse applications of biogas transform it from a simple waste treatment technology into an integrated, circular solution that addresses energy security, waste valorization, and environmental sustainability concurrently.

2.2. Characteristics of biogas

The calorific value of biogas is 0.8 times that of natural gas, and it diffuses in the air at a rate of 40 cm/s [24]. The calorific value and flammability of biogas depend on the methane content; if the amount of carbon dioxide exceeds 50%, biogas will not be flammable [25]. Removing carbon dioxide is the most costly stage in biogas production. As the CO_2 content increases, the amount of CH_4 decreases, resulting in a decrease in the calorific value and flame stability of biogas. When used directly, this can lead to issues such as unstable combustion and low heat intensity [26].

Biogas has a thermal energy content of 36.7 MJ/m^3. When converted into electricity using existing engines, it can yield approximately 2 kW of electricity per cubic meter [27]. Methane gas, which is obtained from biogas, possesses a high octane number and low carbon content. As compared to fossil fuels, it remarkably reduces the emission of pollutant gases [28].

2.3. Types of anaerobic fermentation digesters

There are various factors to consider when selecting a digestion method, including the execution environment, retention time, properties of the raw material, and available equipment [29]. In terms of removing organic matter, two main methods are commonly used: aerobic digestion and anaerobic digestion. Aerobic digestion results in the production of water and carbon dioxide as byproducts. On the other hand, anaerobic digestion (AD) produces methane, carbon dioxide, and a small amount of other gases. The proportions of these gases can vary depending on the type, properties, and quantity of the raw material [30]. Anaerobic digestion can be further categorized into solid (HS-AD) digestion and liquid (L-AD) digestion.

In solid-state anaerobic digestion, the dry matter content is typically above 15%, while in liquid-state anaerobic digestion, it is less than 10%. It has been observed that the production of methane increases significantly in the case of liquid digestion [31]. Comparing the liquid anaerobic digestion mode to the solid anaerobic digestion mode, the amount of methane produced is 13.6% higher in the former, which can be attributed to the optimal carbon-to-nitrogen (C/N) ratio in the liquid mode. However, it is worth noting that the hydrothermal slurry anaerobic digestion (HS-AD) method offers advantages over the liquid anaerobic digestion (L-AD) method, including smaller reactor dimensions, lower cost, minimal nutrient loss, reduced water consumption, and lower maintenance cost [32]. Anaerobic digestion can be conducted using either a single-stage or a two-stage process. In the single-stage method, all the necessary processes for methane production, as well as the destruction of organic compounds, are carried out in a single stage. On the other hand, the two-stage process involves the hydrolysis of organic compounds and the production of volatile fatty acids and H_2 in the first stage, followed by the production of methane in the second stage.

It has been observed that under both aerobic and anaerobic conditions, the hydrolysis process is more efficient when conducted in a two-stage system. This enhanced efficiency leads to an improved yield of methane [33].

When loading substances into the digester, it is possible to use a single material or a combination of multiple materials. However, a digester tends to be more efficient when loaded with several materials. This is because the efficiency of the digestion process increases, leading to accelerated degradation rates [34–36].

3. Types of biogas production digester models

3.1. Biogas production device with buoyancy gas chamber

This type of storage system, commonly referred to as the ”Indian model,” utilizes a floating cap tank to store gas. The tank moves up and down in response to changes in gas pressure, ensuring a consistent output pressure. However, this system requires regular maintenance, and ensuring a proper seal on the tank is crucial. Additionally, this model is not well-suited for cold regions due to high-temperature loss from the gas storage tank.

3.2. Biogas production device with fixed tank

This is known as the Chinese model, which has gained importance and efficiency due to its underground location. It offers advantages such as space-saving, minimal space requirements, heat stabilization, and resistance to cold regions.

3.3. Ideal conditions for the growth of bacteria and enzymes

Bacteria are the main factor in biogas production and it is necessary to provide optimal conditions to accelerate the process and increase the amount of biogas produced. Critical variables in biogas power plants include temperature, pH, C/N ratio, retention time, mixing, moisture percentage, particle size, digestion concentration microbial activity, hydrolysis rate, and biomass degradation degree [37].

3.3.1. Temperature

Temperature is a crucial factor in anaerobic digestive as it impacts enzyme activity and methane production yield [38]. Significant temperature drops, exceeding 2 degrees Celsius, have a decisive effect on gas production [39]. Rapid temperature fluctuations disrupt bacterial activity [40]. When the temperature falls below 30 °C, the digestion environment becomes acidic. Conversely, when the temperature surpasses 60 °C, the activity of microorganisms involved in digestion decreases and eventually ceases. The most optimal temperature from both technical and economic perspectives is the mesophilic temperature range, as it promotes stability in the digester [41]. Research has shown that the highest methane production occurs under mesophilic conditions [42]. Increasing the temperature in the anaerobic digestion (AD) process of biomass can lead to an increase in methane production [43]. Temperature plays a critical role in the separation and decomposition of solid materials, with better decomposition occurring at thermophilic temperatures compared to lower, cold-loving temperatures [44].

The production of biogas is significantly higher under thermophilic temperatures (55 °C) compared to cold temperatures (15 °C) [45]. This is because the endothermic digestion process leads to faster methane gas extraction, resulting in a shorter retention time. Therefore, thermophilic temperatures can be used in cases where there are limitations in the amount or size of the digester [46]. Furthermore, the inhibition of the system by ammonia in thermophilic digestion is less than in cryophilic digestion [47]. However, it's important to note that while there are several advantages to thermophilic conditions, they are more sensitive to environmental changes compared to mesophilic conditions [48]. Failure in the thermophilic process occurs when the temperature changes by more than one degree Celsius per day. To maintain stable anaerobic digestion, the temperature changes should be limited to less than 0.6 °C per day [38]. Additionally, biogas production is higher in mesophilic conditions compared to thermophilic conditions, attributed to the additional formation of volatile fatty acids [49].

3.3.2. pH and VFA

The optimal pH for biogas production is around neutral, ranging from 6.5 to 7.5. If the pH falls outside the range of 6 to 8, it can be detrimental to methanogenic bacteria and can lead to a decrease in biogas production [50]. It also hampers the production of

biogas and results in the accumulation of more acids [40]. Acidification of the digester significantly hinders further conversion of organic materials [51]. A pH of 6.5 or lower causes a significant decrease in the activity of microorganisms [52]. When the pH drops below 6, the percentage of methane in biogas decreases to less than 50%, making it non-flammable [53]. If the pH level of the environment decreases to less than 5.5, the bacteria become inactive [54]. VFAs determine the pH of the environment and are one of the most important parameters affecting AD [31]. The number of bacteria can be controlled by acid-producing bacteria and pH control [55,56].

3.3.3. C/N ratio

The performance of anaerobic digestion is significantly influenced by the C/N ratio [57]. To ensure stable anaerobic digestion in the long term, it is important to maintain a balanced C/N ratio [31]. The optimal C/N value for anaerobic digestion of mixed waste can be achieved by mixing carbon-rich waste streams with nitrogen-rich substrates such as food waste (FW) and cow manure (CM) [58]. Studies have reported the ideal C/N ratio for anaerobic digestion to be in the range of 21–31 [59, 60]. Maintaining a C/N ratio of 25–30 is recommended to keep the solution at a neutral pH (pH = 7) and produce biogas with approximately 70% methane content [53]. Some researchers have suggested using a lower C/N ratio than the optimal value as it is more effective for biogas production [52]. If the amount of carbon (C) is lower than the desired level, excess nitrogen (N) is stored in the digester, resulting in toxicity to the bacteria. This can lead to a high mortality rate among the bacteria. On the other hand, if the amount of nitrogen is insufficient, the microorganisms will not be able to survive due to a decrease in the available food source. In one study involving anaerobic digestion of three organic materials (dairy waste, chicken manure, and wheat straw), it was found that the highest methane production occurred at a C/N ratio of 27.2, with a constant pH and low cumulative ammonia concentration [61].

3.3.4. Time left

The retention time in a biogas production system is directly related to the amount of biogas produced. A longer retention time and a high rate of organic compounds result in an increased methane yield. Typically, the recommended retention time in such systems is between 30 and 50 days [62]. Over time, the amount of biogas produced will increase, but at a decreasing rate. While the overall biogas production increases, it may not be economically efficient in terms of the energy and time invested due to the diminishing returns.

3.3.5. Mixing

The purpose of mixing materials in the digester is to distribute nutrients within the digester [63], prevent the accumulation of sediment in the loaded materials, achieve uniform temperature throughout the digester, prevent foam formation, and aid in the release of biogas from the materials [64, 65]. Depending on the type of mixer used, the required energy for mixing can be reduced by up to 70% [66]. To enhance the methane production efficiency of biogas, some of the output material from the digester can be recycled back into the input [67]. Research has demonstrated that increasing the stirring speed results in a decrease in mixing time [68]. Paddle stirrers are suitable for

very viscous fluid and are very common to avoid floating layers. In addition, paddle mixers with slow speed are more efficient in energy consumption compared to floating mixers with high speed [69].

3.3.6. Percentage of moisture

Changes in humidity levels have a direct impact on gas production [70]. For optimal anaerobic fermentation in a biogas system, the ideal solid concentration is around 7–9%. Increasing the total solids (TS) content by 2–8% can result in a higher biogas yield, while a TS of 10% or higher may lead to a decrease in biogas production. When the TS level reaches 8%, the performance can be 1.5 times higher compared to a TS level of 5% [46]. However, it's important to note that higher TS levels can lead to an increase in volatile fatty acids (VFA) and a slight decrease in methane yield.

3.4. Ammonia

Ammonia is produced through the biological decomposition of organic matter and is commonly found in two forms: NH+4 and free ammonia (NH_3) [71]. It serves as an important growth factor for bacteria, although high concentrations of ammonia can be toxic to them [72]. Ammonia plays a crucial role in balancing the C/N ratio, and it can significantly impact the performance of anaerobic digestion (AD) by neutralizing the volatile fatty acids (VFA) generated during the process [61, 73]. However, excessive ammonia levels can hinder biogas production, cause digestion failures, and result in the release of ammonia into wastewater [74].

3.5. Long fatty acids

Biodegradation of long-chain fatty acids (LCFA) is the step that determines the rate of anaerobic digestion. The rate of degradation is limited by the initial concentration of LCFA, and when the concentration is too high, anaerobic digestion can fail [75]. The inhibition of the system by saturated fatty acids becomes more intense as the number of double bonds and chain length increase [76]. Food waste contains a significant amount of fat, with a concentration of about 5 g/L [77, 78].

4. Pre-treatment of biogas

After applying the parameters mentioned by the researchers, pretreatment is employed to enhance the competitiveness of the anaerobic digestion process. This approach accelerates and boosts the production rate of the process by utilizing the decomposition of organic materials [79, 80]. Lignocellulose typically possesses a resistant structure, but with the application of pretreatment, it becomes feasible to hydrolyze cellulose and hemicellulose, resulting in the conversion of polymeric carbohydrates into fermentable monomers. The analysis further investigates the extent of biogas production [81]. Previous studies have shown that the implementation of pretreatment increases the methane yield of LBs and decreases the digestion period [82, 83]. Recent experiments have demonstrated that pretreatment techniques enhance the process of dairy manure fermentation, leading to a significant increase in biogas production (up to 2 to 3 times) [84, 85]. These pretreatment methods

can be categorized into three main groups: physical (such as mechanical, thermal, and ultrasonic treatments), chemical (including acidic and alkaline methods), and biological pretreatment (involving the use of enzymes, fungal and microbial consortium pretreatment, microaerobic processes, and ensiling).

4.1. Mechanical pretreatment

Mechanical pretreatment is commonly employed before chemical and microbial pretreatment to achieve a synergistic effect [86]. Mechanical pretreatment involves crushing, which has two positive impacts on digestion performance. Firstly, it enhances methane production efficiency by expediting the reaction, primarily through an increase in specific surface area, thereby facilitating the digestion of LBs [87]. Secondly, it improves biomethane production efficiency by breaking down the complex structure and altering the morphology of LBs, including crystallinity, thus enhancing LBs' biodegradability [88]. For instance, researchers observed a 43% increase in methane yield by reducing the particle size of ley crop silage from 2 to 0.125 mm [88]. In a study, it was found that the consumption rate coefficient doubled when the average particle size decreased from 2.14 mm to 1.02 mm [31]. This indicates that reducing particle size can increase the biodegradability of LBs. When particle size is smaller, the digestion time is shortened, resulting in faster decomposition [89]. However, excessive mechanical pretreatment (such as excessive particle size reduction) may not favor methane production due to the accumulation of VFAs. This can lead to a deterioration in digestion performance [90] and a negative net energy output [88]. Another study reported a proportional decrease in methane production with a decrease in particle size of sunflower seed processing waste. The highest methane yield was observed when the particle size was between 1.4 and 2.0 mm [91].

4.2. Chemical pretreatments

Chemical pretreatments are commonly employed for the digestion of LBs [92]. These pretreatments mainly involve alkaline and acid treatments. Alkaline pretreatment aims to reduce cellulose crystallinity and lignin content by means of hydrolysis, consequently enhancing the porosity of LBs. This increased porosity facilitates the digestion process by microorganisms, making it the most widely utilized pretreatment method [87]. Typical chemical pretreatments include the addition of reagents such as ammonia fiber explosion, CO_2 explosion, as well as acidic and alkaline separation [93]. **Figure 3** illustrates the mechanism of alkaline pretreatment on LBs. The decomposition of LBs is challenging due to the presence of two crucial chemical bonds. The first bond is the hydrogen bond between lignin and polysaccharides, while the second bond is the ether-ester bond between hemicellulose and cellulose. These bonds are broken by OH produced by the alkaline precursor, which leads to easier decomposition of LBs [87].

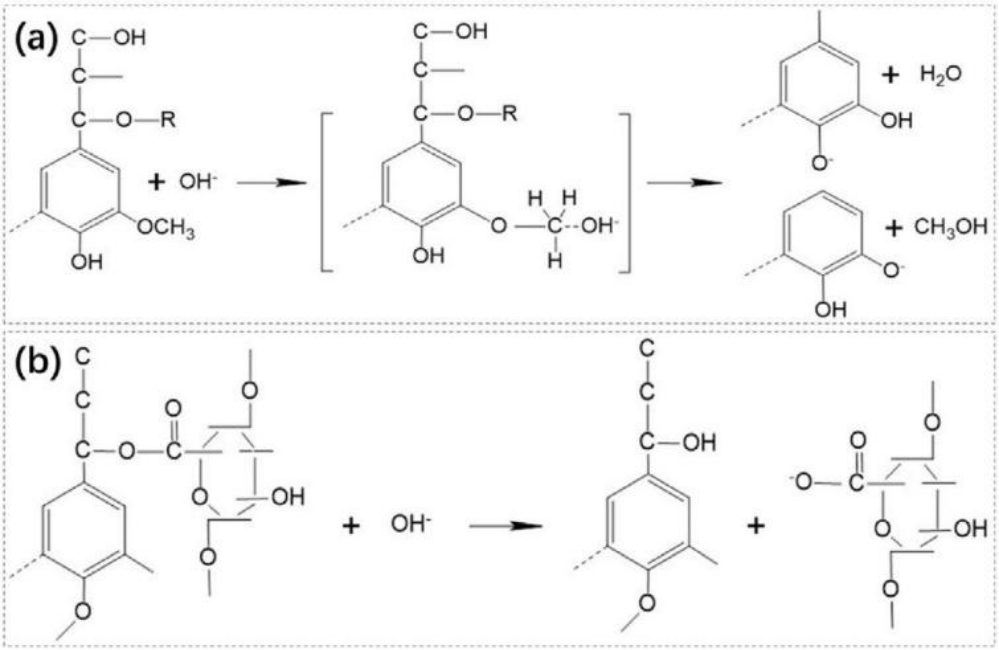

Figure 3. Mechanism of alkaline pretreatment: **(a)** Reaction mechanism between lignin and OH; **(b)** Reaction mechanism between lignin complex and OH [89].

After applying a pretreatment of 10% CaO, researchers observed an 11.99% increase in methane production [94]. For the acid peeling method, sugarcane bagasse was treated with hydrochloric acid (HCl 0.63 M) for a reaction time of 6.4 min at a temperature of 136 °C. After 30 days of incubation under mesophilic conditions (35 °C), 122.2 mL $CH_4.g^{-1}$ biomass was obtained [95]. Bases such as NaOH, potassium hydroxide (KOH), calcium hydroxide ($Ca(OH)_2$), or ammonium hydroxide (NH_4OH) help increase the porosity of the materials and reduce the degree of lignin polymerization [96]. This leads to the dissolution of lignin and makes hemicellulose more susceptible to enzymatic attack by microbes, resulting in a higher rate of biogas production [96, 97]. Alkaline pretreatment using sodium hydroxide (NaOH) is one of the most widely used thermochemical methods for pretreating lignocellulosic biomass [98]. During anaerobic digestion (AD), lignin can be a potential inhibitor to microorganisms. For instance, when the dissolved lignin concentration reaches 1.0 g/L, the hydrolysis efficiency can decrease by 25% [99]. Zhu et al. reported a significant increase in biogas yields, up to 57%, with an 8% NaOH pretreatment at 175 °C. The removal of lignin was considered the main contributing factor to this improvement [100]. Silica is another factor that inhibits the digestion of cellulosic materials [101, 102]. After NaOH pretreatment, the silica content was reduced by 88.7%, resulting in increased biodegradability of lignocellulosic biomass [86]. In another study, the pretreatment of raw materials with NaOH showed improved efficacy compared to untreated raw materials. reported a 111.6% increase in methane production from wheat straw pretreated with NaOH (4% NaOH at 37 °C for 120 h) [103].

Acidic pretreatment involves the addition of acid to the digester, and the acid used can include H_2SO_4, HCl, H_2O_2, and CH_3COOH. This pretreatment method is mainly targeted at dissolving hemicellulose, which is one of the components of lignocellulosic biomass (LBs). The acid breaks down the hemicellulose, resulting in significant changes

in the biodegradation of LBs. However, it's worth noting that acidic pretreatment generally has lower performance compared to alkaline pretreatment, even when using the same molar concentration of acid. This is primarily because acidic pretreatment has a limited effect on the structure of LBs. The acids, whether organic or inorganic, convert the hydrogen bonds between cellulose chains into a completely amorphous state. As a result, the cellulose becomes more susceptible to breakdown into glucose.

In summary, while acidic pretreatment can be effective in dissolving hemicellulose, it may not have as significant an impact on the overall structure of LBs compared to alkaline pretreatment. **Figures 4** and **5** illustrate the steps involved in the hydrolysis of the rigid lignocellulosic structure into a simpler and more easily digestible form for microorganisms. The two figures show that the use of inorganic acids yields better results compared to organic acids, mainly due to their stronger nature.

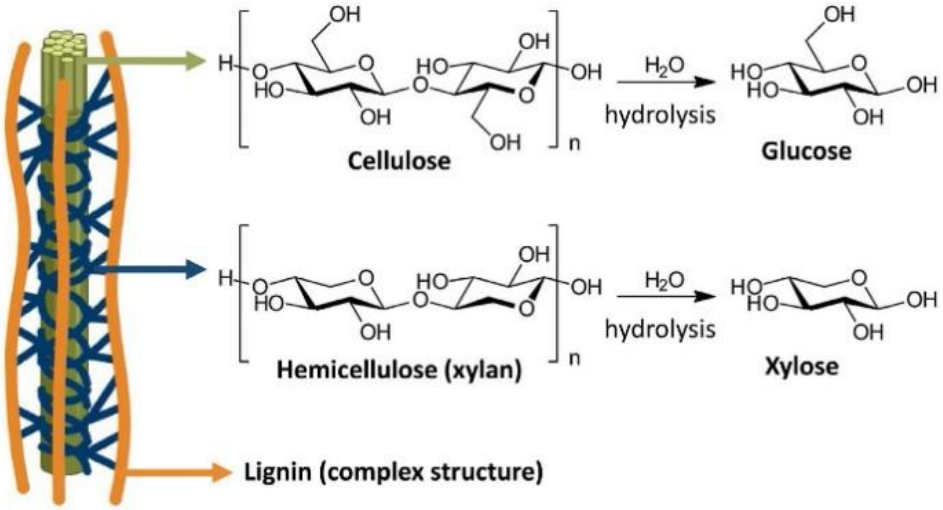

Figure 4. Simplified diagram of lignocellulosic structure and monomers formed after the combination of cellulose and hemicellulose hydrolysis [104].

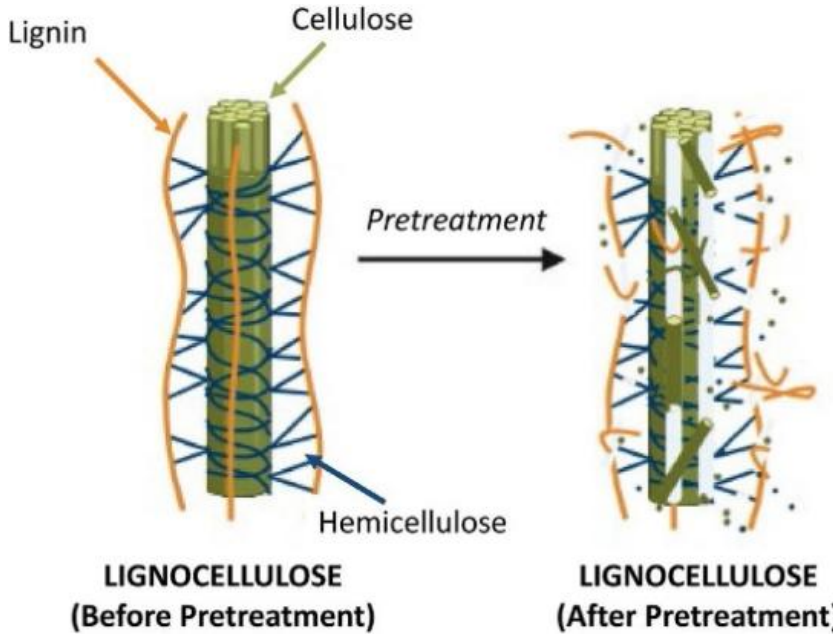

Figure 5. Simplified scheme of lignocellulosic structure disorder after pretreatment [104].

In a study comparing the effects of H_2SO_4, H_2O_2, HCl, and CH_3COOH pretreatments on rice straw, it was found that the biogas yield followed the order of 3% H_2O_2 > 2% H_2SO_4 > 2% HCl > 4% CH_3COOH. This indicates that pretreatment with hydrogen peroxide (H_2O_2) had the highest biogas production potential, followed by sulfuric acid (H_2SO_4), hydrochloric acid (HCl), and acetic acid (CH_3COOH) respectively. However, it is generally observed that organic acid pretreatment at low concentrations may not yield satisfactory results in terms of biogas production. On the other hand, high concentrations of organic acid pretreatment can lead to the loss of a significant amount of dry matter, which can be detrimental to anaerobic digestion (AD) processes. This suggests that finding the right balance and optimal conditions for pretreatment is crucial for efficient biogas production from lignocellulosic materials [105].

4.3. Thermal treatment methods

Heat treatment is a process that involves applying heat to substrates, which leads to deflocculation of macromolecules. This deflocculation occurs due to the increased surface area of the substrates. As a result, the degradation of complex compounds is improved, leading to an increase in soluble organic matter. Additionally, heat treatment interacts with the microbial population, facilitating a greater conversion of organic matter to biomethane [106]. Some recent studies have suggested that anaerobic digestion may not be economically viable when thermal pretreatments are used [107]. However, it is possible to make anaerobic digestion profitable through a series of operations that include increasing energy efficiency, enhancing operational capacity, and utilizing technological advancements [108]. These measures can contribute to ensuring the economic feasibility of anaerobic digestion with thermal pretreatment.

Substrate thermal pretreatment methods such as autoclaving, hot water baths, ovens (hot air ovens), and microwaving are used to keep the substrate warm [109]. In hot water baths, ovens, and autoclaves, heat is transferred through hot water, hot air, and steam, respectively. The optimal temperature ranges for hot air, microwave, autoclave, and hot water bath are 90–170 °C, 140–200 °C, 90–175 °C, and 90–100 °C, respectively. All thermal pretreatments have a positive effect on the dissolution of lignocellulosic biomass (LBs). However, it should be noted that high temperatures above 150 °C can cause the decomposition of lignin into phenolic compounds, which are toxic to microorganisms in anaerobic digestion (AD) [86].

4.4. Biological treatment methods

In addition to modifying the biomass structure, biological pretreatment methods have been shown to enhance methane yield through simultaneous digestion mechanisms [103]. This method offers several advantages, including low energy consumption [110] and environmental compatibility [111], which make it a promising approach.

Biological pretreatment can be achieved through microbial or enzymatic methods [86]. Microbial pretreatment is a commonly used approach, where fungi are capable of secreting cellulases, hemicellulases, and ligninase [112]. Enzymes

play a crucial role in modifying the lignin structure (such as the guaiacyl/sinapyl ratio), increasing material porosity, reducing cellulose crystallinity, and altering hemicellulose structure [113].

4.5. Combined pretreatment

Combined pretreatment methods include both physical and chemical changes and are usually more efficient than physical pretreatment or chemical pretreatment.

4.6. Heat-alkaline pretreatment

Since mixed cultures have a greater ability to break down lignocellulosic enzymes compared to single cultures, they were initially considered more effective. However, studies have shown that the pretreatment time required for mixed cultures is much longer compared to physical or chemical pretreatment methods. Mixed culture pretreatments can take several days or even weeks, although some are shorter than monoculture pretreatments [114]. Furthermore, the microbial structure of mixed cultures can change over time, potentially reducing their degradation ability. The ultimate advantage of monoculture pretreatment over mixed culture pretreatment is the ease of controlling growth conditions in a monoculture [115]. Alkaline or thermal-alkaline pretreatments initially focus on lignin removal followed by hemicellulose breakdown. The extent of cellulose degradation depends on various factors including the pretreatment type, raw materials, and methodology employed. Thermal-alkaline pretreatment offers advantages such as high buffering capacity, dissolution of COD, and delayering, thereby enhancing the performance of the anaerobic digestion (AD) process. Previous research indicates that thermal-alkaline pretreatment at 150 degrees Celsius with 1% NaOH is a more viable and cost-effective option [13,116]. Thermochemical pretreatment, which combines thermal and chemical methods, has been recognized as a highly beneficial pretreatment approach [19].

5. Nanoparticles for biogas production

Many nanoparticles are added as additives to the process, which can generally be divided into three categories:

(1) Zero valent iron nanoparticles (ZVI);
(2) Metal nanoparticles and metal oxide;
(3) Carbon-based nanoparticles.

5.1. Nanoparticles of zero-valent iron (ZVI)

Iron, also known as zero iron, can enhance the hydrolysis process in anaerobic digestion by acting as an electron donor [117]. Iron nanoparticles are unstable and gradually release iron ions, thereby promoting the activity of methanogenic microorganisms [118]. The introduction of iron has been shown to stimulate and stabilize the anaerobic digester, leading to improved performance in biogas production [119]. However, it should be noted that while the addition of iron nanoparticles initially increased biogas production within the first 48 h, excessively high concentrations resulted in bacteria poisoning and ultimately led to a decline in

biogas production [120]. The increase in biomethane production with the presence of iron nanoparticles can be attributed to the effect on the conditions of methanogenic microorganisms through the control of pH, the amount of volatile fatty acids, and the concentration of ammonia nitrogen [121].

5.2. Metal nanoparticles and metal oxides

Metals, as essential nutrients, play a crucial role in the efficiency and stability of agricultural biodigesters [122]. The incorporation of metal elements into anaerobic digestion can significantly enhance its performance. Apart from the essential elements found in food (N, O, H, and C), bacteria require metal elements such as metal ions (Al, Ca, Mg, K, and Na) and heavy ions (Ni, Zn, Cu, Co, Cr) to carry out aerobic processes [123]. Moreover, certain metal elements like Co, Cu, Fe, and Mo, and Ni can contribute to the stimulation and stabilization of anaerobic digestion for organic waste materials, even at low concentrations [124]. The addition of heavy metals such as Ni^{2+}, Zn^{2+}, and Cu^{2+} has been shown to improve the performance of the digester, with Ni^{2+} at 100 ppm yielding the best biogas production [125].

When the concentration of light and heavy metals is excessively high, it inhibits the system [38]. Zinc has a crucial role in enzymes and serves as a structural ion in the ester exchange factor, whereas copper is essential for coenzymes and biological electron transport [126]. In a study, the impact of four types of metal oxide nanoparticles (TiO_2, Al_2O_3, SiO_2, ZnO) on anaerobic digestion was examined, revealing that only ZnO had a detrimental effect on methane production, with no impact observed at low concentrations [127].

The increase in iron and zinc oxide nanoparticles and the decrease in cobalt oxide nanoparticles have a positive impact on methane production yield [128]. The researchers utilized Fe_3O_4 nanoparticles for anaerobic digestion of urban waste and determined the optimal dosage to be 75 g/L. They observed that if the nanoparticle dosage exceeds this amount, methane production will decrease [129].

5.3. Carbon-based nanoparticles

All compounds that contain carbon atoms in their structure are categorized as carbon-based nanomaterials, which are further classified based on their geometric structure. Graphene, fullerenes, and carbon nanotubes are significant examples of carbon-based nanoparticles used in various industries. Carbon nanotubes (CNTs) are nanometer-sized hollow tubes made up of carbon atoms, and they can exist as single-walled or multi-walled structures. Carbon nanotubes possess remarkable mechanical, absorption, electronic, and thermal properties, making them highly valuable in many industrial applications. Recently, they have also been explored for their potential use in biogas production, which is recognized as a branch of renewable energy.

Single-walled carbon nanotubes (SWCNTs) are cylindrical structures composed of a hexagonal lattice of carbon atoms. These nanomaterials play a crucial role in facilitating direct reciprocal electron transfer (DIET) in the anaerobic digestion (AD) process. Studies investigating the effects of SWCNTs on biogas production have

observed an accelerated consumption of the loading materials, leading to a rapid release of biogas and a reduction in processing time. However, the methane production yield remains constant throughout the process [130].

Multiwalled carbon nanotubes (MWCNTs) consist of multiple layers of nested single-walled carbon nanotubes [131]. These nanomaterials have shown potential in enhancing biogas production through electron transfer to methanogenic microorganisms. Another successful approach for biogas production involves the use of ash-based nanomaterials. In a research study, the addition of ash particles with nano/micro dimensions (obtained from a municipal solid waste incinerator) to the anaerobic digestion (AD) digester resulted in a significant increase in biogas production [132].

6. Analysis of technical, economic, and environmental effects

Pretreatment is vital for all types of biomass in biogas production, with cost being a significant factor. However, an economically viable and cost-effective pretreatment method is necessary. The primary challenge in biogas production is implementing a specialized pretreatment process to maximize biogas fuel production. This objective often involves mechanical pretreatment and optimizing associated parameters. However, at large industrial scales, mechanical pretreatment can incur high energy, operating, and maintenance costs, leading to increased overall biogas production expenses. Consequently, combined pretreatment approaches prove more economically feasible than single pretreatment methods for achieving efficient biogas production. Biological pretreatment is an environmentally friendly method, although its effectiveness is inferior to thermochemical pretreatments. Additionally, it is worth noting that zero-valent iron nanoparticles show great promise in enhancing biogas production. A summary of key pretreatment conditions, substrates, and corresponding biogas yields is given in **Table 1**.

Table 1. Summary of Key Pretreatment Conditions, Substrates, and Corresponding Biogas Yields.

Substrate	Pretreatment method & key conditions	Effect on biogas/methane yield
Ley crop silage	Mechanical: Particle size reduction (from 2 mm to 0.125 mm)	Increased methane yield by ~43%.
Wheat straw	Mechanical: Particle size reduction (average size from 2.14 mm to 1.02 mm)	Doubled the consumption rate coefficient, indicating increased biodegradability.
Sunflower seed waste	Mechanical: Particle size optimization (1.4–2.0 mm)	Highest methane yield was observed within this particle size range.
Wheat straw	Alkaline (NaOH): 4% NaOH at 37 °C for 120 h	Increased methane production by 111.6% compared to untreated straw.
Lignocellulosic biomass	Alkaline (NaOH): 8% NaOH at 175 °C	Increased biogas yields up to 57%, primarily due to lignin removal.
Lignocellulosic biomass	Alkaline (NaOH): General pretreatment	Silica content reduced by 88.7%, significantly increasing biomass biodegradability.
Various biomasses	Alkaline (CaO): 10% CaO pretreatment	Increased methane production by 11.99%.
Sugarcane bagasse	Acidic (HCl): 0.63 M HCl, 136 °C, 6.4 min reaction time	Yielded 122.2 mL CH_4 per gram of volatile solids (VS) after 30 days under mesophilic digestion (35 °C).

Table 1. *Cont.*

Substrate	Pretreatment method & key conditions	Effect on biogas/methane yield
Rice straw	Comparative Acidic: 3% H_2O_2, 2% H_2SO_4, 2% HCl, 4% CH_3COOH	Biogas yield order: 3% H_2O_2 2% H_2SO_4 2% HCl 4% CH_3COOH. Hydrogen peroxide pretreatment showed the highest potential.
Dairy manure	Thermal-Alkaline: 150 °C with 1% NaOH	Identified as a more viable and cost-effective pretreatment option, enhancing Anaerobic Digestion (AD) performance via high buffering capacity and COD dissolution.
Waste Flower Straw	Biogas Slurry Pretreatment	Enhanced biogas production characteristics in anaerobic digestion.
Pinewood	Mesophilic Aerobic Digestion (Biological)	An efficient and inexpensive biological pretreatment improving biogas production from highly-recalcitrant feedstock.
(General)	Thermal Pretreatment: Hot air (90–170 °C), Microwave (140–200 °C), Autoclave (90–175 °C), Hot water bath (90–100 °C)	All have a positive effect on dissolving lignocellulosic biomass. Caution: Temperatures 150 °C may degrade lignin into phenolic compounds toxic to AD microorganisms.
(General - Nanoparticles)	Additive: Zero-Valent Iron (ZVI) Nanoparticles	Enhances hydrolysis as an electron donor; stabilizes digester and improves biogas production. Optimal concentration is critical as excess causes bacterial inhibition.
Urban waste	Additive: Fe_3O_4 Nanoparticles at 75 mg/L	Optimal dosage for enhanced methane production. Dosages exceeding this level led to decreased methane yield.

7. Conclusion

Fossil fuel pollution, which supplies the largest amount of energy in the world, is the main factor in changing the energy source towards renewable energy. The primary sources of biogas are found in abundance in the world, and according to the geographical location and living conditions, its type is different. According to the two approaches presented, the source of biogas production is adopted. Several factors, including temperature, reactor type, input concentration, input material type, and mixing, impact biogas production. To optimize and increase the production rate, the addition of pretreatment materials that yield positive effects is often beneficial. However, it is essential to evaluate the economic efficiency of such pretreatments. The ultimate objective is to reduce the overall cost of the production process while creating favorable conditions for bacteria.

Temperature fluctuations can disrupt bacterial activity and even halt their metabolic processes. Extensive research indicates that the most favorable temperature conditions for efficient digestion and maximum biogas production are typically within the mesophilic range. Maintaining stable temperature conditions within this range is crucial for optimizing production yields. Mixing time is inversely related to the fermentation speed and plays a vital role in preventing sedimentation within the digester. The carbon-to-nitrogen (C/N) ratio, commonly found to be around 25 in various studies, is a key parameter influencing microbial activity and biogas production. While a small amount of ammonia is necessary for bacterial survival, exceeding the recommended threshold can lead to digestive toxicity and inhibit biogas production. It should be noted that the concentration and size of the loaded materials should not be too low or too high; Because it will disturb the digestion process. The economic efficiency parameter is a limiting factor that has a specific range and there is no economic value of production outside this range. Speeding up and increasing the amount of production, which is the main goal, can be strengthened by using

pre-treatment. Pretreatment is the most common way to improve the AD efficiency of LBs.

Pretreatment is a process that breaks down the rigid structure of lignocellulose, converting it into fermentable monomers. This results in a reduction in the digestion period and a significant increase in biogas yield (2–3 times). While physical pretreatment is effective, it often requires high energy consumption, making it less cost-effective. Additionally, excessive reduction during physical pretreatment can lead to the accumulation of volatile fatty acids. On the other hand, chemical pretreatment is considered the most efficient method for enhancing AD efficiency. However, it has drawbacks such as potential secondary pollution and the production of toxins. Therefore, a careful balance between effectiveness and the associated drawbacks needs to be considered when selecting the appropriate pretreatment method. It has been observed that among chemical pretreatments, alkaline pretreatment exhibits the highest performance. Sodium hydroxide (NaOH) is a commonly used alkaline pretreatment in anaerobic digestion applications. Comparatively, acidic pretreatment shows lower performance than alkaline pretreatment when used at the same molar concentration.

Funding: This work received no external funding.

Institutional review board statement: Not applicable.

Informed consent statement: Not applicable.

Data availability statement: Data sharing is not applicable to this article as no new data were created or analyzed in this study.

Conflict of interest: The author declares no conflict of interest.

References

1. Ghasemian S, Faridzad A, Abbaszadeh P, et al. An overview of global energy scenarios by 2040: Identifying the driving forces using cross-impact analysis method. International Journal of Environmental Science and Technology. 2024; 21: 7749–7772.
2. Shaibur MR, Husain H, Arpon SH. Utilization of cow dung residues of biogas plant for sustainable development of a rural community. Current Research in Environmental Sustainability. 2021; 3: 100026.
3. Khelifi O, Laksaci H, Merabti MA, et al. Production of biofuel from Washingtonia fruits by anaerobic digestion with *Saccharomyces cerevisiae*: Process optimization. Fuel. 2024; 358(Part A): 130240.
4. Kusmiyati K, Wijaya DK, Hartono BR, et al. Harnessing the power of cow dung: Exploring the environmental, energy, and economic potential of biogas production in Indonesia. Results in Engineering. 2023; 20: 101431.
5. Tumusiime E, Kirabira JB, Musinguzi WB. Optimization of substrate mixing ratios for wet anaerobic digestion of selected organic waste streams for productive biogas systems. Energy Reports. 2022; 8: 10409–10417.
6. Abanades S, Abbaspour H, Ahmadi A, et al. A critical review of biogas production and usage with legislations framework across the globe. International Journal of Environmental Science and Technology. 2022; 19: 3377–3400.
7. Khelifi O, Sbai S, Selka H, et al. Statistical optimization and kinetic study of biofuel production from wastes fruits by saccharification and fermentation. Energy. 2025; 315: 134276.
8. McCabe BK, Schmidt T. Integrated Biogas Systems: Local Applications of Anaerobic Digestion towards Integrated Sustainable Solutions. Murphy, J.D. (editor). IEA Bioenergy; 2018.
9. Patinvoh RJ, Osadolor OA, Chandolias K, et al. Innovative pretreatment strategies for biogas production. Bioresource Technology. 2017; 224: 13–24.
10. Nganyira PD, Mahushi DJ, Balengayabo JG, et al. Quality of biogas generated through co-digestion of Brewer's

spent grain and cattle dung. Energy Reports. 2023; 10: 2330–2336.
11. Ahmad F, Sakamoto IK, Adorno MAT, et al. Methane production from hydrogen peroxide assisted hydrothermal pretreatment of solid fraction sugarcane bagasse. Waste and Biomass Valorization. 2020; 11: 31–50.
12. Balat M. Production of bioethanol from lignocellulosic materials via the biochemical pathway: A review. Energy Conversion and Management. 2011; 52(2): 858–875.
13. Rahmani AM, Tyagi VK, Gunjyal N, et al. Hydrothermal and thermal-alkali pretreatments of wheat straw: Co-digestion, substrate solubilization, biogas yield and kinetic study. Environmental Research. 2023; 216(Part 1): 114436.
14. Rahman MA, Møller HB, Saha CK, et al. The effect of temperature on the anaerobic co-digestion of poultry droppings and sugar mill press mud. Biofuels. 2022; 13(2): 139–147.
15. Ahmadi-Pirlou M, Ebrahimi-Nik M, Khojastehpour M, et al. Mesophilic co-digestion of municipal solid waste and sewage sludge: Effect of mixing ratio, total solids, and alkaline pretreatment. International Biodeterioration and Biodegradation. 2017; 125: 97–104.
16. Bora BJ, Saha UK. Experimental evaluation of a rice bran biodiesel–biogas run dual fuel diesel engine at varying compression ratios. Renewable Energy. 2016; 87(Part 1): 782–790.
17. Emmanuel JK, Nganyira PD, Shao GN. Evaluating the potential applications of brewers' spent grain in biogas generation, food and biotechnology industry: A review. Heliyon. 2022; 8(10): e11140.
18. Kiran EU, Trzcinski AP, Ng WJ, et al. Bioconversion of food waste to energy: A review. Fuel. 2014; 134: 389–399.
19. Ram NR, Nikhil GN. A critical review on sustainable biogas production with focus on microbial-substrate interactions: Bottlenecks and breakthroughs. Bioresource Technology Reports. 2022; 19: 101170.
20. Pan SY, Tsai CY, Liu CW, et al. Anaerobic co-digestion of agricultural wastes toward circular bioeconomy. iScience. 2021; 24(7): 102704.
21. Kothari R, Pandey AK, Kumar S, et al. Different aspects of dry anaerobic digestion for bio-energy: An overview. Renewable and Sustainable Energy Reviews. 2014; 39: 174–195.
22. Detman A, Bucha M, Treu L, et al. Evaluation of acidogenesis products' effect on biogas production performed with metagenomics and isotopic approaches. Biotechnology for Biofuels. 2021; 14(1): 125.
23. Awe OW, Zhao Y, Nzihou A, et al. A review of biogas utilisation, purification and upgrading technologies. Waste and Biomass Valorization. 2017; 8: 267–283.
24. Xia ZM, Li XS, Chen ZY, et al. Hydrate-based CO_2 capture and CH_4 purification from simulated biogas with synergic additives based on gas solvent. Applied Energy. 2016; 162: 1153–1159.
25. Pohland FG (editor). Anaerobic Biological Treatment Processes. American Chemical Society; 1971.
26. Møller HB, Sørensen P, Olesen JE, et al. Agricultural biogas production—Climate and environmental impacts. Sustainability. 2022; 14(3): 1849.
27. Indrawan N, Thapa S, Wijaya ME, et al. The biogas development in the Indonesian power generation sector. Environmental Development. 2018; 25: 85–99.
28. Tricase C, Lombardi M. State of the art and prospects of Italian biogas production from animal sewage: Technical-economic considerations. Renewable Energy. 2009; 34(3): 477–485.
29. Paritosh K, Kushwaha SK, Yadav M, et al. Food waste to energy: An overview of sustainable approaches for food waste management and nutrient recycling. BioMed Research International. 2017; 2017(1): 2370927.
30. Alam M, Sultan MB, Mehnaz M, et al. Production of biogas from food waste in laboratory scale dry anaerobic digester under mesophilic condition. Energy Nexus. 2022; 7: 100126.
31. Zhang C, Su H, Baeyens J, et al. Reviewing the anaerobic digestion of food waste for biogas production. Renewable and Sustainable Energy Reviews. 2014; 38: 383–392.
32. Sun Y, Wang D, Yan J, et al. Effects of lipid concentration on anaerobic co-digestion of municipal biomass wastes. Waste Management. 2014; 34(6): 1025–1034.
33. Rafieenia R, Girotto F, Peng W, et al. Effect of aerobic pre-treatment on hydrogen and methane production in a two-stage anaerobic digestion process using food waste with different compositions. Waste Management. 2017; 59: 194–199.
34. Catherine C, Twizerimana M. Biogas production from thermochemically pretreated sweet potato root waste. Heliyon. 2022; 8(9): e10376.
35. Castro-Molano LP, Escalante-Hernández H, Lambis-Benítez LE, et al. Synergistic effects in anaerobic codigestion of chicken manure with industrial wastes. Dyna. 2018; 85(206): 135–141.
36. Kasinath A, Fudala-Ksiazek S, Szopinska M, et al. Biomass in biogas production: Pretreatment and codigestion.

Renewable and Sustainable Energy Reviews. 2021; 150: 111509.
37. Dioha IJ, Ikeme CH, Nafi'u T, et al. Effect of carbon to nitrogen ratio on biogas production. International Research Journal of Natural Sciences. 2013; 1(3): 1–10.
38. Appels L, Van Assche A, Willems K, et al. Peracetic acid oxidation as an alternative pre-treatment for the anaerobic digestion of waste activated sludge. Bioresource Technology. 2011; 102(5): 4124–4130.
39. Mulat DG, Feilberg A. GC/MS method for determining carbon isotope enrichment and concentration of underivatized short-chain fatty acids by direct aqueous solution injection of biogas digester samples. Talanta. 2015; 143: 56–63.
40. Rea J. Kinetic Modeling and Experimentation of Anaerobic Digestion [Bachelor's Thesis]. Massachusetts Institute of Technology; 2014.
41. Elanur ADAR. Optimization of cattle manure liquid fraction anaerobic digestion at different temperatures: Modelling by Taguchi method. Sigma Journal of Engineering and Natural Sciences. 2020; 38(4): 1753–1766.
42. Kovács E, Wirth R, Maróti G, et al. Augmented biogas production from protein-rich substrates and associated metagenomic changes. Bioresource Technology. 2015; 178: 254–261.
43. González-Fernández C, Sialve B, Bernet N, et al. Impact of microalgae characteristics on their conversion to biofuel. Part II: Focus on biomethane production. Biofuels, Bioproducts and Biorefining. 2012; 6(2): 205–218.
44. Kaparaju P, Angelidaki I. Effect of temperature and active biogas process on passive separation of digested manure. Bioresource Technology. 2008; 99(5): 1345–1352.
45. Wang S, Ma F, Ma W, et al. Influence of temperature on biogas production efficiency and microbial community in a two-phase anaerobic digestion system. Water. 2019; 11(1): 133.
46. Curry N, Pillay P. Biogas prediction and design of a food waste to energy system for the urban environment. Renewable Energy. 2012; 41: 200–209.
47. Gallert C, Bauer S, Winter J. Effect of ammonia on the anaerobic degradation of protein by a mesophilic and thermophilic biowaste population. Applied Microbiology and Biotechnology. 1998; 50: 495–501.
48. Kim JK, Oh BR, Chun YN, et al. Effects of temperature and hydraulic retention time on anaerobic digestion of food waste. Journal of Bioscience and Bioengineering. 2006; 102(4): 328–332.
49. Lattieff FA. A study of biogas production from date palm fruit wastes. Journal of Cleaner Production. 2016; 139: 1191–1195.
50. Muvhiiwa RF, Matambo TS, Chafa PM, et al. Effect of temperature and pH on biogas production from cow dung and dog faeces. Africa Insight. 2016; 45(4): 167–181.
51. Zhang L, Jahng D. Long-term anaerobic digestion of food waste stabilized by trace elements. Waste Management. 2012; 32(8): 1509–1515.
52. Wagner AO, Lins P, Malin C, et al. Impact of protein-, lipid- and cellulose-containing complex substrates on biogas production and microbial communities in batch experiments. Science of the Total Environment. 2013; 458–460: 256–266.
53. Rao PV, Baral SS, Dey R, et al. Biogas generation potential by anaerobic digestion for sustainable energy development in India. Renewable and Sustainable Energy Reviews. 2010; 14(7): 2086–2094.
54. Sharma DK. Studies on Availability and Utilization of Onion Storage Waste in a Rural Habitat [PhD Thesis]. Indian Institute of Technology Delhi; 2002.
55. Horiuchi JI, Shimizu T, Tada K, et al. Selective production of organic acids in anaerobic acid reactor by pH control. Bioresource Technology. 2002; 82(3): 209–213.
56. Fang HH, Liu H. Effect of pH on hydrogen production from glucose by a mixed culture. Bioresource Technology. 2002; 82(1): 87–93.
57. Zeshan, Karthikeyan OP, Visvanathan C. Effect of C/N ratio and ammonia-N accumulation in a pilot-scale thermophilic dry anaerobic digester. Bioresource Technology. 2012; 113: 294–302.
58. Korai RM, Li X. Effect of ultrasonic assisted KOH pretreatment on physiochemical characteristic and anaerobic digestion performance of wheat straw. Chinese Journal of Chemical Engineering. 2020; 28(9): 2409–2416.
59. Iyovo GD, Du G, Chen J. Sustainable bioenergy bioprocessing: Biomethane production, digestate as biofertilizer and as supplemental feed in algae cultivation to promote algae biofuel commercialization. Journal of Microbial and Biochemical Technology. 2010; 2(4): 100–106.
60. Zhou J, Qu A, Ming S, et al. Binary-component anaerobic co-digestion: Synergies and microbial profiles. Renewable Energy. 2022; 201(Part 2): 1–10.
61. Zhang Y, Yue D, Liu J, et al. Effect of organic compositions of aerobically pretreated municipal solid waste

on non-methane organic compound emissions during anaerobic degradation. Waste Management. 2012; 32(6): 1116–1121.
62. Diltz R, Pullammanappallil P. Biofuels from algae. In: Fang Z (editor). Liquid, Gaseous and Solid Biofuels: Conversion Techniques. IntechOpen; 2013. pp. 431–449.
63. Zabaleta I, Rodic L. Recovery of essential nutrients from municipal solid waste–Impact of waste management infrastructure and governance aspects. Waste Management. 2015; 44: 178–187.
64. Naegele HJ, Mönch-Tegeder M, Haag NL, et al. Effect of substrate pretreatment on particle size distribution in a full-scale research biogas plant. Bioresource Technology. 2014; 172: 396–402.
65. Hosseini SE, Wahid MA. Development of biogas combustion in combined heat and power generation. Renewable and Sustainable Energy Reviews. 2014; 40: 868–875.
66. Lemmer A, Naegele HJ, Sondermann J. How efficient are agitators in biogas digesters? Determination of the efficiency of submersible motor mixers and incline agitators by measuring nutrient distribution in full-scale agricultural biogas digesters. Energies. 2013; 6(12): 6255–6273.
67. Sreekrishnan TR, Kohli S, Rana V. Enhancement of biogas production from solid substrates using different techniques—A review. Bioresource Technology. 2004; 95(1): 1–10.
68. Melton LA, Lipp CW, Spradling RW, et al. Dismt-determination of mixing time through color changes. Chemical Engineering Communications. 2002; 189(3): 322–338.
69. Annas S, Elfering M, Jantzen HA, et al. Experimental analysis of mixing-processes in biogas plants. Chemical Engineering Science. 2022; 258: 117767.
70. Lohani SP, Chhetri A, Adhikari J, et al. Sustainable biogas production potential from urban wastewater in Nepal. International Journal of Environmental Science and Development. 2013; 4(5): 595–599.
71. Whelan MJ, Everitt T, Villa R. A mass transfer model of ammonia volatilisation from anaerobic digestate. Waste Management. 2010; 30(10): 1808–1812.
72. Kim DH, Oh SE. Continuous high-solids anaerobic co-digestion of organic solid wastes under mesophilic conditions. Waste Management. 2011; 31(9–10): 1943–1948.
73. Wang X, Yang G, Feng Y, et al. Optimizing feeding composition and carbon–nitrogen ratios for improved methane yield during anaerobic co-digestion of dairy, chicken manure and wheat straw. Bioresource Technology. 2012; 120: 78–83.
74. Park J, Jin HF, Lim BR, et al. Ammonia removal from anaerobic digestion effluent of livestock waste using green alga Scenedesmus sp. Bioresource Technology. 2010; 101(22): 8649–8657.
75. Oh ST, Martin AD. Long chain fatty acids degradation in anaerobic digester: Thermodynamic equilibrium consideration. Process Biochemistry. 2010; 45(3): 335–345.
76. Lalman J, Bagley DM. Effects of C18 long chain fatty acids on glucose, butyrate and hydrogen degradation. Water Research. 2002; 36(13): 3307–3313.
77. Kim SG. System for separation of oil and sludge from food waste leachate. KR20110133989A, 8 June 2010.
78. Zhang C, Su H, Tan T. Batch and semi-continuous anaerobic digestion of food waste in a dual solid–liquid system. Bioresource Technology. 2013; 145: 10–16.
79. Jain S, Jain S, Wolf IT, et al. A comprehensive review on operating parameters and different pretreatment methodologies for anaerobic digestion of municipal solid waste. Renewable and Sustainable Energy Reviews. 2015; 52: 142–154.
80. Zheng Y, Zhao J, Xu F, et al. Pretreatment of lignocellulosic biomass for enhanced biogas production. Progress in Energy and Combustion Science. 2014; 42: 35–53.
81. Li Z, Chen CH, Liu T, et al. Catalysis with Cu(II) (bpy) improves alkaline hydrogen peroxide pretreatment. Biotechnology and Bioengineering. 2013; 110(4): 1078–1086.
82. Guan R, Li X, Wachemo AC, et al. Enhancing anaerobic digestion performance and degradation of lignocellulosic components of rice straw by combined biological and chemical pretreatment. Science of the Total Environment. 2018; 637–638: 9–17.
83. Li Q, Zhang W, Yi F, et al. Effect of biogas slurry pretreatment on biogas production characteristics in anaerobic digestion of waste flower straw. China Biogas. 2020; 38(3): 52–56. (in Chinese)
84. Kim JR, Karthikeyan KG. Effects of severe pretreatment conditions and lignocellulose-derived furan byproducts on anaerobic digestion of dairy manure. Bioresource Technology. 2021; 340: 125632.
85. Kim JR, Karthikeyan KG. Solubilization of lignocellulosic biomass using pretreatments for enhanced methane production during anaerobic digestion of manure. ACS ES&T Engineering. 2021; 1(4): 753–760.

86. Cai Y, Zheng Z, Schäfer F, et al. A review about pretreatment of lignocellulosic biomass in anaerobic digestion: Achievement and challenge in Germany and China. Journal of Cleaner Production. 2021; 299: 126885.
87. Yu Q, Liu R, Li K, et al. A review of crop straw pretreatment methods for biogas production by anaerobic digestion in China. Renewable and Sustainable Energy Reviews. 2019; 107: 51–58.
88. Lindmark J, Leksell N, Schnürer A, et al. Effects of mechanical pre-treatment on the biogas yield from ley crop silage. Applied Energy. 2012; 97: 498–502.
89. Kang X, Zhang Y, Song B, et al. The effect of mechanical pretreatment on the anaerobic digestion of Hybrid Pennisetum. Fuel. 2019; 252: 469–474.
90. Ferreira LC, Nilsen PJ, Fdz-Polanco F, et al. Biomethane potential of wheat straw: Influence of particle size, water impregnation and thermal hydrolysis. Chemical Engineering Journal. 2014; 242: 254–259.
91. De la Rubia MA, Fernández-Cegrí V, Raposo F, et al. Influence of particle size and chemical composition on the performance and kinetics of anaerobic digestion process of sunflower oil cake in batch mode. Biochemical Engineering Journal. 2011; 58–59: 162–167.
92. Solé-Bundó M, Eskicioglu C, Garfí M, et al. Anaerobic co-digestion of microalgal biomass and wheat straw with and without thermo-alkaline pretreatment. Bioresource Technology. 2017; 237: 89–98.
93. Kim I, Han JI. Optimization of alkaline pretreatment conditions for enhancing glucose yield of rice straw by response surface methodology. Biomass and Bioenergy. 2012; 46: 210–217.
94. Solé-Bundó M, Carrère H, Garfí M, et al. Enhancement of microalgae anaerobic digestion by thermo-alkaline pretreatment with lime (CaO). Algal Research. 2017; 24(Part A): 199–206.
95. Leitão RC, Costa AG, Cassales AR, et al. Anaerobic biodegradability of residues from biofuel production chains: Sugarcane bagasse. Research and Development Bulletin 80: Embrapa Tropical Agroindustry, Fortaleza-CE. 2013; 80: 1–41. (in Portuguese)
96. Sundberg M. Pretreatment of Biomass Investigation of suitable pretreatment of Icelandic biomass for biofuel production. Mannvit hf.; 2010.
97. Vu HP, Nguyen LN, Vu MT, et al. A comprehensive review on the framework to valorise lignocellulosic biomass as biorefinery feedstocks. Science of the Total Environment. 2020; 743: 140630.
98. Saratale GD, Oh MK. Improving alkaline pretreatment method for preparation of whole rice waste biomass feedstock and bioethanol production. RSC Advances. 2015; 5(118): 97171–97179.
99. Koyama M, Yamamoto S, Ishikawa K, et al. Inhibition of anaerobic digestion by dissolved lignin derived from alkaline pre-treatment of an aquatic macrophyte. Chemical Engineering Journal. 2017; 311: 55–62.
100. Zhou J, Yan BH, Wang Y, et al. Effect of steam explosion pretreatment on the anaerobic digestion of rice straw. RSC Advances. 2016; 6(91): 88417–88425.
101. Kaur K, Phutela UG. Enhancement of paddy straw digestibility and biogas production by sodium hydroxide-microwave pretreatment. Renewable Energy. 2016; 92: 178–184.
102. Chandra R, Takeuchi H, Hasegawa T, et al. Improving biodegradability and biogas production of wheat straw substrates using sodium hydroxide and hydrothermal pretreatments. Energy. 2012; 43(1): 273–282.
103. Karami K, Karimi K, Mirmohamadsadeghi S, et al. Mesophilic aerobic digestion: An efficient and inexpensive biological pretreatment to improve biogas production from highly-recalcitrant pinewood. Energy. 2022; 239(Part E): 122361.
104. Camargo FP, Rabelo CA, Duarte IC, et al. Biogas from lignocellulosic feedstock: A review on the main pretreatments, inocula and operational variables involved in anaerobic reactor efficiency. International Journal of Hydrogen Energy. 2023; 48(54): 20613–20632.
105. Song Z, Yang G, Liu X, et al. Comparison of seven chemical pretreatments of corn straw for improving methane yield by anaerobic digestion. PLoS One. 2014; 9(4): e93801.
106. Wid N, Raudin N. Recovery of biogas from food waste using treated and untreated anaerobic digestion. IOP Conference Series: Earth and Environmental Science. 2023; 1205(1): 012004.
107. de Oliveira MC, Bassin ID, Cammarota MC. Microalgae and cyanobacteria biomass pretreatment methods: A comparative analysis of chemical and thermochemical pretreatment methods aimed at methane production. Fermentation. 2022; 8(10): 497.
108. Kim JR, Hu Y, Zavala VM, K, et al. Techno-economic analysis of pretreatments to dairy manure biomass for enhanced biogas production. Bioresource Technology Reports. 2022; 20: 101275.
109. Kainthola J, Shariq M, Kalamdhad AS, et al. Enhanced methane potential of rice straw with microwave assisted pretreatment and its kinetic analysis. Journal of Environmental Management. 2019; 232: 188–196.

110. Neshat SA, Mohammadi M, Najafpour GD, et al. Anaerobic co-digestion of animal manures and lignocellulosic residues as a potent approach for sustainable biogas production. Renewable and Sustainable Energy Reviews. 2017; 79: 308–322.
111. Kavitha S, Gondi R, Kannah RY, et al. A review on current advances in the energy and cost effective pretreatments of algal biomass: Enhancement in liquefaction and biofuel recovery. Bioresource Technology. 2022; 344: 128383.
112. Guo J, Cui X, Sun H, et al. Effect of glucose and cellulase addition on wet-storage of excessively wilted maize stover and biogas production. Bioresource Technology. 2018; 259: 198–206.
113. Rouches E, Herpoël-Gimbert I, Steyer JP, et al. Improvement of anaerobic degradation by white-rot fungi pretreatment of lignocellulosic biomass: A review. Renewable and Sustainable Energy Reviews. 2016; 59: 179–198.
114. Jin X, Wei S. Efficient short time pretreatment on lignocellulosic waste using an isolated fungus *Trametes* sp. W-4 for the enhancement of biogas production. Heliyon. 2023; 9(3): e14573.
115. Wei S. The application of biotechnology on the enhancing of biogas production from lignocellulosic waste. Applied Microbiology and Biotechnology. 2016; 100(23): 9821–9836.
116. Dhavaleswarapu RK, Hoysall CN, Srinivasaiah D. Thermal-alkaline pretreatment of different biomass to understand the interplay of composition of biomass, biogas yields, rates and mass balance. Bioresource Technology Reports. 2025; 30: 102162.
117. Karri S, Sierra-Alvarez R, Field JA. Zero valent iron as an electron-donor for methanogenesis and sulfate reduction in anaerobic sludge. Biotechnology and Bioengineering. 2005; 92(7): 810–819.
118. Hao H, Tian Y, Zhang H, et al. Copper stressed anaerobic fermentation: Biogas properties, process stability, biodegradation and enzyme responses. Biodegradation. 2017; 28: 369–381.
119. Hanay O, Hasar H, Kocer NN. Effect of EDTA as washing solution on removing of heavy metals from sewage sludge by electrokinetic. Journal of Hazardous Materials. 2009; 169(1–3): 703–710.
120. He Y, Pang Y, Liu Y, et al. Physicochemical characterization of rice straw pretreated with sodium hydroxide in the solid state for enhancing biogas production. Energy & Fuels. 2008; 22(4): 2775–2781.
121. Suanon F, Sun Q, Li M, et al. Application of nanoscale zero valent iron and iron powder during sludge anaerobic digestion: Impact on methane yield and pharmaceutical and personal care products degradation. Journal of Hazardous Materials. 2017; 321: 47–53.
122. Rasouli M, Ajabshirchi Y, Mousavi SM, et al. Process optimization and modeling of anaerobic digestion of cow manure for enhanced biogas yield in a mixed plug-flow reactor using response surface methodology. Biosci Biotech Res Asia. 2015; 12: 2333–2344.
123. Jin P, Bhattacharya SK, Williams CJ, et al. Effects of sulfide addition on copper inhibition in methanogenic systems. Water Research. 1998; 32(4): 977–988.
124. Roussel J. Metal Behaviour in Anaerobic Sludge Digesters Supplemented with Trace Nutrients [PhD Thesis]. University of Birmingham; 2013.
125. Okeh OC, Onwosi CO, Odibo FJC. Biogas production from rice husks generated from various rice mills in Ebonyi State, Nigeria. Renewable Energy. 2014; 62: 204–208.
126. Ali A, Mahar RB, Soomro RA, et al. Fe_3O_4 nanoparticles facilitated anaerobic digestion of organic fraction of municipal solid waste for enhancement of methane production. Energy Sources, Part A: Recovery, Utilization, and Environmental Effects. 2017; 39(16): 1815–1822.
127. Mu H, Chen Y, Xiao N. Effects of metal oxide nanoparticles (TiO_2, Al_2O_3, SiO_2 and ZnO) on waste activated sludge anaerobic digestion. Bioresource Technology. 2011; 102(22): 10305–10311.
128. Khaledian S, Haji Agha Alizade H, Rasouli M, Shadidi B. Investigating the effects of Co_2O_3, ZnO, and Fe_3O_4 nanoparticles on methane yield during anaerobic co-digestion of municipal organic solid waste using BMP test. Fuel and Combustion. 2021; 14(3): 1–15.
129. Otero-González L, Field JA, Sierra-Alvarez R. Fate and long-term inhibitory impact of ZnO nanoparticles during high-rate anaerobic wastewater treatment. Journal of Environmental Management. 2014; 135: 110–117.
130. Li LL, Tong ZH, Fang CY, et al. Response of anaerobic granular sludge to single-wall carbon nanotube exposure. Water Research. 2015; 70: 1–8.
131. Iijima S. Helical microtubules of graphitic carbon. Nature. 1991; 354: 56–58.
132. Lo HM, Chiu HY, Lo SW, et al. Effects of micro-nano and non micro-nano MSWI ashes addition on MSW anaerobic digestion. Bioresource Technology. 2012; 114: 90–94.

Energy Storage and Conversion 2025, 3(4), 3975.
doi: https://doi.org/10.59400/esc3975

Editorial

More patience—a plea for longer stability testing and systematic data reporting

Rudolf Holze[1,2,3,4]

[1] Confucius Energy Storage Lab, School of Energy and Environment & Z Energy Storage Center, Southeast University, Nanjing 210018, China; rudolf.holze@chemie.tu-chemnitz.de

[2] State Key Laboratory of Materials-Oriented Chemical Engineering, School of Energy Science and Engineering, Nanjing Tech University, Nanjing 210009, China

[3] Chemnitz University of Technology, D-09111 Chemnitz, Germany

[4] Institute of Chemistry, Saint Petersburg State University, St. Petersburg 199034, Russia

CITATION

Holze R. More patience—a plea for longer stability testing and systematic data reporting. Energy Storage and Conversion. 2025; 3(4): 3975. https://doi.org/10.59400/esc3975

ARTICLE INFO

Received: 28 November 2025
Accepted: 1 December 2025
Available online: 7 December 2025

A brief look at publications in this journal, as well as many other journals covering materials and systems for electrochemical energy conversion and storage, confirms the impression that mostly electrochemical materials science in terms of electrode materials, sometimes electrolytes and electrocatalysts, is at work. Once a study of a newly developed material for a battery or supercapacitor electrode is (barely) completed, the authors rush to report. In their enthusiastic excitement, they frequently calculate energy and power density for a single electrode, apparently happily clueless about the absence of single-electrode batteries and capacitors. Reporting charge densities with specification of the explored electrode potential range would be fine [1], and stating explicitly whether only the active material, or the complete electrode material including binder and conductive additives, even the support and current collector, has been included in calculating said charge density would be fine! In case of a complete cell (the terms *full cell* or *full battery* are hardly helpful because they commonly refer to the state of charge), the same applies. Setting up a Ragone plot for a single electrode (material) is obviously baseless, too, but very popular. Disappointed authors afraid to lose their chance to demonstrate the high current capabilities of their electrode have a popular and well-established option: display the capacity, i.e., charge storage capability, retention as a function of applied current!

The second aspect addressed in the title is experimental studies of material and device stability. Certainly, storage and power capabilities are interesting and fascinating, with poor performance on these points, a material is most likely of very small and limited interest for further investigation, not to speak of development. But beyond this, the stability of these data is of major importance. No consumer or user is going to buy a device showing the promised performance only for a few charge/discharge cycles or a few months. Of course, the expected number of cycles depends on the intended application. A secondary battery for a mobile phone, which will be exchanged by the user for a new model with even more gadgets and features after about two years (whether this is an example of sustainability is another question, and perhaps this habit similar to fast fashion in other fields of society and economies is indeed likely to fade sometime) is burdened with much lower expectations than the cells for an electric vehicle or a battery power station expected to work for ten or more years. Accordingly, an electrode (or cell) performance stable for less than 100 cycles is hardly more than a suggestion for further

thorough studies of the causes of the degradation and failure. Instead cycle numbers for batteries between 1000 and 2000 should be the aim [2] as proposed by various national and international agencies.

With supercapacitors and their materials, the situation appears to be even worse. Manufacturers of double-layer (EDLC) capacitors claim millions of charge/discharge cycles without hitting the generally accepted "failure limits" (20% nominal capacity loss and/or doubling of the internal resistance). With this in mind, cycle numbers of a few hundred or maybe 2000 are simply unrealistic or more flatly irrelevant—but are reported nevertheless. A simple estimate suggests that running 10,000 cycles with 26 s duration of a single cycle needs three days—an extended weekend! It is hard to imagine serious reasons for not conducting this experiment with a simple and quite common cycling instrument. Security concerns regarding unsupervised long-term experiments, once thrown at the present author by another professor of physical chemistry who glimpsed a low current electrolysis running overnight in the author's lab, can certainly be mitigated by running the cycling in a suitable laboratory with all safety precautions at industry standards. The extra effort will certainly be appreciated by the scientific community!

Funding: This work received no external funding.

Institutional review board statement: Not applicable.

Informed consent statement: Not applicable.

Data availability statement: Not applicable.

Conflict of interest: The author disclosed no conflict of interest.

References

1. Ge Y, Xie X, Roscher J, et al. How to measure and report the capacity of electrochemical double layers, supercapacitors, and their electrode materials. Journal of Solid State Electrochemistry. 2020; 24: 3215–3230.
2. Qu Q, Liu L, Fu L, et al. Composite Electrolytes for Non-Lithium-Ion Batteries. Polymers. 2025; 17(22): 3084.

Academic Publishing Pte. Ltd.

Add.: 73 Upper Paya Lebar Road #07-02B-01 Centro Bianco Singapore 534818
Email: editorial_office@acad-pub.com
Web: https://ojs.acad-pub.com